Low Temperature Physics/Fizika Nizkikh Temperatur, 2018, v. 44, No. 1, pp. 3–35

Conventional and unconventional impurity effects in superconductors

(Review Article)

Yu.G. Pogorelov

IFIMUP-IN, Departamento de Física e Astronomia, Universidade do Porto, Porto, Portugal

V.M. Loktev

Bogolyubov Institute for Theoretical Physics, NAN of Ukraine, 14b Metrologichna Str., Kiev 03143, Ukraine

National Technical University of Ukraine "KPI", 37 Peremohy Ave., Kiev 03056, Ukraine
E-mail: vloktev@bitp.kiev.ua

Received June 12, 2017, published online November 28, 2017

A survey is done on the effects of impurities in different types of superconductors, both conventional and unconventional, on their electronic spectra and physical properties. These effects can be generally divided on the base of validity (or not) for them of the known Anderson theorem, which is determined by the symmetries of the superconducting state vs those of the impurity perturbation. In this regard, the unconventional behavior can be naturally attributed to this theorem's failure when the impurity effects are generally much stronger and more diverse. Specific forms of such perturbations in different superconducting systems are analyzed and they reveal a variety of possible scenarios for quasiparticle spectra modification, including formation of several superconducting phases, distinguished by the types of specific narrow bands within the main spectrum gap. These phases and transitions between them, including the transition to the normal metal state, present a lot of unconventional features that can be of interest for some practical applications. The concluded observable effects are compared to the available experimental data.

PACS: 74.62.–c Transition temperature variations, phase diagrams;
74.62.Dh Effects of crystal defects, doping and substitution;
74.62.En Effects of disorder;
74.70.Ad Metals; alloys and binary compounds;
74.70.Xa Pnictides and chalcogenides;
74.72.–h Cuprate superconductors.

Keywords: impurity effects, superconductor, electronic spectra.

Contents

1. Introduction

Immediately with the rise of the microscopic theory of superconductivity (SC) [1,2], the interest of researchers was drawn to possible effects of impurities in SC systems. It was motivated by the already known importance of such effects in normal electronic systems, for instance, in semiconductors [3–5] where the impurity doping helps to strongly enhance and stabilize the performance of related devices. However, essential specifics of the SC case were recognized early by Anderson in his famous theorem on insensitivity of the SC order to impurity perturbations, unless they break the time-reversal symmetry of the host system, basic for the Cooper pairing [6]. It was then shown by Abrikosov and Gor'kov (AG) [7] that magnetic impurities, violating this symmetry, indeed can cause a strong suppression of SC order parameter Δ and transition critical temperature T_c (though some deviations from the measured data [8,9] and certain inconsistencies in their Born approximation treatment [10] were indicated later). Furthermore, going beyond the Born approximation for such impurities reveals excistence of bound exitation states at certain discrete energy levels within the SC gap [11–14], in an analogy with the dopant states in semiconductors. Following this analogy, the immediate effects of these states on such basic SC properties (beyond the above noted Δ and T_c) such as the magnetic penetration depth, rf absorption spectra, specific heat, etc., were discussed [15–17], including the possibility for finite impurity bands to emerge from single impurity levels at high enough impurity concentrations [18,19]. The latter process also sets the principal issue of separation between the two alternative types of quasiparticle states, localized and band-like, in the spectrum of a disordered system [20,21]. This is usually estimated through the known Ioffe–Regel–Mott (IRM) criterion [20,22], namely, the state can be considered band-like with well enough defined wave vector **k** if its mean-free-path ℓ is long enough: $k\ell >> 1$. From the point of view of this rich impurity-induced physics, the case of Anderson theorem violation in disordered SC systems can be as well referred to as unconventional. It should be noted that all the above considerations were still limited to the case of most conventional s-wave SC pairing in the host system.

A new pulse for studies on such impurity effects was given in 1980-ies by the discoveries of new families of unconventional SC materials, beginning from the heavy fermion systems with triplet p-wave SC pairing [23–25] and then advancing to even more striking and rapidly expanding field of high critical temperature SC (HTSC) systems including: d-wave cuprates [26–28], s-wave two-band MgB_2 [29–31], $s_{\pm}$-wave iron pnictides [32,33], and, finally, the highest T_c record (201 K under 1.5 Mbar pressure) holder H_2S [34]. Those appeared unusual not only in their types of SC order parameter but also in a pronounced role of their reduced structural dimensionality (layered, interfacial, chain-like). Such diversity of relevant electronic parameters of SC hosts leads to yet broader variety of impurity perturbations on them and to yet richer potentiality of resulting physical effects.

Thus, the important manifestation of unconventional impurity behavior in HTSC cuprates with d-wave SC order was found in formation of in-gap resonance states by non-magnetic Zn impurities [35,36]. Though looking similar to the resonances by heavy impurities in the acoustic spectra of crystals [37] or by isotopic impurities in the electronic spectrum of graphene [38], their too short lifetimes [36] exclude the effect of resonance splitting in the quasiparticle spectrum at growing impurity concentration (as an alternative to the formation of impurity band around the localized level) known for the resonances in phonon and magnon spectra [39]. Nevertheless, pronounced physical effects of these impurities were observed, for instance, in the strong local suppression of SC order parameter [40].

The principal aim of the present article is to give a brief survey on various cases of unconventional impurity effects in HTSC materials, both conventional and unconventional, in order to characterize their general types and physical manifestations and to give some indications for possible further studies on their finer properties.*

A special emphasis in this course is made on the distinction between localized and band-like quasiparticle states.

It should be noted that formation of the latter type of states at energies close to single impurity levels is impossible within the simplest single-impurity approximation (considered for HTSC systems, e.g., in Ref. 41), so accounting for inter-impurity correlations is needed. Besides, the common approaches to such collective impurity effects in SC systems, using either Born or self-consistent T-matrix approximations for impurity scattering amplitude (see, for instance, the recent review article [42]), treat all the quasiparticle states as band-like and thus ignore this dis-

* Therefore we leave aside possible impurity effects in triplet p-wave SC systems where the known T_c values are restricted to ~1 K.

tinction in principle. Similar treatments are known to give a misguiding spectrum description, e.g., for narrow impurity bands in doped semiconductors [5,43], so we address this issue by using some properly adapted Green's function (GF) techniques [44] (even at the cost of limiting to simpler two-time GF's [45] instead of more thermally advanced Matsubara ones [46]). Also we limit the consideration to the common BCS regime of relatively weak SC coupling, while the impurity effects under the opposite strong SC coupling limit were recently treated in the first-principles approach [47].

The actual techniques are resumed in Sec. 2, and next they are applied in Sec. 3 for analysis of the known localized in-gap levels by magnetic impurities in common *s*-wave SC materials, including their possible extension into finite impurity bands with unconventional effects in SC thermodynamics, optical, and transport properties. Then Sec. 4 presents the alternative scenario of resonance states produced by non-magnetic impurities in d-wave SC systems, modeling the effects of Cu substitutes in SC cuprates, and compares them with the previous *s*-wave case. The further development of the method is done in Sec. 5 for the case of multiband electronic structure in order to consider a possible alternation of localized and resonance impurity states in the specific case of two-gap *s*-wave SC MgB_2. Finally, yet another SC order symmetry, of the $s_{\pm}$ type, such as that known in iron pnictide compounds, is considered in Sec. 6 showing this case also to admit unconventional effects by non-magnetic impurities and discussing their observable effects.

2. Green's function methods for disordered superconductors

As mentioned above, our main tool for the analysis of quasiparticle spectra in disordered many-electron systems and their related observable properties are the two-time (retarded, Fourier-transformed) GF's [45]:

$$\langle\langle a \,|\, b\rangle\rangle_{\varepsilon} = i \int_{-\infty}^{0} \mathrm{e}^{i(\varepsilon - i0)t} \langle\{a(t), b(0)\}\rangle dt, \tag{1}$$

where $\{a(t), b(0)\}$ is the anticommutator of fermion operators in the Heisenberg representation, $\langle\ldots\rangle$ is the quantum statistical average with the system generalized Hamiltonian $H - \mu N$ (at chemical potential μ, as a rule close to the Fermi energy ε_F), and the variables of energy ε and temperature T are defined in the units of $\hbar = k_B = 1$. The basic equation of motion for GF's:

$$\varepsilon\langle\langle a \,|\, b\rangle\rangle = \langle\{a(0), b(0)\}\rangle + \langle\langle [a, H] \,|\, b\rangle\rangle, \tag{2}$$

involves the commutator $[a, H]$ and opens the way for their consequent calculation. The practical importance of GF's is in the possibility to obtain the related observable quantities (the averages of some Hermitian operators) using the spectral theorem:

$$\langle ba\rangle = \frac{1}{\pi} \int_{-\infty}^{\infty} d\varepsilon \, \mathrm{Im}\, \langle\langle a \,|\, b\rangle\rangle_{\varepsilon}, \tag{3}$$

but without a detailed quantum-mechanical solution for the macroscopic Hamiltonian H. Despite the known restrictions on the GF's version given by Eq. (1) (compared to their more advanced forms, such as those by Matsubara [46] or Keldysh [48]), it has an advantage of its simpler equation of motion, Eq. (2), which better fits just the specifics of disordered systems. In what follows, the energy argument ε of GF's will be omitted as a rule.

2.1. Green's function description of pure superconductors

Impurity effects in SC materials are essentially determined by the symmetries of the host band structure (including the SC gap) and of the impurity perturbation potential. The simplest band structure for normal electrons corresponds to a single band of the quasimomentum $\mathbf{k}$ eigenstates with the related Fermi operators $a_{k,\sigma}$ (also labeled by the spin projection σ) and the dispersion law $\varepsilon_{\mathbf{k}}$ of total bandwidth W. It is linearized near the chemical potential (close to the Fermi energy ε_F chosen as the energy reference): $\xi_{\mathbf{k}} = \varepsilon_{\mathbf{k}} - \varepsilon_F \approx v_F(k - k_F)$, to define the second quantization Hamiltonian $H_0 = \sum_{\mathbf{k},\sigma} \xi_{\mathbf{k}} a^{\dagger}_{\mathbf{k},\sigma} a_{\mathbf{k},\sigma}$. Then the relevant GF's are explicitly given as $\langle\langle a_{\mathbf{k},\sigma} \,|\, a^{\dagger}_{\mathbf{k}',\sigma'}\rangle\rangle = \delta_{\mathbf{k},\mathbf{k}'}\delta_{\sigma,\sigma'} \left(\varepsilon - \xi_{\mathbf{k}}\right)^{-1}$.

For SC electrons, the main object of our study, we pass to the standard BCS Hamiltonian (in absence of impurity perturbation):

$$H_{BCS} = H_0 + \sum_{\mathbf{k},\sigma} \left(\Delta_{\mathbf{k}} a_{\mathbf{k},\sigma} a_{-\mathbf{k},-\sigma} + \mathrm{h.c.}\right), \tag{4}$$

with the SC gap function $\Delta_{\mathbf{k}}$ to be specified below for its different symmetries. In the convenient basis of Nambu spinors: $\psi^{\dagger}_{\mathbf{k}} = (a^{\dagger}_{\mathbf{k},\uparrow}, a_{-\mathbf{k},\downarrow})$, the BCS Hamiltonian is presented as

$$H_{BCS} = \sum_{k} \psi^{\dagger}_{\mathbf{k}} (\xi_{\mathbf{k}} \hat{\tau}_3 + \Delta_{\mathbf{k}} \hat{\tau}_1) \psi_{\mathbf{k}}, \tag{5}$$

with the Pauli matrices $\hat{\tau}_l$ ($l = 1, 2, 3$). Then the electronic dynamics follow from the respective GF matrices: $\hat{G}_{\mathbf{k},\mathbf{k}'} = \langle\langle \psi_{\mathbf{k}} \,|\, \psi^{\dagger}_{\mathbf{k}'}\rangle\rangle$. Particularly important is the momentum-diagonal GF, also called the propagator: $\hat{G}_{\mathbf{k},\mathbf{k}} \equiv \hat{G}_{\mathbf{k}}$, that define the SC quasiparticle spectrum $\varepsilon = E_{\mathbf{k}}$ through the dispersion equation [49]:

$$\mathrm{Re}\det \hat{G}^{-1}_{\mathbf{k}} = 0. \tag{6}$$

The propagator's diagonal elements (in Nambu indices) define the quasiparticle (global) density of states (DOS):

$$\rho(\varepsilon) = \frac{1}{\pi N}\mathrm{Im}\mathrm{Tr}\sum_{\mathbf{k}}\hat{G}_{\mathbf{k}}, \tag{7}$$

where N is the number of points in the Brillouin zone (BZ) (not to be confused with the operator of excitation numbers mentioned after Eq. (1)). Evidently, the normalization condition for DOS holds:

$$\int_{-\infty}^{\infty}\rho(\varepsilon)d\varepsilon = 1.$$

Next, the propagator's Nambu-off-diagonal elements define the gap function $\Delta_{\mathbf{k}}$ itself from the BCS gap equation:

$$\Delta_{\mathbf{k}} = \frac{1}{\pi N}\int_0^{\infty} d\varepsilon \tanh\frac{\varepsilon}{2T}\mathrm{Im}\mathrm{Tr}\sum_{\mathbf{k}'}{}'\Lambda_{\mathbf{k},\mathbf{k}'}\hat{G}_{\mathbf{k}',\mathbf{k}'}\hat{\tau}_1. \tag{8}$$

Here the SC coupling function $\Lambda_{\mathbf{k},\mathbf{k}'}$ is usually taken in the factorized form: $\Lambda_{\mathbf{k},\mathbf{k}'} = \Lambda\gamma_{\mathbf{k}}\gamma_{\mathbf{k}'}$, where the momentum dependent function $\gamma_{\mathbf{k}} = \theta(\omega_D - |\xi_{\mathbf{k}}|)\gamma_{\varphi}$ includes the radial restriction to the BCS shell of $\pm\omega_D$ (the Debye frequency) width around the Fermi surface, expressed by the primed sum in Eq. (8). Also the dependence of γ_{φ} on an azimuthal momentum variable $\varphi_{\mathbf{k}}$ defines the particular symmetry of SC order, $\Delta_{\mathbf{k}} = \Delta\gamma_{\mathbf{k}}$. In what follows we adopt the usual BCS model hierarchy of energy scales: $\Delta << \omega_D << \varepsilon_F < W$, in conformity with the known experimental data.

Otherwise, the Nambu-diagonal elements of the momentum-off-diagonal GF's define the local density of states (LDOS) on **n**th lattice site:

$$\rho_{\mathbf{n}}(\varepsilon) = \frac{1}{\pi N}\sum_{\mathbf{k},\mathbf{k}'}\mathrm{e}^{i(\mathbf{k}-\mathbf{k}')n}\mathrm{Im}\mathrm{Tr}\,\hat{G}_{\mathbf{k},\mathbf{k}'}, \tag{9}$$

effectively displayed by scanning tunneling microscopy (STM) studies on these systems. Eventually, the local deviation of the order parameter on **n**th site from its average Δ over the crystal results from both momentum- and Nambu off-diagonal GF's:

$$\Delta_{\mathbf{n}} - \Delta = \frac{\Lambda}{\pi N}\int_0^{\infty} d\varepsilon \tanh\frac{\varepsilon}{2T}\sum_{\mathbf{k},\mathbf{k}'\neq\mathbf{k}}{}'\mathrm{e}^{i(\mathbf{k}-\mathbf{k}')\mathbf{n}}\gamma_{\mathbf{k}'}\mathrm{Im}\mathrm{Tr}\,\hat{G}_{\mathbf{k},\mathbf{k}'}\hat{\tau}_1, \tag{10}$$

it can be also measured by the STM techniques. In a similar way, other physical quantities can be expressed in terms of GF's.

Use of Eq. (2) for the unperturbed SC system with the Hamiltonian, Eq. (4), gives the explicit solution for related GF matrices as

$$\hat{G}^{(0)}_{\mathbf{k},\mathbf{k}'} = \delta_{\mathbf{k},\mathbf{k}'}\frac{\varepsilon + \xi_{\mathbf{k}}\hat{\tau}_3 + \Delta_{\mathbf{k}}\hat{\tau}_1}{\varepsilon^2 - \xi_{\mathbf{k}}^2 - \Delta_{\mathbf{k}}^2}, \tag{11}$$

whose denominator defines, accordingly to Eq. (6), the explicit dispersion law for unperturbed quasiparticles: $E_{\mathbf{k}} = \sqrt{\xi_{\mathbf{k}}^2 + \Delta_{\mathbf{k}}^2}$.

Strictly speaking, the solution in the form of Eq. (11) is rigorous only at zero temperature but in what follows we shall also use it for finite (but low enough) temperatures, only considering the most pronounced temperature effect on the gap parameter $\Delta_{\mathbf{k}}$.

Then, for the conventional *s*-wave SC order: $\gamma_{\varphi} = 1$, $\Delta_{\mathbf{k}} = \Delta_s$ (implicitly temperature dependent, $\Delta_s \equiv \Delta_s(T)$), Eq. (11) can be used in Eq. (7), with the sum in **k** converted to integral in $\xi_{\mathbf{k}} = \xi$ by the rule

$$\frac{1}{N}\sum_{\mathbf{k}} f(\xi_{\mathbf{k}}) = \rho_N\int_{-\varepsilon_F}^{W-\varepsilon_F} f(\xi)d\xi,$$

where ρ_N is the Fermi DOS of normal metal. This results in the BCS expression for DOS:

$$\rho_s^{(0)}(\varepsilon) = \rho_N\frac{\varepsilon}{\sqrt{\varepsilon^2 - \Delta_s^2}}\theta\left(\varepsilon^2 - \Delta_s^2\right). \tag{12}$$

Using of Eq. (11) in the gap equation, Eq. (8), permits to present it in the standard form:

$$\frac{1}{\lambda} = S^{(0)}(\Delta_s, T), \tag{13}$$

with the dimensionless SC coupling parameter $\lambda = \Lambda\rho_N$ and the (unperturbed *s* wave) BCS order function:

$$S^{(0)}(\Delta_s, T) = \int_{\Delta_s}^{\sqrt{\omega_D^2+\Delta_s^2}} d\varepsilon \tanh\frac{\varepsilon}{2T}\frac{1}{\sqrt{\varepsilon^2 - \Delta_s^2}}.$$

In the limit of zero temperature, one has $S^{(0)}(\Delta_s, 0) = \mathrm{arcsinh}[\omega_D/\Delta_s]$, and then arrives at the known result for the (maximum) *s*-wave order parameter: $\Delta_s(0) = \omega_D/\sinh(1/\lambda) \approx 2\omega_D\mathrm{e}^{-1/\lambda}$. Next, the critical temperature for this case, T_s, is found from Eq. (13) in the limit of $\Delta_s \to 0$:

$$\frac{1}{\lambda} = S^{(0)}(0, T_s) \approx \ln\frac{2\omega_D}{\pi T_s} + \gamma_E, \tag{14}$$

as $T_s \approx (2/\pi)\omega_D\mathrm{e}^{\gamma_E - 1/\lambda}$ with the Euler constant $\gamma_E \approx 0.5772$, it assures the BCS universal ratio: $r_s = \Delta_s(0)/T_s \approx \pi\mathrm{e}^{-\gamma_E} \approx 1.76$.

In the case of unconventional, *d*-wave SC order (actual for HTSC perovskites with quasi-2D spectrum), the nontrivial symmetry factor $\gamma_{\varphi} = \cos 2\varphi_{\mathbf{k}}$ with the angular argument $\varphi_{\mathbf{k}} = \arctan k_y/k_x$ provides the related angular dependent order parameter $\Delta_{\mathbf{k}} = \Delta_d\cos 2\varphi_{\mathbf{k}}$ (again implying its temperature dependence). Then, with the generalized integration rule

$$\frac{1}{N}\sum_{\mathbf{k}} f(\xi_{\mathbf{k}},\varphi_{\mathbf{k}}) = \frac{\rho_N}{2\pi}\int_0^{2\pi} d\varphi \int_{-\varepsilon_F}^{W-\varepsilon_F} d\xi f(\xi,\varphi)$$

the corresponding DOS takes the form

$$\rho_d^{(0)}(\varepsilon) = \frac{2\rho_N}{\pi} K\left(\frac{\Delta_d^2}{\varepsilon^2}\right) \tag{15}$$

with the 1st kind full elliptic integral K [50]. Its unconventional behavior, compared to Eq. (12), is in reaching zero only at $\varepsilon \to 0$ and having only logarithmic singularities at $\varepsilon = \pm\Delta_d$ (as the line *2* in Fig. 2). Then the gap equation, Eq. (8), is presented at zero temperature as

$$\frac{1}{\lambda} = \frac{4}{\pi^2}\int_0^{\infty} d\varepsilon \int_0^{\pi/2} d\varphi \cos^2\varphi \times$$

$$\times \operatorname{Im}\int_0^{\omega_D} \frac{d\xi}{\varepsilon^2 - \xi^2 - \Delta_d^2(0)\cos^2\varphi} = D^{(0)}\left(\frac{\omega_D}{\Delta_d(0)}\right), \tag{16}$$

the latter function being also expressed as

$$D^{(0)}(x) = \frac{2}{\pi}\int_0^1 dt \frac{t^2}{\sqrt{1-t^2}} \operatorname{arcsinh}\frac{x}{t}.$$

For relevant big arguments, $x >> 1$, this function has the simple asymptotics: $D^{(0)}(x) = \ln\sqrt{4x} - 1/4 + O(1/x^2)$, providing the *d*-wave order parameter value:

$$\Delta_d(0) \approx 4\omega_D e^{-2/\lambda - 1/2}. \tag{17}$$

Otherwise, the critical temperature for this case is obtained from:

$$\frac{1}{\lambda} = \frac{4}{\pi^2}\int_0^{\infty} d\varepsilon \tanh\frac{\varepsilon}{2T_d} \int_0^{\pi/2} \cos^2\varphi\, d\varphi \times$$

$$\times \operatorname{Im}\int_0^{\omega_D} \frac{d\xi}{\varepsilon^2 - \xi^2} \approx \frac{1}{2}\left(\ln\frac{2\omega_D}{\pi T_d} + \gamma_E\right) \tag{18}$$

(its r.h.s. being exactly 1/2 of that in Eq. (14)), leading to $T_d \approx (2/\pi)\omega_D e^{\gamma_E - 2/\lambda}$. Hence the resulting ratio:

$$r_d = \frac{\Delta_d(0)}{T_d} \approx \frac{2}{\sqrt{e}} r_s \approx 2.14, \tag{19}$$

is as universal as r_s but notably exceeds it, which can be seen as another unconventional feature of the *d*-wave case. Note a good agreement of the theoretical value given by Eq. (19) with the typical experimental value, $r_d \approx 2.2$ for HTSC perovskites.

The forthcoming analysis of impurity effects involves the correlator GF's, $\hat{G}_{\mathbf{n}} = N^{-1}\sum_{\mathbf{k}} e^{i\mathbf{kn}}\hat{G}_{\mathbf{k}}$, expressing correlations between two lattice sites at separation **n** produced by quasiparticles with given energy ε. In particular, the locator $\hat{G}_{\mathbf{n}=0} \equiv \hat{G}_0$, important for single-impurity effects, is presented as a sum of three components:

$$\hat{G}_0 = g_0 + g_1\hat{\tau}_1 + g_3\hat{\tau}_3, \qquad g_0 = \frac{\varepsilon}{N}\sum_{\mathbf{k}} \frac{1}{\varepsilon^2 - \xi_{\mathbf{k}}^2 - \Delta_{\mathbf{k}}^2},$$

$$g_1 = \frac{1}{N}\sum_{\mathbf{k}}{}' \frac{\Delta_{\mathbf{k}}}{\varepsilon^2 - \xi_{\mathbf{k}}^2 - \Delta_{\mathbf{k}}^2}, \quad g_3 = \frac{1}{N}\sum_{\mathbf{k}} \frac{\xi_{\mathbf{k}}}{\varepsilon^2 - \xi_{\mathbf{k}}^2 - \Delta_{\mathbf{k}}^2}. \tag{20}$$

In the relevant low-energy range, $|\varepsilon| << \varepsilon_F$, ω_D, the dominant BCS contributions into the $\hat{G}_0$ matrix come from the vicinity of the Fermi surface and it will be shown below that these contributions (sensitive to a specific SC order) decide validity of Anderson's theorem for a given SC material in presence of impurities. Besides, there are some subdominant contributions into $\hat{G}_0$, coming from the rest of BZ, that are insensitive to the SC order but sensitive to the overall (normal) spectrum.

Thus, for the *s*-wave case, supposing the linearized dispersion $\xi_{\mathbf{k}} = v_F(k - k_F)$ to be valid over the whole spectrum width W, we obtain

$$g_0 \approx \rho_N\varepsilon\left(-\frac{\pi}{\sqrt{\Delta_s^2 - \varepsilon^2}} + \frac{W}{(W-\varepsilon_F)\varepsilon_F}\right),$$

$$g_1 \approx \rho_N\Delta_s\left(-\frac{\pi}{\sqrt{\Delta_s^2 - \varepsilon^2}} + \frac{2}{\omega_{D_s}}\right),$$

$$g_3 \approx \rho_N \ln\sqrt{\frac{W}{\varepsilon_F} - 1}, \tag{21}$$

where the dominant terms $\sim \pi/\sqrt{\Delta_s^2 - \varepsilon^2}$ are present in g_0 and g_1 while the remaining parts of g_0, g_1 together with g_3 are subdominant. The comparison between these two types of contributions is presented in Fig. 1. The same *s*-wave case, but supposing the free electron overall spectrum, $\xi_{\mathbf{k}} = (k^2 - k_F^2)/2m$, differs from that only by a modification of the subdominant terms:

$$g_0 \approx \rho_N\varepsilon\left(-\frac{\pi}{\sqrt{\Delta_s^2 - \varepsilon^2}} + \frac{1}{\varepsilon_F}\ln\frac{\sqrt{W} + \sqrt{\varepsilon_F}}{\sqrt{W - \varepsilon_F}}\right),$$

$$g_1 \approx \rho_N\Delta_s\left(-\frac{\pi}{\sqrt{\Delta_s^2 - \varepsilon^2}} + \frac{\omega_D}{2\varepsilon_F^2}\right),$$

$$g_3 \approx \rho_N\left(\sqrt{\frac{W}{\varepsilon_F}} - \ln\frac{\sqrt{W} + \sqrt{\varepsilon_F}}{\sqrt{W - \varepsilon_F}}\right). \tag{22}$$

In the *d*-wave case, the dominant terms are only present in g_0 as real and imaginary parts of $i\rho_N K(\Delta_d^2/\varepsilon^2)$, while $g_1 = 0$ and all the subdominant terms remain as those in

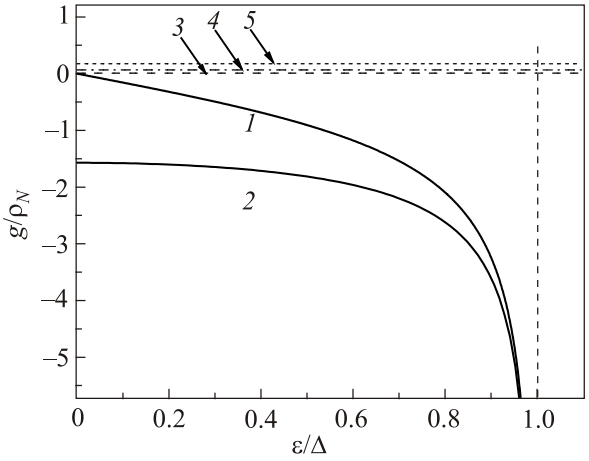

Fig. 1. Comparison between two types of contributions to the $\hat{G}_0$ locator GF in function of energy for the case of *s*-wave SC: the dominant (*1* to g_0 and *2* to g_1) and subdominant (*3* to g_0, *4* to g_1 and 5 to g_3). The latter ones are presented as given by Eq. (21) for the fully linear dispersion law at the choice of parameters: $\varepsilon_F/\Delta_s(0)=100$, $\omega_D/\Delta_s(0)=30$, $W/\varepsilon_F=3$.

Eqs. (21) or (22) (see Fig. 2). Formally, this expression for $\hat{G}_0$ also holds for the *p*-wave case with $\Delta_{\mathbf{k}}=\Delta_p k_z/k$.

General correlators $\hat{G}_{\mathbf{n}\neq 0}$ are important for the analysis of the effects of impurity clusters. For the same low-energy range, their deviation from $\hat{G}_0$ becomes notable at long distances $n=|\mathbf{n}|$ compared to the lattice period, in which case only the dominant contributions can be taken into account. Their explicit calculation for the *s*-wave case results in

$$\hat{G}_{\mathbf{n}} \approx \hat{G}_0 \frac{\sin k_F n}{k_F n} \mathrm{e}^{-n/r_{\mathrm{cor}}}, \qquad (23)$$

presenting, besides the Friedel-like oscillating $(\sin k_F n)/(k_F n)$ term, also the exponential factor with the energy dependent correlation radius $r_{\mathrm{cor}}=\pi\xi_{\mathrm{coh}}\Delta/\sqrt{\Delta^2-\varepsilon^2}$. It can be much longer than the BCS coherence length $\xi_{\mathrm{coh}}=v_F/(\pi\Delta)$ for energies ε approaching the gap edge Δ (here and in what follows, Δ without subindices is understood as $\Delta_{s,d}$ for the respective case). We notice that the spatial behavior of the correlator function, Eq. (23), also defines the wave function of a localized state (at an in-gap energy: $\varepsilon^2<\Delta^2$), so r_{cor} can be also considered its localization radius r_{loc} [39]. For well known typical values of $\xi_{\mathrm{coh}}\sim 100$–$1000$ nm in *s*-wave SC's, this radius could be even much longer than that known for shallow donor and acceptor levels in normal semiconductors [51]. This would indicate even sharper impurity effects in SC materials than in doped semiconductors (provided the in-gap localized levels are permitted here by the system symmetry). However the exponential factor in Eq. (23) turns irrelevant for description of most important effects at high enough impurity concentrations c when the mean inter-impurity distance $\bar{r}\sim c^{-1/3}$ is much shorter than r_{loc}. Otherwise, for higher energies, $\varepsilon^2>>\Delta^2$, relevant for calculation of local observables, the exponential factor in Eq. (23) becomes oscillating but much slower than the Friedel oscillations and can be also disregarded.

The spatial structure of the general correlator for the *d*-wave (and 2D) case is more complicated, because of a specific interference between Friedel-like radial oscillations and fourfold azymuthal symmetry of SC dispersion law in its explicit expression:

$$\hat{G}_{\mathbf{n}}=\frac{\rho_N}{2\pi}\int_0^{2\pi} d\varphi \int_{-\varepsilon_F}^{W-\varepsilon_F} d\xi \mathrm{e}^{ikn\cos(\varphi-\theta)} \frac{\varepsilon+\Delta\cos 2\varphi\hat{\tau}_1+\xi\hat{\tau}_3}{\varepsilon^2-\Delta^2\cos^2 2\varphi-\xi^2}, \qquad (24)$$

where $\theta=\arctan n_x/n_y$. Generally it does not permit factorization like in Eq. (23). Here, this simple form is only achieved in the high-energy limit, $\varepsilon^2>>\Delta^2$, with the Friedel oscillation factor $(\sin k_F n)/(k_F n)$ changed to $J_0(k_F n)$ (see Fig. 3). Otherwise, for low energies, $\varepsilon^2\lesssim\Delta^2$,

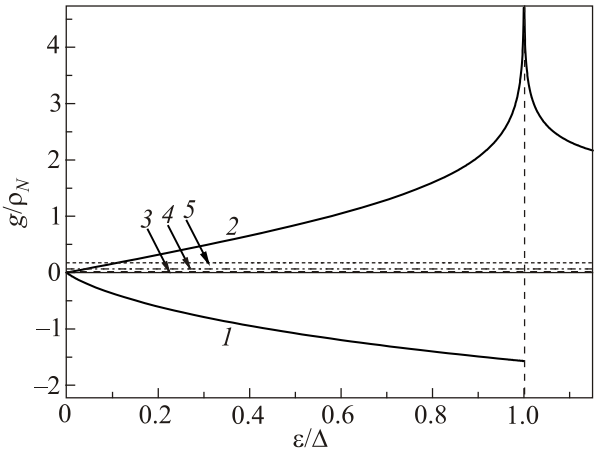

Fig. 2. The dominant (*1* for $\mathrm{Re}\, g_0$ and *2* for $\mathrm{Im}\, g_0$) and subdominant (the same as those in Fig. 1) contributions to $\hat{G}_0$ for the case of *d*-wave SC.

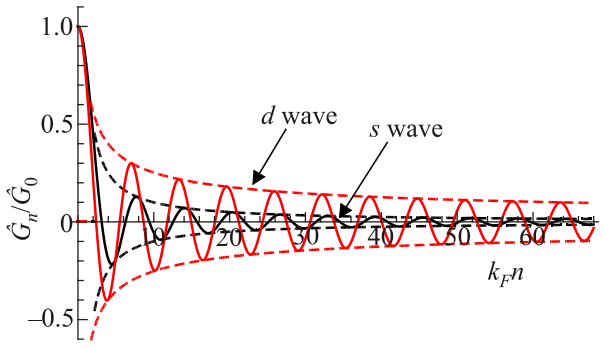

Fig. 3. (Color online) Comparison of correlators $\hat{G}_{\mathbf{n}}$ for the *s*-wave and *d*-wave SC's (in the high-energy limit $\varepsilon^2>>\Delta^2$) vs distance n (in units of the Fermi wavelength $1/k_F$).

its spatial behavior is only obtained from numerical calculation in Eq. (24) and displays fourfold azymuthal anisotropy. In particular, it consists in variation of the oscillating function argument from $k_F n$ along the nodal directions, $n_x^2 = n_y^2$, to $k_F n/\sqrt{2}$ along the antinodal directions, $n_x = 0$ or $n_y = 0$.

2.2. Impurity perturbations in superconductors

After having defined the basic parameters of pure *s*- and *d*-wave SC systems, we can pass to their modification under the effects of impurity perturbations. Those for an SC system are most simply modeled by identical scatterers located in random lattice sites p, in addition to the BCS Hamiltonian, Eq. (4). For the case of spin-independent (non-magnetic) scattering, it can be presented as

$$H_{\text{imp}} = \frac{1}{N}\sum_{\mathbf{p},\mathbf{k},\mathbf{k}'} \mathrm{e}^{i(\mathbf{k}'-\mathbf{k})\mathbf{p}} \psi_{\mathbf{k}}^{\dagger} V_{\mathbf{k}-\mathbf{k}'} \hat{\tau}_3 \psi_{\mathbf{k}'}. \qquad (25)$$

Here the Fourier image $V_{\mathbf{k}-\mathbf{k}'}$ of the impurity perturbation potential $V(\mathbf{r})$ can be generally expanded into a sum of factorable terms: $V_{\mathbf{k}-\mathbf{k}'} = \sum_{l=1}^{m} V_l \alpha_{\mathbf{k},l} \alpha_{\mathbf{k}',l}^{*}$, each related to lth representation of the local symmetry group for the cluster of m sites affected by the impurity. From the general theory [52], the coefficients $\alpha_{\mathbf{k},l}$ satisfy the relations of orthogonality: $\sum_{\mathbf{k}} \alpha_{\mathbf{k},l}\alpha_{\mathbf{k},l'}^{*} = \delta_{l,l'}$, and completeness: $\sum_{l} \alpha_{\mathbf{k},l}\alpha_{\mathbf{k},l}^{*} = m$, but the simplest case of point-like potential, $V(\mathbf{r}) = V\delta(\mathbf{r})$, yields an obvious constant: $V_{\mathbf{k}-\mathbf{k}'} = V$, reducing the above expansion to the single trivial representation with $l = 1$, $\alpha_{V_{\mathbf{k}},1} = 1$.

For the case of magnetic impurities, the perturbation potential $V_{\mathbf{k}-\mathbf{k}'}\hat{\tau}_3$ in Eq. (25) is modified by addition of the magnetic exchange term $J\mathbf{s}_{\mathbf{p}}\boldsymbol{\tau}$ with the impurity spin operator $\mathbf{s}_{\mathbf{p}}$, resembling the Kondo problem in normal metals [53]. Then the equation of motion, Eq. (2) produces, aside from the simply scattered GF's $\langle\langle a_{\mathbf{k}'} \mid a_{\mathbf{k}}^{\dagger}\rangle\rangle$, also some new composite GF's: $\langle\langle \mathbf{s}_{\mathbf{p}}^{l}\mathbf{s}_{\mathbf{p}'}^{l'} \ldots \mathbf{s}_{\mathbf{p}''}^{l''} a_{\mathbf{k}'} \mid a_{\mathbf{k}}^{\dagger}\rangle\rangle$, where $l, l', \ldots, l'$ are the Cartesian indices for respective spins. In the same analogy with the Kondo problem and supposing the impurity spins fully uncorrelated (paramagnetic), a reasonable simplification is then obtained by decoupling such composite GF's as

$$\langle\langle s_{\mathbf{p}}^{2} a_{\mathbf{k}'} \mid a_{\mathbf{k}}^{\dagger}\rangle\rangle \approx s(s+1)\langle\langle a_{\mathbf{k}'} \mid a_{\mathbf{k}}^{\dagger}\rangle\rangle, \qquad (26)$$

together with respective powers of $s(s+1)$ from multiple products $s_{\mathbf{p}}^{2}s_{\mathbf{p}'}^{2}\ldots$, while omitting contributions from all other spin compositions.*

In presence of impurity disorder that breaks the translational symmetry of the system, quasimomentum is no longer an exact quantum number for its states, and the spectrum is generally divided into alternative ranges of band-like states (approximately described by quasimomentum) and localized ones (whose quantum numbers have no relation to quasimomentum), separated by the so-called mobility edges [20]. Then the solution for GF matrix is modified vs Eq. (11) by introduction of a self-energy matrix, in a form appropriate for the particular spectrum range [54]. Thus, for the band-like states, this form reads

$$\hat{G}_{\mathbf{k}} = \left[\left(\hat{G}_{\mathbf{k}}^{(0)}\right)^{-1} - \hat{\Sigma}_{\mathbf{k}}\right]^{-1}, \qquad (27)$$

while for the localized states it is

$$\hat{G}_{\mathbf{k}} = \hat{G}_{\mathbf{k}}^{(0)} + \hat{G}_{\mathbf{k}}^{(0)}\hat{\Sigma}^{(0)}\hat{G}_{\mathbf{k}}^{(0)}. \qquad (28)$$

As seen from Eq. (27), its structure permits to define both the dispersion law by Eq. (6) and DOS by Eq. (7), while that in Eq. (28) only applies for DOS. Both types of self-energy matrices are generally expanded in the above referred local symmetry representations: $\hat{\Sigma}_{\mathbf{k}} = \sum_l \hat{\Sigma}_{\mathbf{k},l}$ and $\hat{\Sigma}^{(0)} = \sum_l \hat{\Sigma}_l^{(0)}$, and their partial terms can be then presented in form of group expansions (GE's), in groups of interacting impurity centers at given relative impurity concentration c (supposedly low, $c << 1$) [39]. Thus, for the case of Eq. (27), its construction is

$$\hat{\Sigma}_{\mathbf{k},l} = c\hat{T}_l\left[1 + c\sum_{\mathbf{n}}\left(\hat{A}_{\mathbf{n},l}\mathrm{e}^{-i\mathbf{k}\mathbf{n}} + \hat{A}_{\mathbf{n},l}\hat{A}_{-\mathbf{n},l}\right)\times\right.$$

$$\left.\times\left(1 - \hat{A}_{\mathbf{n},l}\hat{A}_{-\mathbf{n},l}\right)^{-1} + \ldots\right], \qquad (29)$$

called the fully renormalized expansion (FRE), while that for Eq. (28)

$$\hat{\Sigma}_{\mathbf{k},l}^{(0)} = c\hat{T}_l^{(0)}\left[1 + c\sum_{\mathbf{n}}\hat{A}_{\mathbf{n},l}^{(0)}\hat{A}_{-\mathbf{n},l}^{(0)}\left(1 - \hat{A}_{\mathbf{n},l}^{(0)}\hat{A}_{-\mathbf{n},l}^{(0)}\right)^{-1} + \ldots\right] \qquad (30)$$

is called the non-renormalized expansion (NRE). Generally, some other GE types are also possible [39], one such example to be considered in Sec. 3.2 below.

For FRE, its constituents are the single-impurity (partial) T-matrices:

* Generally, Eq. (2) for this case produces yet another set of composite functions of $\langle\langle s_{\mathbf{p}}^{l}s_{\mathbf{p}'}^{l'}\ldots s_{\mathbf{p}''}^{l''}a_{\mathbf{k}'}^{\dagger}a_{\mathbf{k}''}a_{\mathbf{k}'''} \mid a_{\mathbf{k}}^{\dagger}\rangle\rangle$ type, but they can be neglected beside the above considered ones because of additional small thermal occupation factors $\langle n_{\mathbf{k}'}\rangle = \langle a_{\mathbf{k}'}^{\dagger}a_{\mathbf{k}'}\rangle$ emerging at their decoupling.

$$\hat{T}_l = V_l \hat{\tau}_3 \left(1 - \frac{1}{N} \sum_{\mathbf{k}' \neq \mathbf{k}} | \alpha_{\mathbf{k}',l} |^2 \hat{G}_{\mathbf{k}'} \right)^{-1}, \qquad (31)$$

and the related indirect inter-impurity interaction matrices:

$$\hat{A}_{\mathbf{n},l} = \hat{T}_l \frac{1}{N} \sum_{\mathbf{k}' \neq \mathbf{k}} e^{i\mathbf{k}'\mathbf{n}} | \alpha_{\mathbf{k}',l} |^2 \hat{G}_{\mathbf{k}'}, \qquad (32)$$

with the additional restriction of summing to only non-coincident quasimomenta in the products like $\hat{A}_{\mathbf{n},l} \hat{A}_{-\mathbf{n},l}$.

Analogous elements $\hat{T}_l^{(0)}$ and $\hat{A}_{\mathbf{n},l}^{(0)}$ for NRE differ from these in Eqs. (31), (32) only by $\hat{G}_{\mathbf{k}}$ replaced for $\hat{G}_{\mathbf{k}}^{(0)}$ and by no restrictions in quasimomentum sums. The sums in separation vectors **n** (next to unity in the brackets of Eqs. (29) and (30)) describe the effects of quasiparticle interference in pairs of impurities, the omitted higher order GE terms correspond to such effects from impurity triples, etc. [39].

Using these GE's, we can evaluate the important parameters of band-like (coherent) and localized states in the spectrum of a disordered crystal. Thus, the inverse lifetime of a band-like state with given quasimomentum **k** is defined as $\tau_{\mathbf{k}}^{-1} = \mathrm{Im} \det \hat{G}_{\mathbf{k}}^{-1} / | 2E_{\mathbf{k}} |$ and it can be used in the IRM criterion presented as

$$\mathbf{k} \nabla_{\mathbf{k}} E_{\mathbf{k}} >> \tau_{\mathbf{k}}^{-1}. \qquad (33)$$

Then, the approaching of a mobility edge is manifested by the failure of this criterion (that is, when the strong inequality ">>" passes to the "~" relation). This indicates a limit of the band-like range, either of a host band (modified vs its non-perturbed spectrum) or a new, impurity band of coherent states, near a single-impurity level $\varepsilon_{\mathrm{loc},l}$ (a pole of some $\hat{T}_l^{(0)}$). This condition is also accompanied by the loss of FRE convergence, while the NRE can still remain convergent and then it describes DOS of localized states. Finally, the NRE convergence can be also lost at sufficient proximity to a single-impurity level, giving an estimate for its concentrational broadening.

Presence of two qualitatively different types of quasiparticle states in the spectrum with their proper GF forms requires reformulation of the gap equation, Eq. (8). Now, the energy integration over each range should be done using the respective (FRE or NRE) GF form. Then two different mechanisms for the impurity-induced gap reduction should be distinguished: (i) due to modification of the host bands, a more conventional one, and (ii) due to emergence of in-gap impurity levels or impurity bands. The latter can be considered an unconventional mechanism and, as will be seen below, it can strongly enhance the impurity effect and provide some new qualitative features to the system.

Now we proceed to the particular cases of SC systems with impurities, starting from the simplest point-like scatterers in an *s*-wave BCS host.

3. Impurity levels and impurity bands in *s*-wave superconductors

3.1. The case of non-magnetic impurities

In an *s*-wave SC system with non-magnetic point-like impurities, calculation of the self-energy matrices given by Eq. (31) and simplified to the single trivial representation of the point symmetry group, results in the single-impurity T-matrix for NRE:

$$\hat{T}^{(0)} = V \left(\hat{\tau}_3 - V \hat{G}_0^{(0)} \right)^{-1}. \qquad (34)$$

Next, in terms of the decomposition, Eq. (20), it is expressed as

$$\hat{T}^{(0)} = V \frac{V \left(g_0 - g_1 \hat{\tau}_1 \right) + \left(1 - V g_3 \right) \hat{\tau}_3}{\left(1 - V g_3 \right)^2 - V^2 \left(g_0^2 - g_1^2 \right)}, \qquad (35)$$

and possible localized in-gap levels would be given by its poles. But if the $\hat{G}_0$ components presented by Eqs. (21) or (22) are restricted only to their dominant terms, it is readily seen that the denominator of Eq. (35) becomes a positive constant: $(1 - V g_3)^2 (1 + v^2)$, with the dimensionless impurity perturbation parameter $v = \pi \rho_N V / (1 - V g_3)$. This constancy prevents quasiparticle localization by a single impurity center and related restructuring of the spectrum at finite impurity concentrations. Then, approximating the self-energy matrix by its T-matrix term in Eqs. (29), (30) and using the result of Eq. (35) in the gap equation, Eq. (8), we get the modification of Eq. (13) in that the order function $S^{(0)}(\Delta, T)$ is replaced for

$$\frac{1}{\lambda} = S(\Delta, T) = \frac{1}{2\pi} \int_{-\infty}^{\infty} s(\varepsilon, \Delta) \tanh \frac{\varepsilon}{2T} d\varepsilon,$$

$$\text{with} \quad s(\varepsilon, \Delta) = \mathrm{Im} \frac{\tilde{\Delta}}{\Delta} \int_0^{\omega_D} \frac{d\xi}{\tilde{\varepsilon}^2 - \tilde{\Delta}^2 - \xi^2}. \qquad (36)$$

Here the renormalized energy and gap variables are defined by the relations

$$\frac{\tilde{\varepsilon}}{\varepsilon} = \frac{\tilde{\Delta}}{\Delta} = 1 - \frac{i\zeta}{\sqrt{\varepsilon^2 - \Delta^2}} \quad \text{with} \quad \zeta = \frac{cVv}{1 + v^2},$$

and the uniform shift of the dispersion law ξ by ζ / v is implicitly accounted for. The gap parameter results from Eq. (36) as a function of temperature and impurity concentration: $\Delta = \Delta(T, c)$, though in this case the impurity parameters c and v enter it only through their single combination ζ. In what follows, we denote $\Delta_0 \equiv \Delta(0, 0)$ the maximum possible (for given λ) gap value.

Next we notice that the function $s(\varepsilon, \Delta)$ in Eq. (36) is only non-zero at $\varepsilon^2 > \Delta^2$. Then, passing to the complex variable $z = \xi / (\sqrt{\varepsilon^2 - \Delta^2} - i\zeta)$, it is transformed to

$$s(\varepsilon,\Delta) = \mathrm{Im}\left(\frac{1}{\sqrt{\varepsilon^2-\Delta^2}}\int_{z_-}^{z_+}\frac{dz}{1-z^2}\right),$$

with $z_\pm = \pm\omega_D/(\sqrt{\varepsilon^2-\Delta^2}-i\zeta)$. Taking the standard integral

$$\int_{z_-}^{z_+}\frac{dz}{1-z^2} = \mathrm{arctanh}\frac{z_+-z_-}{1-z_+z_-}$$

and separating its imaginary part, one has explicitly

$$s(\varepsilon,\Delta) = \frac{1}{\sqrt{\varepsilon^2-\Delta^2}}\left(\pi - \arctan\frac{2\zeta\omega_D}{\omega_D^2-\varepsilon^2+\Delta^2-\zeta^2}\right). \quad (37)$$

The next integration in Eq. (36) is done over the energy range of $\Delta^2 \le \varepsilon^2 \le \omega_D^2+\Delta^2-\zeta^2$, and for low enough impurity concentrations, such that $\zeta << \omega_D$, the arctan argument in Eq. (37) can be reasonably approximated by $2\zeta/\omega_D << 1$ over all the relevant range of $\varepsilon^2 \lesssim \omega_D^2$, which, for the case of $T = 0$, results finally in

$$\frac{1}{\lambda} \approx \left(1-\frac{2\zeta}{\pi\omega_D}\right)\mathrm{arcsinh}\frac{\omega_D}{\Delta}.$$

Comparing this to Eq. (13) for the unperturbed gap Δ_0, we obtain its relative decay as

$$1-\frac{\Delta}{\Delta_0} \approx \frac{2\zeta}{\pi\lambda\omega_D}, \quad (38)$$

that is linear in concentration c of non-magnetic impurities (shown by the line *2* in Fig. 4). We notice that even in the limit of strong perturbation, $v\to\infty$, its slope stays finite: $1-\Delta/\Delta_0 \to 4c/(\pi^2\lambda\rho_N\omega_D)$, and always much slower of the simplest mean-field expectation: $1-\Delta/\Delta_0 = c|V|/\Delta_0$ (shown by the line *3* in Fig. 4). With further growing c, this decay gets even slower, as seen from the numerical treatment of Eq. (36) with the full form of Eq. (37) (the line *1* in Fig. 4) going formally to zero only at unphysically high impurity concentrations.

The local effect of a non-magnetic impurity on SC order is most simply obtained considering $\mathbf{n} = 0$ a single impurity site in the crystal (actually non-random in this limit). Then the momentum-off-diagonal GF's are $\hat{G}_{\mathbf{k},\mathbf{k}'} = N^{-1}\hat{G}^{(0)}_{\mathbf{k}}\hat{T}^{(0)}\hat{G}^{(0)}_{\mathbf{k}'}$ and their summation over $\mathbf{k},\mathbf{k}'$ in Eq. (10) gives

$$\Delta_{\mathbf{n}} - \Delta = \frac{\Lambda}{\pi}\int_0^\infty d\varepsilon \tanh\frac{\varepsilon}{2T}\,\mathrm{Im}\mathrm{Tr}\,\hat{G}^{(0)}_{\mathbf{n}}\hat{T}^{(0)}\hat{G}^{(0)}_{\mathbf{k}'}\hat{\tau}_1. \quad (39)$$

Next, using of Eqs. (20), (23), (35) leads to the explicit distance dependence

$$\frac{\Delta_{\mathbf{n}}}{\Delta} = 1-\frac{v^2}{1+v^2}\left(\frac{\sin k_F n}{k_F n}\right)^2, \quad (40)$$

shown in Fig. 5.

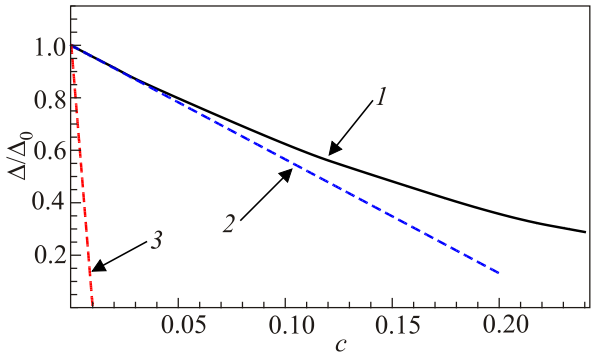

Fig. 4. (Color online) The gap parameter at finite impurity concentration c, $\Delta(c)$, relative to its non-perturbed value Δ_0 for the s-wave SC at the choice of $\omega_D/\Delta_s = 30$ and $T = 0$ in function of the concentration c of non-magnetic impurities with the perturbation parameter $v = 1$. The numerical solution of Eq. (36) (line *1*) and its linear approximation given by Eq. (38) (line *2*) decay much slower than the simple mean-field expectation (line *3*).

These results provide a more detailed insight on the stability of SC order to non-magnetic impurities, concluded to be absolute in Anderson's theorem, only from global symmetry reasons. But the account taken of the specific dynamics of impurity perturbation on SC quasiparticles permits a finite suppression of the global SC order parameter even by those impurities (namely, produced by the arctan term in Eq. (36)). Though the symmetry protection (expressed in the constancy of T-matrix denominator in Eq. (35)) makes this suppression much weaker than it could be expected from simple mean-field reasoning, it is not zero at all and naturally grows with growing impurity parameter ζ (combined from c and v). Also the local SC order at impurity site by Eq. (40) for $\mathbf{n} = 0$: $\Delta_{\mathbf{n}=0} = \Delta/(1+v^2)$, is increasingly suppressed with growing v.

It can be yet noted that the above results can be slightly modified if the subdominant terms in Eqs. (21) or (22) are

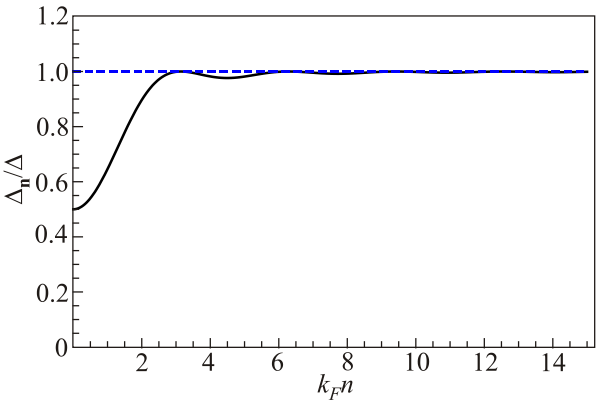

Fig. 5. The local s-wave order parameter $\Delta_{\mathbf{n}}$ in function of the distance from a single non-magnetic impurity center at $\mathbf{n} = 0$ (in k_F^{-1} units). The Friedel-like oscillations described by Eq. (38) decay well before $k_F n$ reaches values $\sim \varepsilon_F/\omega_D >> 1$ where the exponential factor in Eq. (22) could be felt.

also considered. Those will permit a very shallow localized level $\varepsilon_{\rm loc}$ to emerge near the SC gap edge: $\Delta - \varepsilon_{\rm loc} \sim \Delta^3/\omega_D^2$ (for the case of Eq. (21)) or $\sim \Delta^3/\varepsilon_F^2$ (for the case of Eq. (22)). Nevertheless, related straightforward calculations show that presence of such levels can not sensibly modify the impurity effects on the SC order.

3.2. The case of magnetic impurities

A very different situation takes place for magnetic impurities first studied by Abrikosov and Gor'kov [7]. In this case, neglecting for simplicity the non-magnetic part of impurity perturbation, Eq. (25), beside the magnetic term $V_{\rm mag} = J\mathbf{s}_{\mathbf{p}}\boldsymbol{\tau}$, with the parameter J of exchange coupling between host carriers and impurity spin $\mathbf{s}_{\mathbf{p}}$, we obtain the equation of motion for the $\hat{G}_{\mathbf{k}}$ matrix in the form

$$\hat{G}_{\mathbf{k}} = \hat{G}_{\mathbf{k}}^{(0)} + \frac{J}{N}\sum_{\mathbf{p},\mathbf{k}',l} e^{i(\mathbf{k}'-\mathbf{k})\mathbf{p}}\hat{G}_{\mathbf{k}}^{(0)}\hat{\tau}_l\hat{G}_{\mathbf{p};\mathbf{k}',\mathbf{k}}^{l}. \qquad (41)$$

Here the composite GF matrix $\hat{G}_{\mathbf{p};\mathbf{k}',k}^{l}\mathbf{k} = \langle\langle s_{\mathbf{p}}^{l}\psi_{\mathbf{k}'} \mid \psi_{\mathbf{k}}^{\dagger}\rangle\rangle$ presents one of those mentioned at the end of Sec. 2. The equation of motion for this composite GF:

$$\hat{G}_{\mathbf{p};\mathbf{k}',\mathbf{k}}^{l} = \frac{J}{N}\sum_{\mathbf{p}',\mathbf{k}'',l'} e^{i(\mathbf{k}''-\mathbf{k}')\mathbf{p}'}\hat{G}_{\mathbf{k}'}^{(0)}\hat{\tau}_l\hat{G}_{\mathbf{p}',\mathbf{p};\mathbf{k}',\mathbf{k}}^{l',l}, \qquad (42)$$

gives rise to the 2nd order composite GF $\hat{G}_{\mathbf{p}',\mathbf{p};\mathbf{k}',\mathbf{k}}^{l',l} = \langle\langle s_{\mathbf{p}'}^{l'}s_{\mathbf{p}}^{l}\psi_{\mathbf{k}'} \mid \psi_{\mathbf{k}}^{\dagger}\rangle\rangle$. But, for the case of $\mathbf{p}' = \mathbf{p}$, it can be reduced to simpler ones with use of the identity

$$\sum_{l,l'}\hat{\tau}_l\hat{\tau}_{l'}s_{\mathbf{p}}^{l'}s_{\mathbf{p}}^{l} = \sum_{l'\neq l}\hat{\tau}_l\hat{\tau}_{l'}s_{\mathbf{p}}^{l'}s_{\mathbf{p}}^{l} + \sum_{l}\left(s_{\mathbf{p}}^{l}\right)^2 = \sum_{l}\hat{\tau}_l s_{\mathbf{p}}^{l} + s(s+1) \qquad (43)$$

(also allowing the decoupling rule, Eq. (26)). Then, substituting Eq. (43) into Eq. (42), we arrive at

$$\hat{G}_{\mathbf{k}} = \hat{G}_{\mathbf{k}}^{(0)} + cJ^2 s(s+1)\hat{G}_{\mathbf{k}}^{(0)}\hat{G}^{(0)}\hat{G}_{\mathbf{k}} + \frac{J^2}{N}\sum_{\mathbf{p},\mathbf{k}',l} e^{i(\mathbf{k}'-\mathbf{k})\mathbf{p}}\hat{G}_{\mathbf{k}}^{(0)}\hat{G}^{(0)}\hat{\tau}_l\hat{G}_{\mathbf{p};\mathbf{k}',\mathbf{k}}^{l} + \ldots. \qquad (44)$$

The omitted terms in Eq. (44) involve the composite GF's $\hat{G}_{\mathbf{p}'\neq\mathbf{p},\mathbf{p};\mathbf{k}',\mathbf{k}}^{l',l}$ that serve to generate the indirect interaction matrices $\hat{A}_{\mathbf{p}-\mathbf{p}'}$, like those in Eq. (29). The resulting non-trivial T-matrix for this case is

$$\hat{T}_{\rm mag} = J^2 s(s+1)\hat{G}^{(0)}\left[1 - J^2(\hat{G}^{(0)})^2\right]^{-1} = h_{\rm ex}\frac{\sqrt{\Delta^2-\varepsilon^2}\left(\varepsilon + \varepsilon_{\rm loc}\hat{\tau}_1\right)}{\varepsilon^2 - \varepsilon_{\rm loc}^2}, \qquad (45)$$

with the energy scale of exchange nature

$$h_{\rm ex} = Js(s+1)\frac{j_{\rm ex}}{1+j_{\rm ex}^2},$$

and the dimensionless parameter $j_{\rm ex} = \pi\rho_N J$. The two symmetric poles of this matrix at $\varepsilon = \pm\varepsilon_{\rm loc}$ are mainly defined by the dominant parts of $G^{(0)}$ as

$$\varepsilon_{\rm loc} \approx \frac{1-j_{\rm ex}^2}{1+j_{\rm ex}^2}\Delta. \qquad (46)$$

These are just the known Shiba levels for single magnetic impurity [11–14], whose position varies with $j_{\rm ex}^2$ (that is, regardless of the J sign), from the very gap edges (at $j_{\rm ex}^2 << 1$, the weak coupling limit) to its center (at $j_{\rm ex}^2 \to 1$, the strong coupling limit). The following consideration is only limited to the range of $j_{\rm ex}^2 \le 1$ since the case of $j_{\rm ex}^2 \ge 1$ gets reduced to that with the effective value $j_{\rm eff}^2 = 1/j_{\rm ex}^2 \le 1$. We notice that, for typical values of $j_{\rm ex}^2 \sim 1$, the above defined scale $h_{\rm ex}$ is $\sim \rho_N^{-1} \sim \varepsilon_F$.

At finite impurity concentrations (but $c << 1$), one can consider the quasiparticle spectrum (in neglect of $\tau_{\mathbf{k}}^{-1}$) derived from the dispersion equation, Eq. (6), with use of Eqs. (27), (29) (only reduced to the T-matrix term) and Eq. (45):

$$\tilde{\varepsilon}^2 - \tilde{\Delta}^2 - \xi_k^2 = 0. \qquad (47)$$

Here, unlike the non-magnetic case, Eq. (35), the modification is expressed in the energy dependencies:

$$\tilde{\varepsilon} = \left(1 - ch_{\rm ex}\frac{\sqrt{\Delta^2-\varepsilon^2}}{\varepsilon^2-\varepsilon_{\rm loc}^2}\right)\varepsilon,$$

$$\tilde{\Delta} = \Delta + ch_{\rm ex}\frac{\sqrt{\Delta^2-\varepsilon^2}}{\varepsilon^2-\varepsilon_{\rm loc}^2}\varepsilon_{\rm loc}. \qquad (48)$$

Though looking similar to many known cases of impurity band formation, for instance, in doped semiconductors or in magnetic crystals with magnetic impurities [39], this situation has important specifics. First of all, the presence of anomalous $a_{\mathbf{k},\sigma}a_{-\mathbf{k},-\sigma}$ terms in the BCS Hamiltonian, Eq. (4), implies particle-antiparticle hybridization in the resulting eigenstates, also in those from impurity bands (to generalize the concept of Bogolyubov quasiparticles in pure SC systems). On the other hand, this hybridization has a feedback from the SC order parameter Δ, sensible to the impurity effect on the gap equation. We note that, in contrast to the previous case of non-magnetic impurities, here this effect depends on two impurity parameters $j_{\rm ex}$ and c separately and is defined by the gap equation and dispersion equation mutually. The resulting interplay between the dynamics of the main band gap (that defines also the impurity level position by Eq. (45)) and of the impurity

band can produce a number of peculiar features in the overall spectrum and in respective observable properties of the system that are analyzed in more detail below.

Starting from the limit of lowest impurity concentration, when its effect on Δ is yet negligible, we find the formal solutions to Eq. (47) for the in-gap range, $\varepsilon^2 < \Delta^2$, that describe two symmetric impurity bands extended from each localized level towards the gap center (shown for the $\varepsilon > 0$ part in Fig. 6). Their bandwidth is $w_{\rm imp} = \varepsilon_{\rm loc} - \varepsilon_g$, where the band inner edge ε_g is defined from Eq. (47) at $\xi_k = 0$: $\tilde{\varepsilon}^2 = \tilde{\Delta}^2$. In this limit, $w_{\rm imp}$ grows with c linearly: $w_{\rm imp} \approx c h_{\rm ex}/j_{\rm ex}$.

Such band structure resembles the above mentioned cases of normal systems with impurities and, alike them, the next question is to verify whether impurity bands really exist. For this, first of all, the impurity band width should exceed the concentration broadening of localized level $\Gamma_{\rm loc}$, defined by the NRE convergence criterion. The latter is estimated by the comparison between unity and the second term in the brackets of Eq. (30):

$$c\hat{B} = c\sum_{\mathbf{n}} \hat{A}^{(0)}_{\mathbf{n}} \hat{A}^{(0)}_{-\mathbf{n}} \left(1 - \hat{A}^{(0)}_{\mathbf{n}} \hat{A}^{(0)}_{-\mathbf{n}}\right)^{-1}.$$

At not too long distances, $n << r_{\rm cor}(\varepsilon_{\rm loc})$, when the exponential factor in $\hat{G}_{\mathbf{n}}$ given by Eq. (23) can be set to unity, the interaction matrix $\hat{A}^{(0)}_{\mathbf{n}} = \hat{T}_{\rm mag}\hat{G}_{\mathbf{n}}$ is simplified as

$$\hat{A}^{(0)}_{\mathbf{n}} \approx (1+\hat{\tau}_1)\frac{r_\varepsilon}{n}\sin k_F n,$$

with the energy dependent characteristic radius:

$$r_\varepsilon = \frac{s(s+1)}{k_F}\frac{j_{\rm ex}^2}{1+j_{\rm ex}^2}\frac{\varepsilon_{\rm loc}^2}{\varepsilon^2 - \varepsilon_{\rm loc}^2}.$$

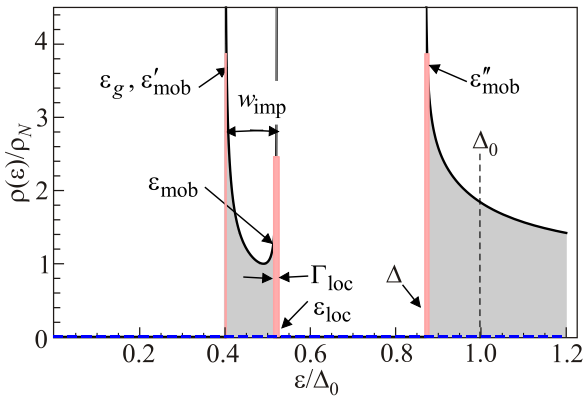

Fig. 6. (Color online) DOS at $T = 0$ in an s-wave SC where the localized level $\varepsilon_{\rm loc}$ by a magnetic impurity is expanded at finite impurity concentration c into an impurity band of width $w_{\rm imp}$ (at the choice of $j_{\rm ex} = 0.5$ and $c = 5\cdot 10^{-3}$). Notice the reduced main band gap Δ vs its unperturbed value Δ_0, the broadening $\Gamma_{\rm loc}$ of the impurity level, and also mobility gaps $\varepsilon_{\rm mob}$, $\varepsilon'_{\rm mob}$, $\varepsilon''_{\rm mob}$, separating the band-like (grey) and localized (pink) ranges. This spectrum is mirrored at $\varepsilon < 0$.

This is valid for calculation of $c\hat{B}$ at wide enough energy separation $|\varepsilon - \varepsilon_{\rm loc}|$, actual for impurity band states emerging at high enough c (but, as seen below, low enough to consider Δ unreduced). Then, doing the spatial integration in two steps, first taking residues in each period of fast oscillating $\sin k_F n$ and then summing the obtained slow envelope function [55], we arrive at the estimate: $c\hat{B} \approx c\eta(r_\varepsilon/a)^3(1+\hat{\tau}_1)$, where a is the lattice period and $\eta = \eta_1 + i\eta_2$ with $\eta_1 \sim \eta_2 \sim 1$. Then, from the NRE convergence condition, $c|\eta|(r_\varepsilon/a)^3 \lesssim 1$, the respective estimate follows for the broadening of localized level and also for the mobility edge position near $\varepsilon_{\rm loc}$ as

$$\varepsilon_{\rm loc} - \varepsilon_{\rm mob} = \Gamma_{\rm loc} \sim c^{1/3}\frac{s(s+1)}{k_F a}\frac{j_{\rm ex}^2}{1+j_{\rm ex}^2}\varepsilon_{\rm loc}. \quad (49)$$

Comparing this to the above estimate for $w_{\rm imp}$, we express the necessary condition for impurity band existence, $w_{\rm imp} \gtrsim \Gamma_{\rm loc}$, as

$$c \gtrsim c_0 = \left(\frac{j_{\rm ex}}{k_F a}\pi\rho_N\varepsilon_{\rm loc}\right)^{3/2}. \quad (50)$$

For a typical case of $j_{\rm ex} \sim 0.5$, $k_F a \sim 2$, and $\pi\rho_N\varepsilon_{\rm loc} \sim 10^{-2}$, the estimated characteristic concentration $c_0 \sim 10^{-4}$ is low enough to assure that Δ is still unreduced vs Δ_0.

Once the condition, Eq. (50), is fulfilled, the next step is to check the proper IRM criterion for the impurity band states. To this end, the inverse lifetime $\tau^{-1}_{\mathbf{k}}$ in Eq. (32) is evaluated, beyond the T-matrix approximation, by the main contribution to $\mathrm{Im}\hat{\Sigma}_{\mathbf{k}}$ from the FRE pair term in Eq. (29). For the most important vicinity of the impurity band edge ε_g, where we can set $\tilde{\varepsilon} \approx \tilde{\Delta} \approx \Delta/(1+j_{\rm ex}^2)$ and

$$\tilde{\varepsilon} - \tilde{\Delta} \approx \frac{c_0^{2/3} k_F a (1+j_{\rm ex}^2)^2}{cs(s+1)(1-j_{\rm ex}^2)}(\varepsilon - \varepsilon_g),$$

the FRE is suitably approximated by its partial version, the so-called 1st order renormalized expansion (FORE). The latter reproduces the genuine NRE structure by Eq. (30) but with the changes $\varepsilon \to \tilde{\varepsilon}$ and $\Delta \to \tilde{\Delta}$ in all its elements (labeled correspondingly by tildes). The relevant FORE pair term is $c^2\mathrm{Im}\hat{\tilde{T}}_{\rm mag}\tilde{B} \approx \Gamma_\varepsilon(1+\hat{\tau}_1)$, where

$$\Gamma_\varepsilon \approx \frac{4\pi\eta_2 c^{3/2} j_{\rm ex}(1+j_{\rm ex}^2)}{3c_0^{1/3}(1-j_{\rm ex}^2)^2}\sqrt{\frac{s(s+1)}{2k_F a}\varepsilon_{\rm loc}\left(\varepsilon - \varepsilon_g\right)},$$

just gives the estimate for quasiparticle inverse lifetime. Then the position of the respective mobility edge near ε_g is evaluated from the IRM criterion as

$$\varepsilon'_{\rm mob} - \varepsilon_g \sim \left(\frac{4\pi c}{3}\right)^2 \frac{(1+j_{\rm ex}^2)^3}{2(1-j_{\rm ex}^2)^4} w_{\rm imp} << w_{\rm imp}, \quad (51)$$

this separation being practically negligible. Thus Eq. (50) is also the sufficient condition and c_0 can be really consid-

ered the characteristic concentration of magnetic impurities for onset of in-gap impurity bands within the ranges of $\varepsilon'_{\rm mob} < \varepsilon < \varepsilon_{\rm mob}$ and its mirror for $\varepsilon < 0$. Also the separation of the $\varepsilon''_{\rm mob}$ mobility edge from the main band edge Δ is evaluated from the simple T-matrix approximation as

$$\varepsilon''_{\rm mob} - \Delta \sim \left[\frac{cs(s+1)(1-j_{\rm ex}^2)}{c_0^{2/3}k_F a(1+j_{\rm ex}^2)}\right]^2 \Delta,$$

being wider than for $\varepsilon'_{\rm mob}$, Eq. (51), but narrower than for $\varepsilon_{\rm mob}$, Eq. (49).

The c_0 value, even that low as above estimated, is much bigger of the value $c_{\rm cor} = (a/r_{\rm cor})^3 \sim c_0^2$, marking the crossover from almost isolated to correlated impurity states and so assuring collective character of impurity band states. On the other hand, it is much smaller than the estimated maximum admissible impurity concentration for the SC state, $c_{\rm max} \sim c_0^{2/3}$ (see below). So, the concentration range for impurity bands to coexist with the SC order results quite broad. Note also that the relevant inter-impurity distances for calculation of the above B-terms: $n \lesssim r_{\rm int}$, are much shorter than $r_{\rm cor}$ in Eq. (23) for the indicated band-like range, and this justifies the assumed irrelevance of $\hat{A}_{\mathbf{n}}$ exponential decay. In this condition, the system energy spectrum mostly consists of the band-like states, resulting either from the modified main bands or from the impurity bands.

3.3. Magnetic impurities at $T = 0$

In the limit of zero temperature, the use of $\hat{G}_{\mathbf{k}}$ given by Eq. (27), within the T-matrix approximation of Eq. (45), in the gap equation, Eq. (36), permits to find the numerical value of Δ for given parameters c and $j_{\rm ex}$. It should be noted that the order function $S(\Delta,T)$ resulting from Eq. (36) with use of the renormalized variables, Eq. (48), unlike its $c \to 0$ limit, Eq. (13), can be a non-monotonous and even non-analytic function of Δ (with possible jumps and breaks of derivative) and hence can generate multiple roots. A particular case of this function is presented in Fig. 7, displaying its peculiar "rhinoceros" shape. This results from the interchange of solutions for the dispersion equation, Eq. (46) with Eq. (47), depending on the relation between its parameters c, $j_{\rm ex}$ and the gap parameter Δ (considering it an independent variable in $S(\Delta,T)$).

Namely, the common (or normal) type of dispersion for impurity bands, like that shown in Fig. 6, only holds for $\Delta > \Delta_{\rm cr}(c, j_{\rm ex})$ where the critical gap value for given c and $j_{\rm ex}$ is

$$\Delta_{\rm cr}(c, j_{\rm ex}) = c\frac{s(s+1)j_{\rm ex}^3}{\pi\rho_N(1-j_{\rm ex}^2)}. \qquad (52)$$

Physically, the normal dispersion corresponds to impurity band states at $\varepsilon > 0$ (eigenvectors of $\hat{G}_{\mathbf{k}}$ matrices for given ε) that present Bogolyubov quasiparticles (specific by their

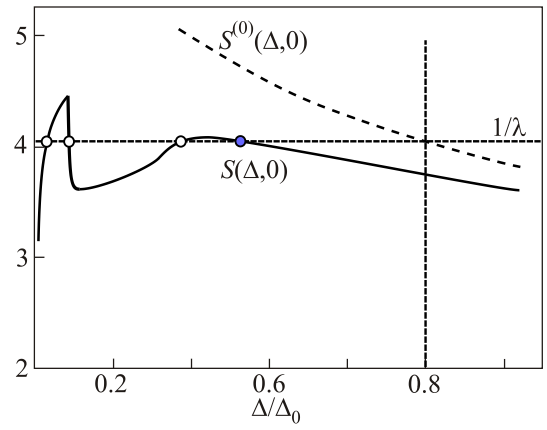

Fig. 7. The graphical solutions for the gap equation, Eq. (36), at $T = 0$ for the choice of $j_{\rm ex} = 0.5$ and $c = 0.0133$. The physical solution (dark circle) is chosen from 4 crossings of the $1/\lambda$ level with the "rhinocero-like" function S to provide the maximum value of the order parameter Δ. For comparison, the unperturbed solution $\Delta = \Delta_0$ is produced by the monotonous $S^{(0)}$ function, Eq. (13).

Bloch amplitudes enhanced on impurity sites) while those at $\varepsilon < 0$ are the related antiparticles. But if the inverse inequality, $\Delta < \Delta_{\rm cr}(c, j_{\rm ex})$, holds, the impurity bands obtain anomalous type of dispersion, being expanded from $\pm\varepsilon_{\rm loc}$ towards the main gap edges. In this case, the impurity states at $\varepsilon > 0$ would mostly refer to antiparticles and those at $\varepsilon < 0$ to particles.

Finally, the threshold condition between the two dispersion types, $\Delta = \Delta_{\rm cr}(c, j_{\rm ex})$, allows for a highly peculiar dispersionless solution with $\varepsilon^2 = \varepsilon_{\rm loc}^2$ for any ξ value (that is, collapsed impurity bands), and it can be shown that the related impurity states are "compensated" particle-antiparticle hybrids. It is just this condition that generates the vertical rear face of the "rhinocero horn", joining the normal (back) and anomalous (front) segments of $S(\Delta,T)$. This resulting function can have multiple intersections with the $1/\lambda$ level as seen in Fig. 7, unlike the unique unperturbed solution $\Delta = \Delta_0$ produced by the monotonous $S^{(0)}(\Delta,0)$. Then, as usual in thermodynamics, the choice of a single non-trivial solution should provide the maximum possible value of the order parameter, that is the highest root of the gap equation. This choice, even at continuous variation of impurity parameters c or $j_{\rm ex}$, can lead to discontinuous jumps in physical Δ.

Next, the found Δ can be used in $\hat{G}_{\mathbf{k}}$ to specify DOS from Eq. (7), displaying the restructured quasiparticle spectrum as in Fig. 6 (limited at this first step to the case of $T = 0$). With further growing c, the extension of $w_{\rm imp}$ comes to interplay with the initial decay of Δ (and of respective $\varepsilon_{\rm loc}$) and generates peculiar dynamics in the in-gap spectrum structure, qualitatively different for different $j_{\rm ex}$ values. Then all possible scenarios for SC system evolution in the considered model of magnetic impurity at $T = 0$ are suitably resumed as an "impurity coupling–impu-

rity concentration" phase diagram. It attains a universal form in the reduced variables: j_{ex} and $\bar{c} = cs(s+1)/\pi\rho_N\Delta_0$ (normalized to the above mentioned scale $\rho_N\Delta_0$ of maximum impurity concentration admissible for SC), and this $j_{ex}-\bar{c}$ diagram is shown in Fig. 8. Besides the normal phase (N) attained at high enough $\bar{c}$, it presents up to four different SC phases, distinguished by specific types of Δ and w_{imp} evolution with c at given j_{ex}. Their general configuration is characterized by the nodal points $\alpha, \beta, \gamma, \delta$ with the $j_{ex}-\bar{c}$ coordinates given in Table 1. Thus, in the initial stage of spectrum evolution with $\bar{c}$, the main band gap Δ always decreases (together with ε_{loc}) while the impurity band w_{imp} expands from ε_{loc} towards the gap center, as shown in Fig. 8. This "gap decrease–band expansion" mode agrees with conventional dynamics of the gap equation and dispersion equation (even in neglect of their coupling). The whole area presenting such behavior in the $j_{ex}-\bar{c}$ plane is denoted as the S_1 phase in the diagram. In its part of weak coupling (to the left from the α node), Δ eventually reaches a finite minimum value $\Delta_1(j_{ex})$ at some $c = c_1(j_{ex})$ (both dependent of j_{ex}), attaining a vertical slope at this point, and there remains only the trivial $\Delta = 0$ solution at $c > c_1(j_{ex})$. This is illustrated in Fig. 9 for the case of $j_{ex} = 0.35$ (along the line *1* in Fig. 8) where $\bar{c}_1(j_{ex}) \approx 1.983$ and $\Delta_1(j_{ex}) \approx 0.424\Delta_0$. Such discontinuous drop of the order parameter Δ can be considered a 1st kind transition from the S_1 SC phase to the N phase, unlike the conventional 2nd kind transition in BCS theory for pure SC materials.* This type of SC/N transition will be shown below to occur also from other SC phases in the diagram and to hold at finite temperatures, as a universal feature for SC criticality under magnetic impurities.

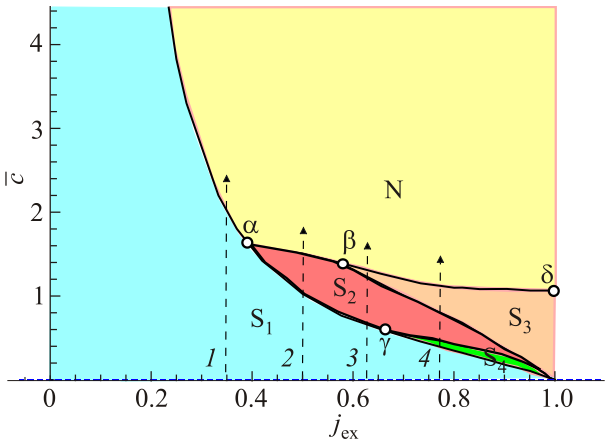

Fig. 8. (Color online) The phase diagram in reduced variables "impurity coupling–impurity concentration" for an *s*-wave SC with magnetic impurities at $T = 0$.

Table 1. Node coordinates in the diagram of Fig. 8

Node	j_{ex}	$\bar{c}$
α	0.393	1.62
β	0.584	1.37
γ	0.651	0.61
δ	1	1.065

Another SC phase is detected when tracing the spectrum evolution with $\bar{c}$ for stronger impurity coupling (to the right of the α node). Here the initial decrease of Δ with c attains vertical slope at c_1 and again drops from corresponding Δ_1 but now to the finite value $\Delta_1' = \Delta_{cr}(c_1, j_{ex})$, that is, precisely to the intercept with Eq. (52) linear law. This law generates a strikingly unconventional posterior evolution where the gap Δ increases with growing c while the impurity band w_{imp} stays collapsed to localized impurity level ε_{loc} of width Γ_{loc}, which advances also linearly in c along Eq. (52) inserted in Eq. (46). This "gap increase–band collapse" mode is realized within the SC phase denoted as S_2 in Fig. 8. For the coupling range between the α and β nodes, the $\Delta = \Delta_{cr}(c, j_{ex})$ evolution ends with the next discontinuous drop, now to zero, at some $c_2(j_{ex})$ (e.g., $\bar{c}_2(j_{ex}) \approx 1.34$ for $j_{ex} = 0.5$ in Fig. 10). This whole process can be already seen as a sequence of two 1st kind phase transitions, one between the S_1 and S_2 SC phases, and another from the S_2 to the N phase.

For yet stronger coupling, to the right of the β node, the above sequence of S_1 and S_2 phases is followed by a transition from S_2 to the next SC phase, denoted as S_3 in the diagram of Fig. 8. This transition, continuous in the order parameter Δ but with a finite break of the derivative $d\Delta/dc$ (unlike its divergence in common 2nd kind transitions), can be referred to as "semi-continuous". In the S_3 phase, Δ

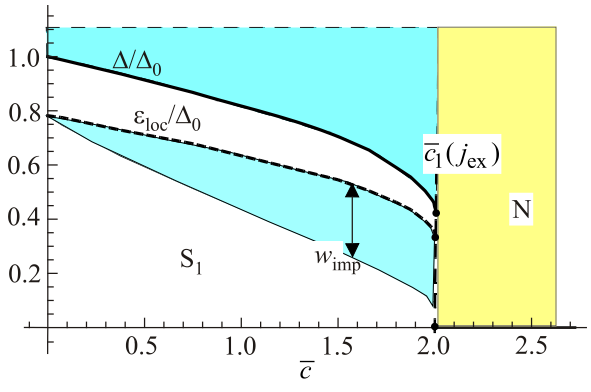

Fig. 9. (Color online) Dynamics of SC gap Δ and impurity band w_{imp} (shaded beneath the impurity level ε_{loc}) with $\bar{c}$ through the S_1 phase and their final drop to the N phase, traced along the line *1* ($j_{ex} = 0.35$) in Fig. 8.

* In fact, if the finite lifetime $\tau_{\mathbf{k}}$ for impurity band states is also accounted for, this transition is not exactly 1st kind but "quasi-1st kind", extended over a very narrow finite range of concentrations of relative width $\delta c/c \sim c^3$.

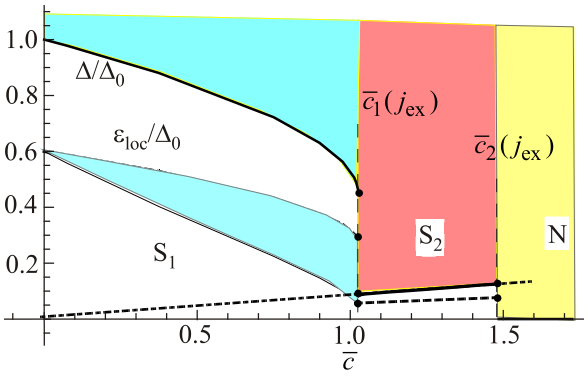

Fig. 10. (Color online) Dynamics of Δ and w_{imp} with $\bar{c}$ through the S_1 and S_2 phases, traced along the line *2* (j_{ex} = 0.5) in Fig. 8. After the 1st kind S_1/S_2 transition at $\bar{c}_1 \approx 1.015$, Δ increases by the linear law, Eq. (52) (dash-dotted line), while w_{imp} gets collapsed to the respective line of ε_{loc}. The next S_2/N 1st kind transition occurs at $\bar{c}_2 \approx 1.34$.

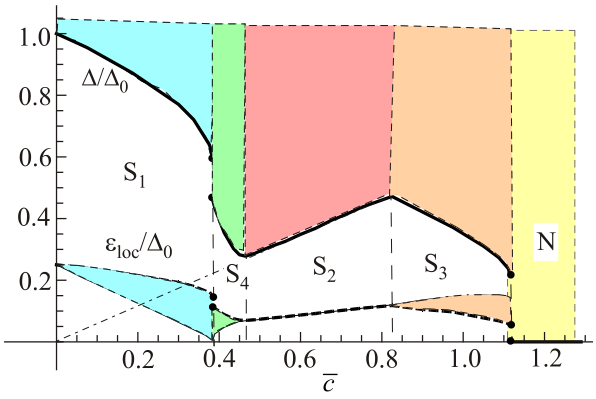

Fig. 12. (Color online) Dynamics of SC spectrum with $\bar{c}$ through the S_1, S_4, S_2 and S_3 phases along the line *4* (j_{ex} = 0.775) in Fig. 8. Besides the 1st kind, S_1/S_2 and S_3/N transitions, two "semi-continuous" S_4/S_2 and S_2/S_3 transitions are present. The dash-dotted line is for the linear law defined by Eq. (52).

returns from expansion to decay, like that in the S_1 phase, and the impurity bands revert from collapse to expansion, but in an anomalous inverse way: from $\pm\varepsilon_{loc}$ towards the main gap edges, since the inequality $\Delta < \Delta_{cr}(c, j_{ex})$ holds here and defines particle-to-antiparticle inversion. This S_3 mode follows to a final 1st kind drop into the N phase, as shown in Fig. 11.

Finally, in the range of strongest coupling, to the right of the γ node, there appears one more SC phase, in between the S_1 and S_2 phases, denoted as S_4 in the diagram. This occurs when the expansion of impurity bands with *c* ends with their merger in the gap center (at $\bar{c} \approx 0.385$ in Fig. 12).

There a discontinuous drop of Δ and ε_{loc} indicates a 1st kind transition from S_1 to S_4, and the latter phase is peculiar in its anomalous contraction of impurity bands with further growing *c*, due to growing rate of antiparticles in the particle states (and vice versa). This ends by their complete compensation and related collapse of the impurity bands at the S_4/S_2 boundary. The following S_4/S_2 transition is again of "semi-continuous" type and can be seen as a "double mirror" image of the S_2/S_3 transition (having inverted both the sign of dw_{imp}/dc and w_{imp} relative position vs ε_{loc}).

Summarizing, the considered phase diagram amounts up to 5 discontinuous and 2 "semi-continuous" transitions between 4 SC phases and the N phase. They present a variety of reentrant dynamics, as well for the SC order as for localization vs banding of quasiparticle spectra, obtained at continuous variation of external parameter (such as impurity concentration *c*) and being a direct effect of narrow impurity bands formed within the SC gap. All the unusual features observed in Figs. 9 to 12 are lost in the former theoretical scenarios shown in Fig. 13: by the simple Born approximation [7], with SC monotonous decay into the gapless phase, or by the self-consistent approximation [13], with a very broad impurity band expanding to fill completely the main band gap.

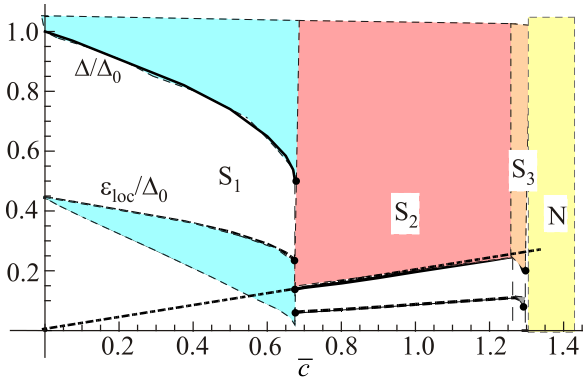

Fig. 11. (Color online) Dynamics of SC spectrum with $\bar{c}$ along the line *3* (j_{ex} = 0.62) in Fig. 8 presents S_1/S_1 and S_3/N 1st kind transitions together with the "semi-continuous" S_2/S_3 transition. The dash-dotted line follows the linear law defined by Eq. (52).

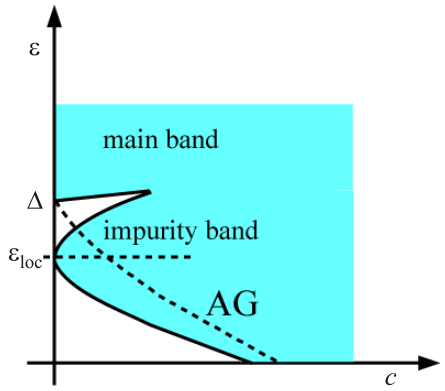

Fig. 13. (Color online) SC spectrum variation under magnetic impurities as obtained within the simplest Born approximation (AG [7], dashed line) or within the self-consistent approximation (Shiba [13], blue area).

3.4. Finite temperatures

Since the order parameter also decreases with temperature, the above indicated transitions could be more suitably observed by raising temperature at given fixed impurity concentration c (but below its maximum admissible value for chosen j_{ex} and $T = 0$). Here also a discontinuous drop of the gap equation solution $\Delta(T)$ takes place at reaching a certain critical temperature value $T_c(c)$ (see in more detail below), and it could be an alternative to the "gapless SC state" concluded from the Born approximation in Ref. 7 or from the self-consistent T-matrix approach in Ref. 13. But before this, yet other non-trivial phenomena can be observed, induced by the above described restructuring of the SC state at zero temperature. Not attempting to provide here a complete description of overall inter-coupled j_{ex}–$\bar{c}$–T dynamics, we indicate some of its notable features which appear when going to finite T from special areas in the j_{ex}–$\bar{c}$ diagram, Fig. 8, namely, from the vicinities of its phase boundaries.

To this end, we take some values of j_{ex} and $\bar{c}$, close to such boundary, and solve numerically the gap equation, Eq. (36), at finite temperatures to define the gap parameter and spectrum structure in function of T. Thus, for the choice of $j_{ex} = 0.5$ and $\bar{c} = 1$ (close to the S_1/S_2 transition at $\bar{c}_1 \approx 1.025$, on line *2* in Fig. 8), the resulting $\Delta(c,T)$ in Fig. 14 starts from the S_1 phase value $\Delta(c,0) \approx 0.506\Delta_0$ to slowly decrease with T but almost immediately reaches the 1st kind S_1/S_2 transition (here in temperature) at $T_1 \approx 0.021\Delta_0$. Thus obtained S_2 phase presents a temperature independent gap value $\Delta_2 = \Delta_0/12$ (as given by Eq. (52)) kept until the next transition, now semicontinuous, to the S_4 phase at $T_2 \approx 0.067\Delta_0$. With further growing temperature, $\Delta(c,T)$ goes non-monotonously, returning from S_4 to S_2 by another semicontinuous transition at

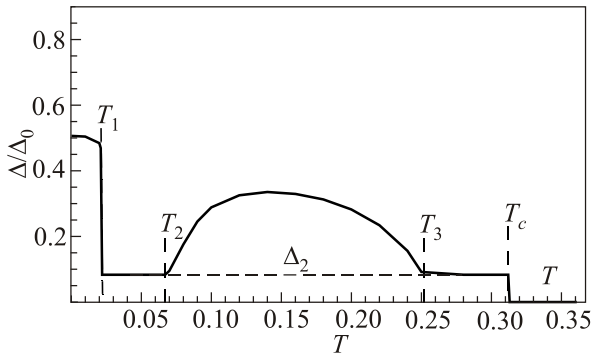

Fig. 14. Dynamics of SC gap with T at the choice of $j_{ex} = 0.5$ and $\bar{c} = 1$ (close to the S_1/S_2 boundary on line *2* in $T = 0$ in Fig. 8). Note the sequence of 1st kind S_1/S_2 transition at $T_1 \approx 0.021\Delta_0$ and "semi-continuous" S_2/S_4 transition at $T_2 \approx 0.067\Delta_0$ followed by a reentrant S_4/S_2 at $T_3 \approx 0.25\Delta_0$ and by the final 1st kind S_2/N transition at $T_c \approx 0.313\Delta_0$. Also constancy of $\Delta(T) = \Delta_2 = \Delta_0/12$ along the S_2 ranges should be noted.

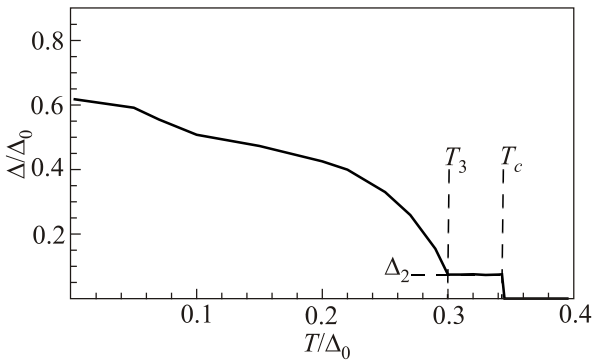

Fig. 15. The same as in Fig. 14 but with a slightly decreased c to 0.9. This results in the loss of low temperature S_1/S_2 and S_2/S_4 transitions (only leaving a shallow depression of $\Delta(T)$) and in an upshift of two final transitions.

$T_3 \approx 0.25\Delta_0$ where it keeps the same constant Δ_2 gap value until the final 1st kind drop from S_2 to N at the SC critical temperature $T_c \approx 0.313\Delta_0$.

When tracing $\Delta(c,T)$ at the same j_{ex} but with $\bar{c} = 0.9$ (that is, farther from $\bar{c}_1$ on the same line *2* in Fig. 8), its temperature evolution reveals both quantitative and qualitative changes. Namely, the initial S_1 phase does not experience in this case any low temperature transitions but only a slight depression remaining in this range (see Fig. 15), while, at going higher on, there are semicontinuous transitions, S_1/S_2 at $T_1 \approx 0.275\Delta_0$ and S_4/S_2 at $T_2 \approx 0.295\Delta_0$, and the final 1st kind S_2/N at $T_c \approx 0.343\Delta_0$. These and similar estimates permit to recover a section of the j_{ex}–$\bar{c}$–T phase diagram, tentatively sketched in Fig. 16. It displays many peculiar features, most notably, the specifically curved S_2 phase boundary giving a possibility for multiple transitions between localized and different types of delocalized impurity states at varying temperature.

Similarly, the temperature effect on SC phase configurations can be traced in other ranges of impurity coupling j_{ex} and, as shown in Fig. 17, they also include peculiar reentrant phase transitions of variable steepness and depth characteristics. Such behaviors can effectively serve for many non-trivial practical applications. For instance, at properly adjusted concentration c of impurities with given j_{ex}, Mott-like "localization-delocalization" transitions in impurity bands can be realized by driving temperature through T_2 or T_3 points, resulting in very sharp changes of related rf conductivity.

But in a more traditional aspect, tracing the critical temperature vs impurity concentration, $T_c(c)$, we only observe its common monotonous decay, which is the faster the stronger the impurity coupling j_{ex} is, as shown in Fig. 18. However, since all this critical line already corresponds to the 1st order SC/N transition (except the single $c = 0$ point), it could be accompanied by such known phenomena for 1st kind phase transitions as formation and coexistence of metastable phases, irreversibility at temperature cycling,

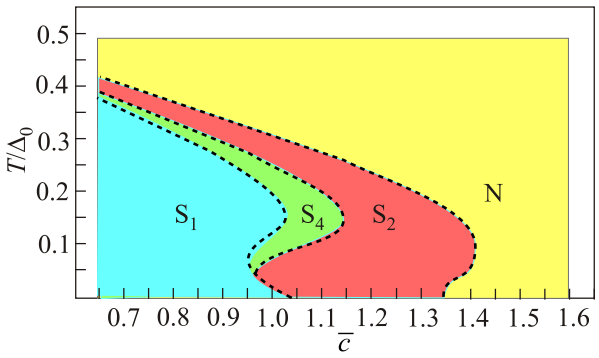

Fig. 16. (Color online) A sketch of a $\bar{c}/T$ section of the 3D $j_{ex}-\bar{c}-T$ phase diagram, taken at $j_{ex} = 0.5$, based on the data in Figs. 14, 15 (indicated by dots, together with the $T = 0$ points from line *2* in Fig. 8).

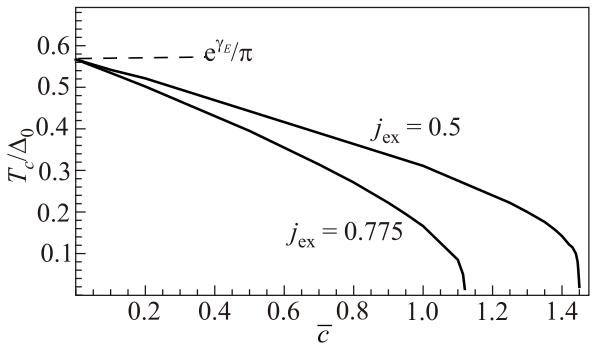

Fig. 18. The "critical temperature–impurity concentration" dependencies for an s-wave SC with magnetic impurities at two choices of their perturbation parameter j_{ex}. The $c \to 0$ limit corresponds to the BCS ratio following from Eq. (13).

etc., where these thermodynamical inhomogeneities can yet interfere with the static inhomogeneities of Bloch-like quasiparticle states within the impurity bands [39,54].

3.5. Local SC order

Finally, the analysis of the local SC order in the vicinity of a magnetic impurity site can be done in analogy with the previous case of Sec. 3.1 but with use of modified variables, Eq. (47). The resulting analytical form,

$$\frac{\Delta_{\mathbf{n}=0}}{\Delta} = 1 + \frac{j_{ex}^2}{\left(1+j_{ex}^2\right)^3}\left(\frac{1-j_{ex}^2}{2\lambda} + |\, j_{ex}\,| \arctan\frac{1-j_{ex}^2}{2\,|\, j_{ex}\,|}\right), \tag{53}$$

is presented in Fig. 19. It can be considered unconventional in its non-monotonous dependence on the perturbation parameter j_{ex}, passing from a smaller maximum at weak, $j_{ex} < 1$, to a deeper minimum at stronger, $j_{ex} > 1$, perturbation and finally tending to the bulk value in the limit of $j_{ex} \to \infty$. This mainly results from the competition between the impurity effects on the lifetime of the main band quasiparticles (the arcsinh and arctan terms in Eq. (53)) and on the depth of local level ε_{loc} (the last $\propto \pi/2$ term in Eq. (53)).

Though the above description has certain similarity with the commonly accepted picture of impurity-induced decay of the s-wave SC state through a gapless phase, it indicates a very different physics of the in-gap states and a different, 1st kind-like phase transition, mostly excluding the gapless SC phase (though some its kind is discussed below in Sec. 6). This could produce some new observable properties of such systems, for instance, in their magnetic penetration depth, specific heat, normal (rf) conductivity, optical absorption. It shows that even the well explored field of conventional SC materials still admits some unconventional impurity effects that require a special attention. In some more detail, the corresponding effects will be considered in the last section of this paper.

Now we pass to the impurity effects on the d-wave SC order, actual for HTSC cuprate systems, especially taking into account that the impurity disorder is an almost universal condition there.

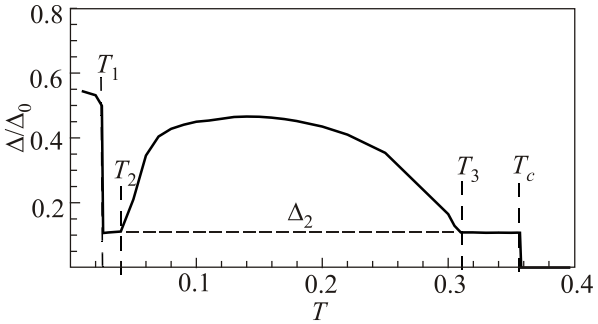

Fig. 17. A similar analysis to Fig. 14 at the choice of $j_{ex} = 0.577$ and $\bar{c} = 0.75$ (close to the S_1/S_2 boundary on line *3* in Fig. 8). A narrowing of the T_1–T_2 range, relative to that in Fig. 14, can be noted.

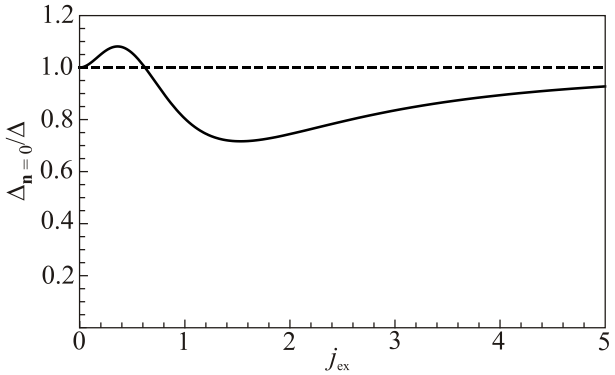

Fig. 19. The local order parameter at magnetic impurity site relative to the bulk value in function of the perturbation parameter j_{ex}. To compare with its monotonous $1/(1+v^2)$ decay at non-magnetic impurity, resulting from Eq. (40).

4. Impurity resonances in high-T_c superconducting cuprates

We start from the above referred structure of the non-perturbed locator GF matrix for the d-wave case with the smallest subdominant terms neglected for simplicity: $\hat{G}^{(0)} \approx g_0 + g_3\hat{\tau}_3$, where $g_0 \approx i\pi_N K(\Delta^2/\varepsilon^2)$, and g_3 is the same as in Eqs. (21) or (22). Consider again the case of non-magnetic point-scattering perturbation $V_{\mathbf{k}-\mathbf{k}'} = V\hat{\tau}_3$ in Eq. (14). Then the reformulated single-impurity T-matrix formally differs from that for the s-wave case, Eq. (33), only by the absence of g_1 terms:

$$\hat{T}^{(0)} = V\frac{Vg_0 + (1-Vg_3)\hat{\tau}_3}{(1-Vg_3)^2 - V^2 g_0^2}. \qquad (54)$$

But now, unlike that case, the real part of its denominator can be already zero at some energies $\pm\varepsilon_{\rm res}$, the roots of the equation $|\tilde{V}\mathrm{Re}\,g_0(\varepsilon_{\rm res})| = 1$ with the effective perturbation parameter $\tilde{V} = V/(1-Vg_3)$, analogous to the known Lifshitz equation in a normal metal [43]. They formally appear near the gap edges: $\Delta^2 - \varepsilon_{\rm res}^2 << \Delta^2$, provided the perturbation parameter modulus, $|\tilde{V}|$, exceeds the threshold value: $2/(\pi\rho_N)$, and goes deeper with growing $|\tilde{V}|$. However, since the denominator has a finite imaginary part within the gap range (due to the finite in-gap DOS by g_0), the roots $\pm\varepsilon_{\rm res}$ generally correspond to impurity resonances, like those for heavy impurities in acoustic spectra [37] or for impurities in graphene [38], instead of localized levels. For the considered SC systems with impurities, such resonances are best resolved in the STM local conductivity proportional to LDOS, Eq. (9). Their broadening is estimated as

$$\Gamma_{\rm res} \approx \left.\frac{\mathrm{Im}\,g_0}{d\mathrm{Re}\,g_0/d\varepsilon}\right|_{\varepsilon_{\rm res}}, \qquad (55)$$

and, for perturbation near the threshold, it turns out to be $\sim\Delta\ln\left[\Delta^2/(\Delta^2-\varepsilon_{\rm res}^2)\right]$, which is larger of $\varepsilon_{\rm res}$ itself. But for strong enough perturbation, such that the dimensionless parameter $v = \pi_N|\tilde{V}| >> 1$, the resonance energy estimated from the logarithmic low energy asymptotics: $\mathrm{Re}\,g_0 \approx (\pi_N\varepsilon/\Delta)\ln(4\Delta/\varepsilon)$, is low: $\varepsilon_{\rm res} \approx \Delta/[v\ln(4v)] << \Delta$ [35,36]. Then the level broadening is estimated as $\Gamma_{\rm res} \approx (\pi/2)\varepsilon_{\rm res}/\ln(4v)$, that is, smaller (though not too much) than $\varepsilon_{\rm res}$ itself.

From a more detailed treatment of Eq. (55) at intermediate perturbations, the condition for this resonance to be practically resolved, $\Gamma_{\rm res} < \varepsilon_{\rm res}$, is satisfied if $v \gtrsim e^{\pi/2}/4 \approx 1.2$ and its resolution is the better the greater v is. It should be noted that, for the effective parameter $|\tilde{V}|$ to be great, the initial perturbation parameter V does not need to be too great but close enough to the "critical" value $1/g_3$, and this condition does not look hard.

The related resonance effects in the quasiparticle spectrum can appear both in the energy dependent DOS, Eq. (7), and in LDOS, Eq. (9), with use of Eq. (54), but with a striking difference in their relative amplitude as seen in the upper panel of Fig. 20. Experimental evidence for such behavior is presented, for instance, by the case of Zn impurity in the $Bi_2Sr_2CaCu_2O_{8+\delta}$ HTSC compound where a sharp resonance was observed in the STM local conductance at $\varepsilon_{\rm res} \approx 0.03\Delta$ [40] (that corresponds to $v \approx 6.65$ or $V \approx 3.1/\pi_N$) shown in the lower panel of Fig. 20. Compared to the situation for non-magnetic impurities in s-wave sys-

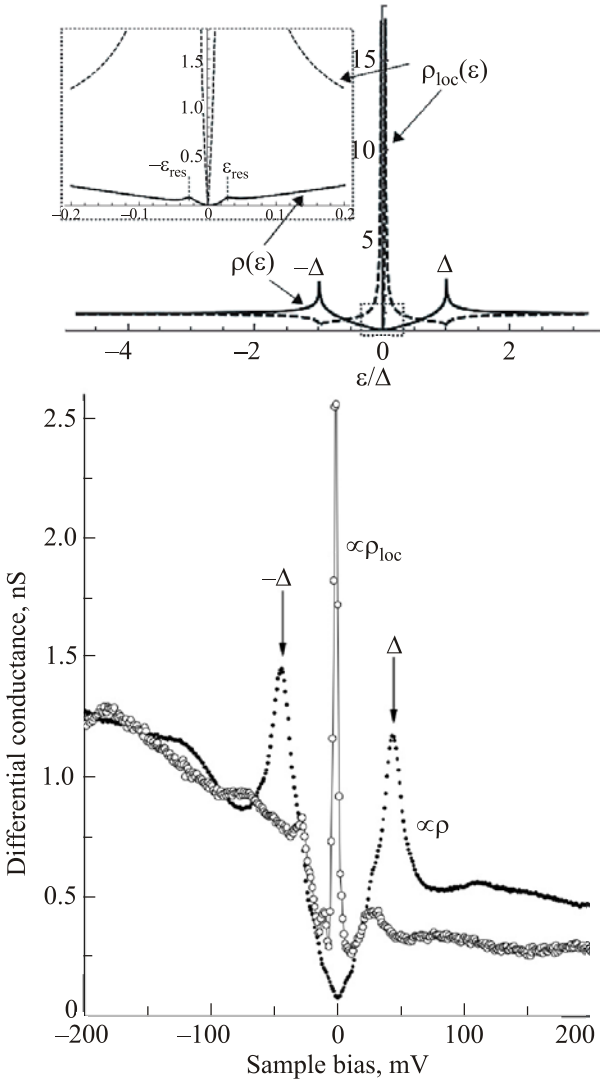

Fig. 20. Upper panel: huge resonance peaks near $\pm\varepsilon_{\rm res}$ in the calculated LDOS (dashed line) on a non-magnetic impurity site in a d-wave SC at impurity perturbation parameter $v = 6.65$ ($\varepsilon_{\rm res} = 0.03\Delta$). In contrast, very weak resonances near $\pm\varepsilon_{\rm res}$ in DOS (solid line) for this system at impurity concentration $c = 2\cdot10^{-3}$ are only seen in the inset. Lower panel: STM conductance vs sample bias in superconducting $Bi_2Sr_2CaCu_2O_{8+\delta}$ with $c = 2\cdot10^{-3}$ of Zn impurities that produce an in-gap resonance at ≈1.5 meV from the Fermi level (adapted from Ref. 40): LDOS is reflected in the data taken on Zn impurity site (open circles) while DOS does in those taken far from impurity (solid circles).

tems from Sec. 3, this resonance can be also considered an unconventional impurity effect, essentially due to the different symmetry of SC order.

The impurity effect on the uniform order parameter can be considered similarly to the *s*-wave case treated in Eq. (36), using an analogue to Eq. (16) but with the modified variables in the denominator of its integrand:

$$\tilde{\varepsilon} = \varepsilon - ic\tilde{V}\frac{vK(\Delta^2/\varepsilon^2)}{1+v^2K^2(\Delta^2/\varepsilon^2))},$$

$$\tilde{\xi} = \xi + c\tilde{V}\frac{1}{1+v^2K^2(\Delta^2/\varepsilon^2)}. \qquad (56)$$

We note the difference of these variables from those in Eq. (48), particularly in the change of $\tilde{\Delta}$ for $\tilde{\xi}$. Though, as in the case of Eq. (36), there is no analytic solution available for the resulting modified gap equation, the uniform *d*-wave gap parameter in function of the impurity concentration, $\Delta(c)$, can be again obtained from its numerical solution for given impurity perturbation parameter v. Such solutions shown in Fig. 21 display a very low sensitivity of Δ to resonant impurities up to their strongest perturbation levels and this insensitivity mainly results from the strong damping effect of finite in-gap DOS of *d*-wave quasiparticles on impurity resonances.

Calculation of the local SC order in the *d*-wave case differs from the previous scheme of Eq. (39) by presence of the non-trivial symmetry factor in the integrand, like that in Eq. (16), and results in

$$\frac{\Delta_{\mathbf{n}=0}}{\Delta} = 1-\frac{\lambda}{\pi}\mathrm{Im}\int_0^{\sqrt{\omega_D^2+\Delta^2}} d\varepsilon \frac{v^2K^2\left(\Delta^2/\varepsilon^2\right)}{1+v^2K^2\left(\Delta^2/\varepsilon^2\right)}\times$$

$$\times[K(\Delta^2/\varepsilon^2)-E(\Delta^2/\varepsilon^2)], \qquad (57)$$

involving the 2nd kind full elliptic integral E [50].

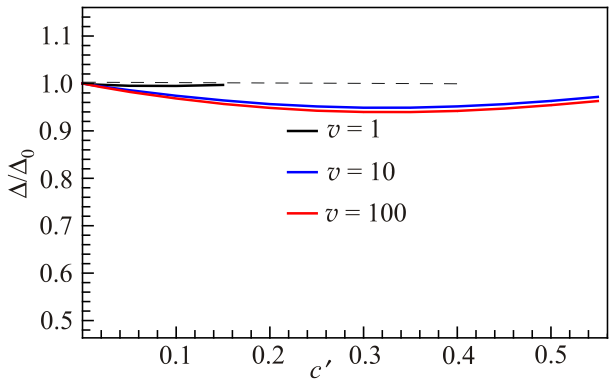

Fig. 21. (Color online) The *d*-wave relative gap parameter Δ/Δ_0 in function of the concentration c of impurities according to the numerical solution of Eq. (28) at $\omega_D/\Delta_0 = 30$ and different values of impurity perturbation parameter v (marked by colors).

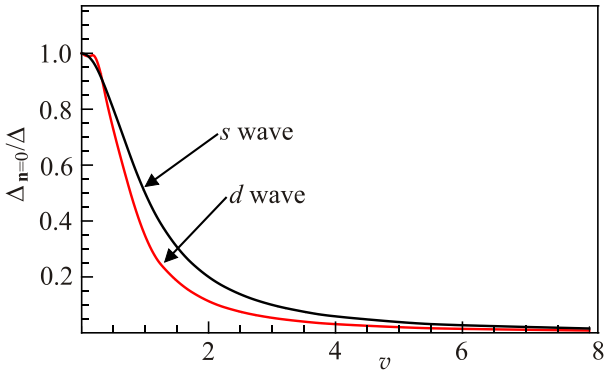

Fig. 22. (Color online) The relative local order parameter at the impurity site, $\Delta_{\mathbf{n}=0}$, in function of the non-magnetic perturbation parameter v. Comparison is shown between the *s*-wave and *d*-wave cases.

The value $\Delta_{\mathbf{n}=0}/\Delta$ for the very impurity site, numerically calculated from Eq. (57), decays with the perturbation parameter v in a very similar way to that for the *s*-wave case by Eq. (40), as shown in Fig. 22. Further on, the Friedel-like oscillations in the impurity neighborhood: $\Delta_{\mathbf{n}}/\Delta = 1-(1-\Delta_{\mathbf{n}=0}/\Delta)J_0^2(k_F n)$, presented in Fig. 23, are visibly more pronounced than those for the *s*-wave case in Fig. 5.

We can summarize the impurity effects in the *d*-wave SC systems as mostly expressed in local suppression of the SC order parameter, even stronger than in the *s*-wave case, and in enhanced local quasiparticle density near impurity centers, though not producing their true localization. Physically, this is caused by the specifics of SC symmetry with vanishing SC gap along the nodal directions, $k_x^2 = k_y^2$, preventing quasiparticles from complete localization in the impurity potential but permitting their longer stay near impurity sites.

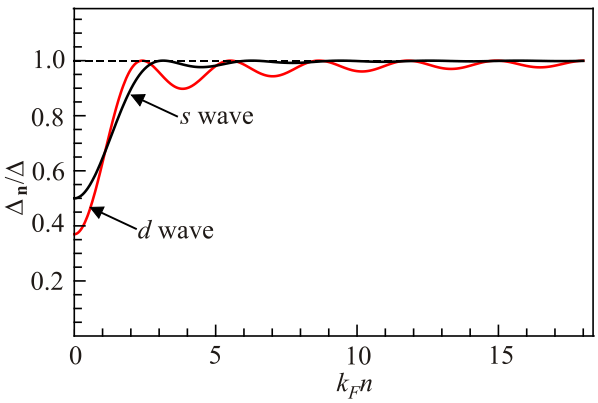

Fig. 23. (Color online) The *d*-wave relative local order parameter in function of distance n from the impurity site (in k_F^{-1} units) at the choice of $v = 1$. When compared to Fig. 5 for the *s*-wave case, a stronger initial suppression and more pronounced Friedel-like oscillations are observed.

The following consideration is given to the impurity effects in more general SC systems with multiband quasiparticle spectrum in their normal state that provides even more complex scenarios for their restructuring under impurity perturbations.

5. Impurity effects in two-gap superconductor MgB_2

Shortly after the basic theoretical concept of superconductivity as the onset of anomalous averages $\{a_{\mathbf{k},\uparrow}a_{-\mathbf{k},\downarrow}\}$ at $\mathbf{k}$ near the Fermi surface and of the related gap $\Delta_{\mathbf{k}}$ in the quasiparticle spectrum was elaborated [1,2], its generalization was proposed for the case of multiband normal electronic spectrum [56,57] with dispersion laws $\varepsilon_{l,\mathbf{k}}$ for each lth subband. Here the most significant new element compared to the above single-band case of Sec. 2.1 is in possible formation of each particular SC gap Δ_l by a combined effect of several anomalous averages, either $\langle a_{l,\mathbf{k},\uparrow}a_{l,-\mathbf{k},\downarrow}\rangle$ and $\langle a_{l',\mathbf{k},\uparrow}a_{l',-\mathbf{k},\downarrow}\rangle$ with $l' \neq l$. The subsequent treatments of such SC systems with impurities mostly generalized the initial AG approach (in the Matsubara formalism) by introducing specific SC coupling matrices $\Lambda_{ll'}$ and multiple Born relaxation time constants τ_l to find the impurity concentration dependencies for the SC critical temperature, $T_c(c)$, and for all particular gaps, $\Delta_l(c)$ [58,59].

These issues gained a new interest after experimental discovery of HTSC in the multiband electronic system of magnesium diboride MgB_2 [30,31]. Its crystalline structure consists of interchanged hexagonal layers of boron and magnesium (see Fig. 24) with the principal contribution to the Fermi states coming from boron atoms [60]. Therefore, a simplified model for description of impurity effects in this system is based on consideration of only two boron sublattices in the vertically stacked hexagonal layers. The related electronic spectrum defined both in the most rigorous first principle treatment [61,62] and in the simpler tight-binding approximation [63] presents two almost cylindrical Fermi surfaces formed by σ-subbands formed from $p_{x,y}$-orbitals and two tubular ones by π-subbands from p_z-orbitals (Fig. 25(a)). In this course, the interband hopping processes can be neglected as was suggested from symmetry reasons [61,64]. This topology can be qualitatively modeled by a combination of two bands [65], here simplified to an equivalent σ-cylinder and a π-torus (Fig. 25(b)). Their proper dispersion laws $\varepsilon_{l,\mathbf{k}}$, $l = \sigma,\pi$ can be linearized in cylindrical coordinates for quasimomentum

$\mathbf{k} = (k\cos\varphi, k\sin\varphi, k_z)$: $\xi_{\sigma,\mathbf{k}} = \varepsilon_{\sigma,\mathbf{k}} - \varepsilon_F \approx v_\sigma(k - k_\sigma)$ and

$$\xi_{\pi,\mathbf{k}} = \varepsilon_{\pi,\mathbf{k}} - \varepsilon_F \approx v_\pi\left[\sqrt{(k-k_M)^2 + k_z^2} - k_\pi\right].$$

Here k_M is the distance between the Γ and M points of the hexagonal prism Brillouin zone (see Fig. 25(b)), and the particular Fermi velocities v_l and quasimomenta k_l are then adjusted to fit the 4-subband parameters obtained from first-principle calculations.

The corresponding two-band BCS Hamiltonian

$$H_{BSC2} = \sum_{l=\sigma,\pi}\sum_{\mathbf{k}}\psi^\dagger_{l,\mathbf{k}}\left(\xi_{l,\mathbf{k}}\hat{\tau}_3 + \Delta_{l,\mathbf{k}}\hat{\tau}_1\right)\psi_{l,\mathbf{k}} \qquad (58)$$

contains the Nambu spinors $\psi^\dagger_{l,\mathbf{k}} = (a^\dagger_{l,\mathbf{k},\uparrow}, a^\dagger_{l,-\mathbf{k},\downarrow})$ for each lth subband and realizes an extension of the single band Hamiltonian by Eq. (5). While it is reasonable to neglect the $\sigma-\pi$ interband transitions in the MgB_2 normal state [61], there appears an implicit correlation between both bands resulting from the above referred interconnection of SC order parameters. This is expressed in the extension of single SC coupling parameter λ, as introduced in Sec. 2.1, to the 2×2 matrix $\hat{\lambda}$ in σ,π-indices and the related set of two coupled gap equations (cf. to Eq. (36) for the single-band case):

$$\Delta_\sigma = \lambda_{\sigma\sigma}S(\Delta_\sigma,T)\Delta_\sigma + \lambda_{\sigma\pi}S(\Delta_\pi,T)\Delta_\pi,$$

$$\Delta_\pi = \lambda_{\pi\sigma}S(\Delta_\sigma,T)\Delta_\sigma + \lambda_{\pi\pi}S(\Delta_\pi,T)\Delta_\pi, \qquad (59)$$

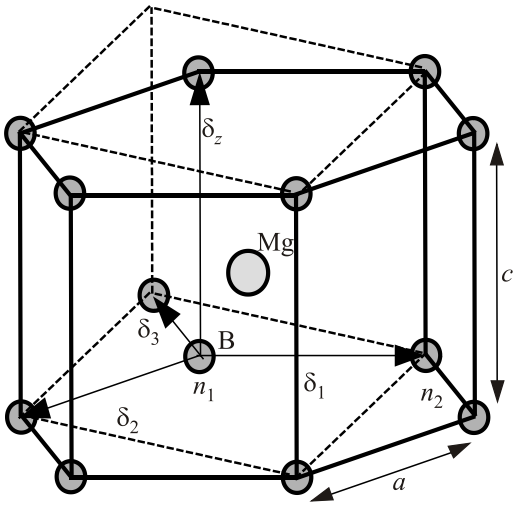

Fig. 24. Crystalline structure of the MgB_2 compound.

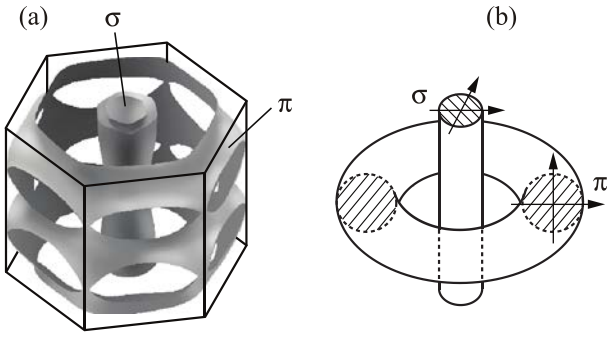

Fig. 25. Structure of normal state Fermi surfaces for MgB_2 by first-principle calculations (a) and its simplification to a minimal two-band model (b).

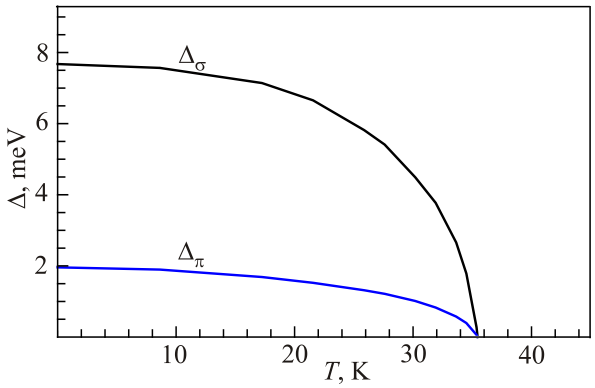

Fig. 26. Decrease of π- and σ-gaps in pure SC MgB_2 with temperature.

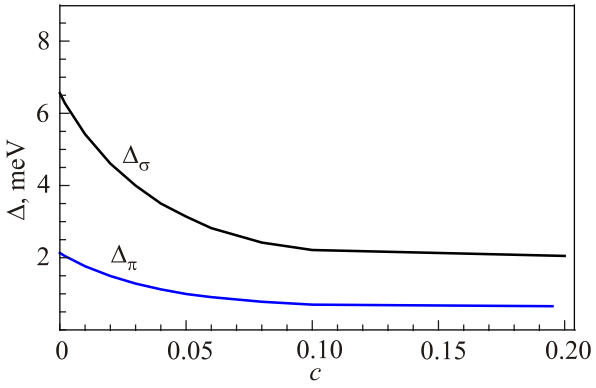

Fig. 27. Decrease of π- and σ-gaps in SC MgB_2 with concentration c of non-magnetic impurities at the choice of dimensionless perturbation parameters $v_\sigma = v_\pi = v = 1$.

equivalent to the known expressions by Refs. 56, 57, 59. Its numerical solution at the choice of $\hat{\lambda}$ matrix elements: $\lambda_{\sigma,\sigma} = 0.28$, $\lambda_{\sigma,\pi} = 0.05$, $\lambda_{\pi,\sigma} = 0.07$, $\lambda_{\pi,\pi} = 0.06$, results in the temperature dependencies of two gap parameters (in absence of impurities) shown in Fig. 26, in a fair agreement with their experimental measurements for MgB_2 [60].

Next, the impurity perturbations on this system can be introduced in a similar way to the considerations in Sec. 3, in order to analyze the difference between their non-magnetic and magnetic types. For simplicity, this consideration will be limited to zero temperature, though its generalization to finite temperatures, like that in Sec. 3, does not present much problems.

5.1. The case of non-magnetic impurities

Here, the effect of non-magnetic impurity is modeled by the two-band extension of the perturbation Hamiltonian, Eq. (25):

$$H_{\text{imp2}} = \frac{1}{N}\sum_{l=\sigma,\pi}\sum_{\mathbf{p},\mathbf{k},\mathbf{k}'} e^{i(\mathbf{k}'-\mathbf{k})p}\psi^{\dagger}_{l,\mathbf{k}} V_l \hat{\tau}_3 \psi_{l,\mathbf{k}'}, \quad (60)$$

where the interband scatterings are also neglected by the same symmetry reasons as above. Then the concentration dependence of gap parameters follows from the modification of Eq. (59), analogous to that of Eq. (13) into Eq. (36), resulting in the specific forms for the *S*-functions to be used in Eq. (59)

$$S(\varepsilon,\Delta_l) = \frac{1}{\sqrt{\varepsilon^2-\Delta_l^2}}\left(\pi - \arctan\frac{2\zeta_l\omega_D}{\omega_D^2-\varepsilon^2+\Delta_l^2-\zeta_l^2}\right), \quad (61)$$

with $\zeta_l = cV_l v_l/(1+v_l^2)$, a partial analogue to Eq. (37) for the single-band *s*-wave case. The numerical solution of the system, Eqs. (59), (61), is presented in Fig. 27, displaying the qualitative similarity with the single band case in Fig. 4. It can be noticed that while both gaps decay with impurity concentration, their ratio Δ_σ/Δ_π stays almost unchanged (within to about a percent).

A more detailed picture of the quasiparticle spectrum is given by the respective DOS function, obtained from the general Eq. (7) where the quasimomentum sum is naturally divided into σ- and π-parts with corresponding partial Fermi densities $\rho_{\pi,\sigma}$ and, after using the renormalized GF's $\hat{G}_{\mathbf{k}}$ with the impurity partial parameters $\zeta_{\pi,\sigma}$, it is well approximated (within to subdominant terms, like those in Eqs. (21), (22)) as

$$\rho(\varepsilon) \approx \sum_{l=\sigma,\pi}\rho_l \frac{\varepsilon}{\sqrt{\varepsilon^2-\Delta_l^2}}. \quad (62)$$

Thus, it is nothing more then a weighted sum of two partial BCS functions by Eq. (12) but with the modified gaps $\Delta_l \equiv \Delta_l(c)$ (as shown in Fig. 27), the only impurity effect occurring in this case. The resulting behavior of two-band DOS at the choice of $\rho_\pi/\rho_\sigma = 3$ (to fit the experimental estimates of these weights for pure MgB_2 [60]), $v_\sigma = v_\pi = v = 1$ (as in Fig. 27) and $c = 0.01$ is presented in Fig. 28, only differing from the unperturbed MgB_2 case by the (unequal) shifts of σ- and π-band edges.

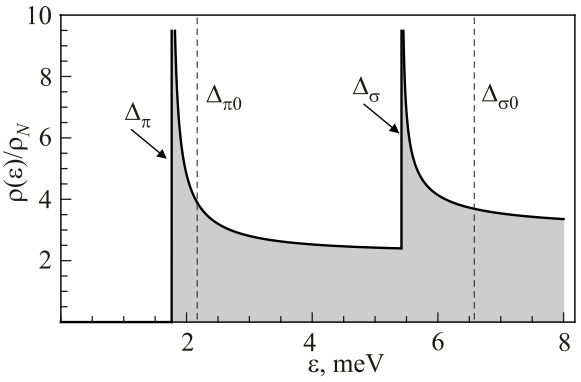

Fig. 28. Calculated DOS for SC MgB_2 with non-magnetic impurities differs only in the shifts of σ- and π-band edges from that for pure MgB_2 (dashed lines).

5.2. The case of magnetic impurities

As it could be expected, a much more diversified spectrum modification is obtained for the case of magnetic impurities. Here we again employ the model perturbation of the kind used in Sec. 3.2 but with two exchange operators: $V_{\text{mag},l} = J_l s_{\mathbf{p}} \boldsymbol{\tau}$, each acting on a respective spectrum branch. Then, evidently, a single impurity produces two Shiba levels: $\varepsilon_{\text{imp},l} = \Delta_l (1 - j_{\text{ex},l}^2)/(1 + j_{\text{ex},l}^2)$, located within each lth gap. So, at least one localized level $\varepsilon_{\text{imp},\pi}$ always exists in the spectrum. As to the second level, $\varepsilon_{\text{imp},\sigma}$, it can also correspond to a localized state (if it occurs inside the π-gap), or otherwise to a resonance.*

The condition for existence of the second localized level is that the impurity exchange parameter $j_{\text{ex},\sigma}$ should surpass the critical value:

$$j_{\text{ex}}^{(\text{cr})} = \sqrt{\frac{\Delta_\sigma - \Delta_\pi}{\Delta_\sigma + \Delta_\pi}}, \tag{63}$$

and, for instance, with the experimental Δ_l values for pure MgB_2, this value amounts to $j_{\text{ex}}^{(\text{cr})} \approx 0.7$.

Next, in the same way as for the single band case, we define the dependencies of two gaps on concentration of magnetic impurities at different values of the parameter $j_{\text{ex},\lambda}$. The calculation using Eqs. (58), (59) with modified variables $\tilde{\varepsilon}_l$ and $\tilde{\Delta}_l$, analogous to those in Eq. (47) but using respective parameters $h_{\text{ex},l}$ and $\varepsilon_{\text{imp},l}$, involves two corresponding order parameters Δ_l and two order functions $S(\Delta_l, T)$ weighted with the SC coupling parameters $\lambda_{l,l'}$. The resulting evolution of $\Delta_l(c,T)$ is affected by the interplay between possible "rhinocero-like" singularities in both order functions, as illustrated in Fig. 29 where the two lines in the Δ_σ–Δ_π plane present graphical solutions of the gap equations system, Eq. (59), resolved for the two S-functions through the inverse $\hat{\lambda}$ matrix:

$$S(\Delta_\sigma, T) = (\lambda^{-1})_{\sigma,\sigma} + (\lambda^{-1})_{\sigma,\pi} \Delta_\pi / \Delta_\sigma,$$

$$S(\Delta_\pi, T) = (\lambda^{-1})_{\pi,\pi} + (\lambda^{-1})_{\pi,\sigma} \Delta_\sigma / \Delta_\pi. \tag{64}$$

For the adopted $\hat{\lambda}$ matrix elements, we have $(\lambda^{-1})_{\sigma,\sigma} \approx 0.365$, $(\lambda^{-1})_{\pi,\pi} \approx 17$, $(\lambda^{-1})_{\sigma,\pi} \approx -0.304$, $(\lambda^{-1})_{\pi,\sigma} \approx -0.426$. Some examples of resulting two-gap evolution in function of reduced impurity concentration $\bar{c}$, as defined in Sec. 3.2 (here, for simplicity, we take both $j_{\text{ex},l}$ values as equal), at $T = 0$ are presented in Fig. 30. Comparing them to the single band cases in Figs. (9)–(12), we observe similar discontinuous drops of both Δ_l at 1st kind transitions (including that to the normal state) and emergence of ranges of their anomalous growth with growing c at strong enough j_{ex}. However the two-gap situation

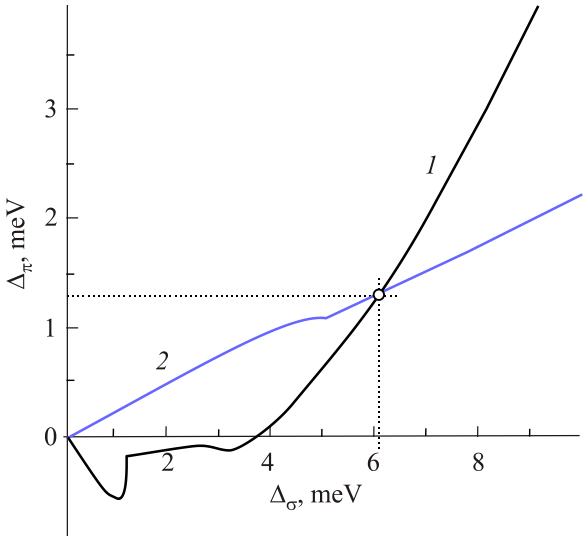

Fig. 29. (Color online) Numeric solution of the system, Eq. (64), for π- and σ-gaps in SC MgB_2 containing magnetic impurities with reduced parameters of exchange coupling $j_{\text{ex}} = 0.775$ and concentration $\bar{c} = 0.7$. This case is close to the phase transition which occurs when, with further growing $\bar{c}$, the crossing between the black line (*1*) (presenting the first line in Eq. (64)) and the blue line (*2*) (the second line in Eq. (64)) reaches the break point of the blue line.

has also its own specifics. Thus, the range between $\bar{c} \approx 1.27$ and $\bar{c} \approx 2.2$ in Fig. 30(c) where both Δ_σ and Δ_π gaps are growing with $\bar{c}$ corresponds to a collapsed state like that in the S_2 phase for the single band case, but only for the impurity σ-band, while the impurity π-band has growing and inverted dispersion here, like that in the S_3 phase. Otherwise, the latter band is found collapsed and Δ_π gap is growing in the range between $\bar{c} \approx 0.8$ and $\bar{c} \approx 0.9$, but the Δ_σ gap decays here and the impurity σ-band has growing and normal dispersion like that in the S_1 phase (see below). In total, the evolution scenario in Fig. 30(c) reveals up to 6 different SC phases and, generally, the case of two-gap SC with magnetic impurities (if also admitting non-equal $j_{\text{ex},l}$) is expected to present yet greater diversity of SC phases and transitions between them.

The following step is again to calculate the DOS function. Evidently, its form is more involved here than in the case of non-magnetic impurities, due to the effects of the impurity levels with their extension into narrow impurity bands. In the same spirit of Sec. 3.2, we estimate by analogies with Eq. (49) the characteristic concentrations $c_{0,l}$ for such bands to really exist. For parameters of MgB_2, these values are $\sim 10^{-4}$, that is again well below $c_{\max}$. This allows treatment of the general Eq. (7) with the modified variables $\tilde{\varepsilon}_l$ and $\tilde{\Delta}_l$ in its σ- and π-parts and readily leads to the DOS profiles as given in Fig. 31.

* Its finite lifetime in this case will be due to any weak interband hopping, irrelevant for all other purposes.

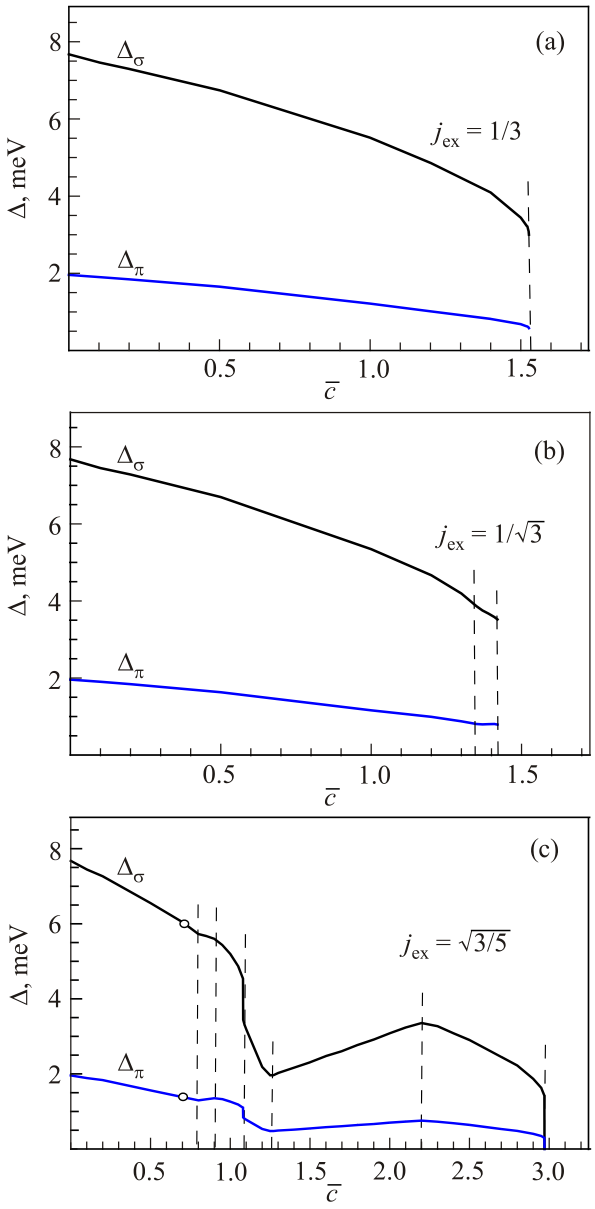

Fig. 30. Decrease of π- and σ-gaps in SC MgB_2 with concentration of magnetic impurities at two different values of their exchange coupling parameters $j_{ex,\sigma} = j_{ex,\pi} \equiv j_{ex}$, below and above the critical value given by Eq. (63). The circles in panel (c) indicate the values of each gap at $\bar{c} = 0.7$ accordingly to the solution presented in Fig. 29.

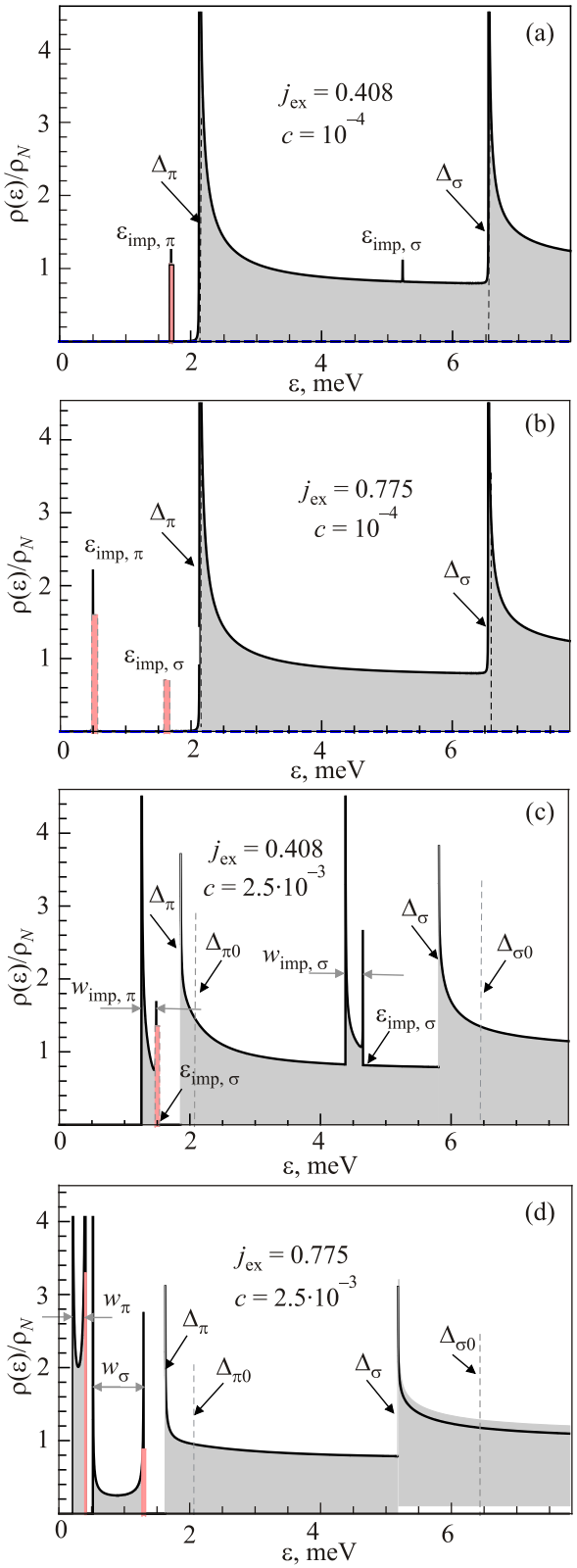

Fig. 31. Calculated DOS in SC MgB_2 with magnetic impurities at different values of their exchange coupling and concentration.

They demonstrate all the expected features of spectrum restructuring with growing concentration c of magnetic impurities. At lowest concentrations, $c < c_{0,l}$ (Fig. 31(a), (b)), the lower impurity level $\varepsilon_{imp,\pi}$, lying inside the SC gap, gives rise to localized quasiparticle states, mostly on π-orbitals near an impurity atom, while weak interactions between such states produce a small broadening $\Gamma_{loc,\pi}$ (an analog to the single-band case, Eq. (49) and Fig. 6) of this level. The nature of the states corresponding to the other level, $\varepsilon_{imp,\sigma}$, depends on the value of exchange parameter $j_{ex,\sigma}$ vs $j_{ex}^{(cr)}$. For its subcritical value (as in Fig. 31(a)) they are of resonance type with broadening $\Gamma_{res,\sigma}$ (an analog to Eq. (55)), having maximum partial Bloch amplitudes

on σ-orbitals near impurity atoms and much smaller ones on π-orbitals in the host crystal. But they turn out to be fully localized on σ-orbitals near impurity atoms at energies within the π-gap for an overcritical $j_{ex,\sigma}$ value (as in Fig. 31(b)). At higher concentrations, $c >> c_{0,l}$ (Figs. 31(c), (d), an impurity band of width w_l develops from each lth level towards the Fermi level. Then the w_π bands consist of band-like states built from π-orbitals, but with their Bloch amplitudes having strong maxima near impurity atoms. And it is only in narrow $\Gamma_{loc,\pi}$ vicinities of $\pm\varepsilon_{imp,\pi}$ levels that the quasiparticle states are localized, but over rather big clusters of impurities (see in more detail in Ref. 39). The structure of w_σ bands again depends on $j_{ex,\sigma}$ vs $j_{ex}^{(cr)}$, containing only band-like states on σ-orbitals (with maxima on impurity atoms) for subcritical $j_{ex,\sigma}$ (Fig. 31(c)) and combining band-like w_σ range with localized $\Gamma_{loc,\sigma}$ range (like their π-analogs but composed from σ-orbitals) for the overcritical case (Fig. 31(d)). We notice that for the major concentration range, until the SC collapse at c_{max}, the initial s-wave gap gets filled with a number of new bands of different symmetry joined with localized states, all being in dynamical interaction. This complex picture of in-gap spectrum evolution confirms again the conclusion by the single-band case of Sec. 3.2 on incompleteness of the simple concept of "gapless" SC state resulted from self-consistent averaging of impurity effects.

Such diversity of possible localized and delocalized states and transitions between them would naturally result in a number of peculiar observable impurity effects in thermodynamical (including the before considered change of the kind of SC transition), kinetic, optical, magnetic, etc., properties of such multiband systems. But for their experimental observation and possible applications, an important practical issue is the real position of a magnetic impurity and its exchange coupling J_{ex} with the host quasiparticles. The available experimental data [66,67] indicate that magnetic impurities in the MgB_2 compound occupy mostly the Mg positions which can essentially reduce their J_{ex} value and make the above discussed effects hardly observable.

Thus, the measured almost linear $T_c(c)$ decay in $Mg_{1-c}Mn_cB_2$, though being quite notable: $dT_c(c)/dc \approx$ ≈ -159 K [68], but from comparison with the initial linear dependencies in Fig. 30 it only permits to expect any unconventional features at $c \sim |dT_c(c)/dc|/T_c(0) \sim 0.25$, rather too high concentration levels either for their experimental realization or for validity of the present theory. Nevertheless, other data on nominally the same but specially prepared single crystal $Mg_{1-c}Mn_cB_2$ [69] showed a much faster T_c decay, vanishing at $c_{max} \sim 0.01$. This already gives a hope to find some unconventional behaviors as, e.g., 1st order transitions or S_2-plateaus at varying temperature, similar to those in Figs. 14, 15, or 17, in such prepared samples with properly adjusted c values in the $[0, c_{max}]$ range. A more detailed theoretical approach to the case of Mn impurity in MgB_2 [70], though limited to the single impurity case, rather supports this possibility.

On the other hand, the observed effect by Fe impurities in MgB_2 [71] more resembles that for the non-magnetic case in Fig. 27. Possibly, this can be due to a strong reduction of the magnetic J-term in the impurity potential, Eq. (25), for this case and its domination by the non-magnetic V-term.

Our consideration of such effects will be continued in further detail in the next section devoted to impurity effects in SC iron pnictides, where the multiband electronic structure is combined with an alternative type of SC symmetry.

6. Impurity effects in superconducting iron pnictides

The discovery of HTSC in the family of doped iron pnictide compounds [32,33] has motivated a great interest towards these materials. Unlike the cuprate family [28], that present insulating properties in their initial undoped state, the typical iron pnictide LaOFeAs compound is a semimetal when undoped. The STM study [72] established that this material has a layered structure, where the relevant structure for SC is the FeAs layer with a 2D square lattice of Fe atoms and out-of-plane As atoms located above or below the centers of square cells (Fig. 32). Its electronic structure, important for constructing microscopic SC models, have been explored with high-resolution angle-resolved photoemission spectroscopy (ARPES)

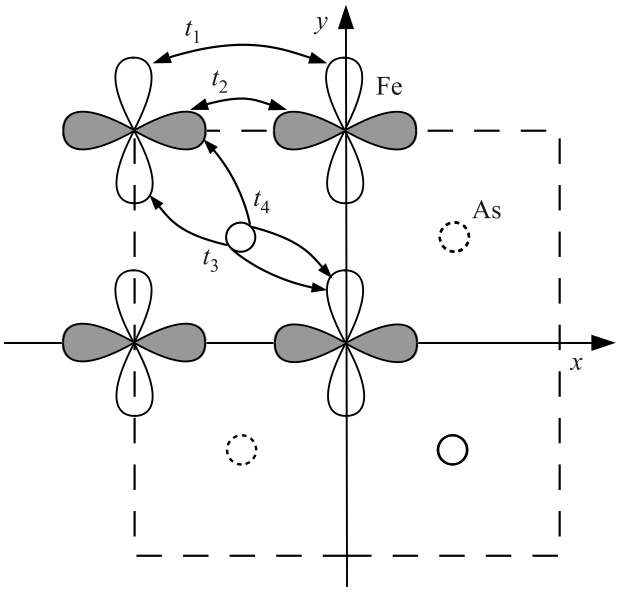

Fig. 32. Schematics of a FeAs layer in the LaOFeAs compound with d_{xz} (white) and d_{yz} (dark) Fe orbitals and the Fe–Fe hopping parameters in the minimal coupling model. Note that the hoppings ($t_{3,4}$) between next near neighbors are mediated by the As orbitals (out of Fe plane).

techniques [73,74]. Their results indicate a multiple connected structure of the Fermi surface, consisting of electron and hole pockets, and absence of nodes in both electron and hole gaps [73], suggesting that these systems display the so-called extended *s*-wave SC order, with opposite signs of the order parameter on the electron and hole segments [75].

To describe this band structure, the first principles numeric calculations are commonly used, outlining the importance of Fe atomic *d*-orbitals. The calculations show that SC in these materials is associated with Fe atoms in the layer plane, represented in Fig. 32 by their orbitals and the related hopping amplitudes. The dominance of Fe atomic 3*d*-orbitals in the DOS of the LaOFeAs compound near its Fermi surface was demonstrated by the local density approximation (LDA) calculations [75–80]. It was then concluded that the multi-orbital effects are important for the electronic excitation spectrum in the SC state, causing formation of two gaps: one for electron and another for hole pockets on the Fermi surface.

To explain the observed SC properties, it is suggested that these materials may reveal an unconventional pairing mechanism, beyond the common electron–phonon scheme [81,82]. In general, the total of 5 atomic orbitals for each iron in the LaOFeAs compound can be involved, however, ways to reduce this basis are sought, in order to simplify analytical and computational work. Some authors [83,84] have suggested that it is sufficient to consider only the d_{xz} and d_{yz} Fe orbitals. This minimal coupling model, based on two orbitals with properly adjusted model parameters (energy hopping and chemical potential), provides the Fermi surface with the same topology that follows from the first principles calculations.

Having established the SC state parameters for doped iron pnictides, one can also study the impurity effects in them. Similarly to doped perovskite cuprates, here impurity centers can result both from the dopants, necessary to form the SC state itself, and from foreign atoms and other local defects in the crystalline structure. Within the minimal coupling model, a possibility for localized impurity levels within SC gaps in doped LaOFeAs was indicated even for non-magnetic impurities [85,86]. Such an essential difference from the case of traditional *s*-wave gap on a single-connected Fermi surface by Sec. 3.1 is due to the presence of additional symmetry and the question naturally rises on possible collective behavior of such states at high enough impurity concentrations. This was considered by the authors [55], using the GF techniques, similar to those for doped cuprates in Sec. 4, within the minimal two-orbital coupling model for iron pnictide electronic structure and supposing the simplest isotopic type of impurity perturbation. Below we discuss formation of impurity bands and corresponding phase states in these systems, in extension of the before presented results for conventional SC materials.

6.1. Impurity effects in the minimal model for a $s_{\pm}$-wave superconductor

In more detail, the minimal coupling model [83,84] for the non-perturbed LaOFeAs considers two types of local Fe orbitals, d_{xz} (or x) and d_{yz} (or y), on sites of the square lattice with lattice parameter a and 4 hopping parameters between nearest (NNs) and next nearest (NNNs) neighbors:

i) t_1 for xx or yy NNs along their orientations, and t_2 across them, and

ii) t_3 for xx or yy NNNs, and t_4 for xy NNNs.

The resulting band Hamiltonian is diagonal in quasimomentum $\mathbf{k}$ and spin σ, but non-diagonal with respect to the orbital indices of the 2-spinors $\psi^{\dagger}(\mathbf{k},\sigma) = (x^{\dagger}_{\mathbf{k},\sigma}, y^{\dagger}_{\mathbf{k},\sigma})$:

$$H_t = \sum_{\mathbf{k},\sigma} \psi^{\dagger}(\mathbf{k},\sigma)\hat{h}(\mathbf{k})\psi(\mathbf{k},\sigma). \tag{65}$$

Here the energy matrix in the orbital basis is expanded in Pauli matrices $\hat{\sigma}_i$: $\hat{h}(\mathbf{k}) = \varepsilon_{+,\mathbf{k}}\hat{\sigma}_0 + \varepsilon_{-,\mathbf{k}}\hat{\sigma}_3 + \varepsilon_{xy,\mathbf{k}}\hat{\sigma}_1$ with the energy factors $\varepsilon_{\pm,\mathbf{k}} = (\varepsilon_{x,\mathbf{k}} \pm \varepsilon_{y,\mathbf{k}})/2$, and

$$\varepsilon_{x,\mathbf{k}} = -2t_1 \cos ak_x - 2t_2 \cos ak_y - 4t_3 \cos ak_x \cos ak_y,$$

$$\varepsilon_{y,\mathbf{k}} = -2t_1 \cos ak_y - 2t_2 \cos ak_x - 4t_3 \cos ak_x \cos ak_y,$$

$$\varepsilon_{xy,\mathbf{k}} = -4t_4 \sin ak_x \sin ak_y. \tag{66}$$

It is readily diagonalized at passing from the orbital to subband basis: $\hat{h}_b(\mathbf{k}) = \hat{U}(\mathbf{k})\hat{h}(\mathbf{k})\hat{U}^{\dagger}(\mathbf{k})$, with the unitary matrix $\hat{U}(\mathbf{k}) = \exp(-i\hat{\sigma}_2\theta_{\mathbf{k}}/2)$ and $\theta_{\mathbf{k}} = \arctan(\varepsilon_{xy,\mathbf{k}}/\varepsilon_{-,\mathbf{k}})$. The resulting eigen energies for electron and hole subbands are

$$\varepsilon_{h,e}(\mathbf{k}) = \varepsilon_{+,\mathbf{k}} \pm \sqrt{\varepsilon^2_{xy,\mathbf{k}} + \varepsilon^2_{-,\mathbf{k}}}, \tag{67}$$

and respective electron and hole segments of the Fermi surface (see Fig. 33) are defined by the equations $\varepsilon_{e,h}(\mathbf{k}) = \varepsilon_F$. A reasonable fit to the LaOFeAs band structure given by the more detailed LDA calculations [78] is attained with the parameter choice (in $|t_1|$ units) of $t_1 = -1$, $t_2 = 1.3$, $t_3 = t_4 = -0.85$ [80].

The SC state of such a multiband electronic system is suitably described in terms of "multiband-Nambu" 4-spinors $\Psi^{\dagger}_{\mathbf{k}} = (\alpha^{\dagger}_{\mathbf{k},\uparrow}, \alpha_{-\mathbf{k},\downarrow}, \beta^{\dagger}_{\mathbf{k},\uparrow}, \beta_{-\mathbf{k},\downarrow})$ with the multiband spinor $(\alpha^{\dagger}_{\mathbf{k},\sigma}, \beta^{\dagger}_{\mathbf{k},\sigma}) = \psi^{\dagger}(\mathbf{k},\sigma)\hat{U}^{\dagger}(\mathbf{k})$. It generates another extension of the Hamiltonian, Eq. (65), in addition to Eq. (58) for two-band MgB_2, in the 4×4 matrix form:

$$H_s = \sum_{\mathbf{k},\sigma} \Psi^{\dagger}_{\mathbf{k}} \hat{h}_s(\mathbf{k}) \Psi_{\mathbf{k}}. \tag{68}$$

Here the 4×4 matrix $\hat{h}_s(\mathbf{k}) = \hat{h}_b(\mathbf{k}) \otimes \hat{\tau}_3 + \Delta_{\mathbf{k}}\hat{\sigma}_0 \otimes \hat{\tau}_1$ includes, besides the orbital Pauli matrices $\hat{\sigma}_j$, also the Pauli matrices $\hat{\tau}_j$ acting on the Nambu (particle-antiparticle)

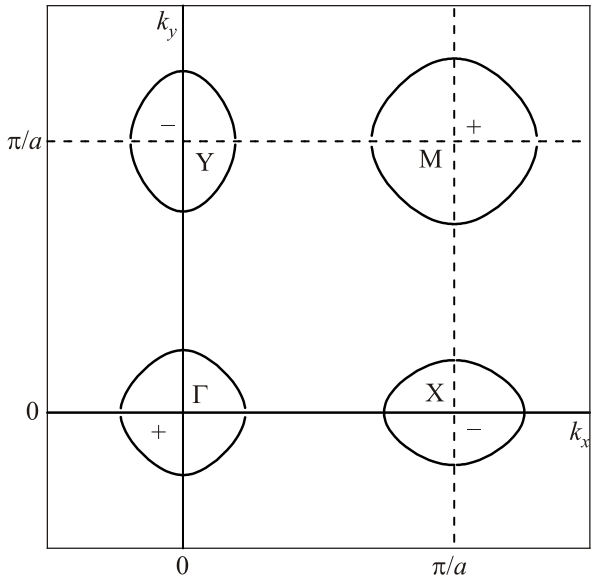

Fig. 33. Electron (–) and hole (+) segments of the Fermi surface in the normal state of model system with electronic spectrum given by Eq. (67). The center of first Brillouin zone is displaced by $(\pi/2a, \pi/2a)$ to fully include all the segments around four characteristic points Γ, X, M, and Y in this zone.

indices in Ψ-spinors. The simplified form for the extended *s*-wave gap function takes constant values, $\Delta_{\mathbf{k}} = \Delta$ on the electron segments and $\Delta_{\mathbf{k}} = -\Delta$ on the hole segments.

For the non-perturbed system described by Eq. (65), the respective GF 4×4 matrices, $\hat{G}_{\mathbf{k},\mathbf{k}'} = \langle\langle \Psi_{\mathbf{k}} \mid \Psi^{\dagger}_{\mathbf{k}'} \rangle\rangle$, are diagonal in quasimomentum: $\hat{G}_{\mathbf{k},\mathbf{k}'} = \delta_{\mathbf{k},\mathbf{k}'}\mathbf{k}'\hat{G}_{\mathbf{k}}$, with

$$\hat{G}_{\mathbf{k}} = \frac{\varepsilon\hat{\tau}_0 + \varepsilon_e(\mathbf{k})\hat{\tau}_3 + \Delta\hat{\tau}_1}{2d_{e,\mathbf{k}}} \otimes \hat{\sigma}_e + \frac{\varepsilon\hat{\tau}_0 + \varepsilon_h(\mathbf{k})\hat{\tau}_3 - \Delta\hat{\tau}_1}{2d_{h,\mathbf{k}}} \otimes \hat{\sigma}_h, \qquad (69)$$

$$\hat{\sigma}_{e,h} = \left(\hat{\sigma}_0 \pm \hat{\sigma}_3\right)/2, \quad d_{j,\mathbf{k}} = \varepsilon^2 - \varepsilon_j^2(\mathbf{k}) - \Delta^2.$$

To simplify the treatment of impurity perturbations, the band structure is approximated to identical circular electron and hole Fermi segments of radius k_F around respective BZ points $\mathbf{K}_{e,h}$ and to identical linear dispersion of normal state quasiparticles near the Fermi level ε_F: $\varepsilon_e(\mathbf{k}) - \varepsilon_F = \hbar v_F(|\mathbf{k} - \mathbf{K}_e| - k_F)$ and $\varepsilon_h(\mathbf{k}) - \varepsilon_F = -v_F(|\mathbf{k} - \mathbf{K}_h| - k_F)$. Moreover, we shall describe the contributions of both segments to overall electronic properties by a single quasimomentum variable ξ, identified with both electron $\xi_e = \varepsilon_e(\mathbf{k}) - \varepsilon_F$ and hole $\xi_h = \varepsilon_h(\mathbf{k}) - \varepsilon_F$ ones.

Next, the Hamiltonian of the disordered SC system is chosen as $H = H_s + H_{\text{imp}}$ including, besides H_s, Eq. (67), the term due to non-magnetic impurities [85] on random sites $\mathbf{p}$ in Fe square lattice with an on-site energy shift V (supposed positive without loss of generality). It is written in the multiband-Nambu spinor form as

$$H_{\text{imp}} = \frac{1}{N}\sum_{\mathbf{p},\mathbf{k},\mathbf{k}'} e^{i(\mathbf{k}'-\mathbf{k})\cdot\mathbf{p}} \Psi^{\dagger}_{\mathbf{k}} \hat{V}_{\mathbf{k},\mathbf{k}'} \Psi_{\mathbf{k}'} \qquad (70)$$

with the 4×4 scattering matrix $\hat{V}_{\mathbf{k},\mathbf{k}'} = V\hat{U}^{\dagger}(\mathbf{k})\hat{U}(\mathbf{k}') \otimes \hat{\tau}_3$. Under this perturbation, the GFs are again presented in the general forms by Eqs. (29) or (30), respective for band-like or localized energy ranges. The corresponding T-matrix:

$$\hat{T} = \frac{V}{1+v^2} \frac{v\varepsilon\sqrt{\Delta^2 - \varepsilon^2} - \left(\Delta^2 - \varepsilon^2\right)\hat{\tau}_3}{\varepsilon^2 - \varepsilon_{\text{loc}}^2}, \qquad (71)$$

is diagonal in the subband indices in and displays the in-gap impurity levels $\varepsilon_{\text{loc}} = \Delta/\sqrt{1+v^2}$ [84] with the dimensionless impurity perturbation parameter $v = \pi\rho_N V$. This essential difference from the T-matrix defined by Eq. (35) for non-magnetic impurities in single-band *s*-wave SC, Sec. 3.1, is just due to the $s_{\pm}$-symmetry. It assures cancelation of non-diagonal elements in the locator $\hat{G}$ matrix obtained from Eq. (69) and thus a non-trivial behavior of the T-matrix denominator. On the other hand, when comparing such in-gap levels with those by magnetic impurities, Sec. 3.2, they are also insensitive to the sign of perturbation parameter (here V) but only can reach zero energy in the limit of $V^2 \to \infty$.

Following the line of Sec. 3.2, the restructured band spectrum at finite impurity concentration c is obtained from the dispersion equation (in the same T-matrix approximation):

$$D_{\mathbf{k}}(\varepsilon) = \det \hat{G}_{\mathbf{k}}^{-1}(\varepsilon) = \left(\tilde{\varepsilon}^2 - \tilde{\xi}_e^2 - \Delta^2\right)\left(\tilde{\varepsilon}^2 - \tilde{\xi}_h^2 - \Delta^2\right) = 0, \qquad (72)$$

with the renormalized energy and momenta forms

$$\tilde{\varepsilon} = \varepsilon\left(1 - \frac{cVv}{1+v^2}\frac{\sqrt{\Delta^2 - \varepsilon^2}}{\varepsilon^2 - \varepsilon_{\text{loc}}^2}\right),$$

$$\tilde{\xi}_j = \xi_j - \frac{cV}{1+v^2}\frac{\Delta^2 - \varepsilon^2}{\varepsilon^2 - \varepsilon_{\text{loc}}^2}. \qquad (73)$$

Notice also the $s_{\pm}$-symmetry related difference of this case from Secs. 3 and 5, namely, in non-trivial renormalization for momenta $\tilde{\xi}_j$ (instead of gap parameters), producing different behavior of renormalized spectrum and subsequent physical properties at variation of c and/or T.

The roots of Eq. (72) with the variables, Eq. (73), define up to 8 subbands, shown in Fig. 34: 4 main bands (*m*-bands), for particles and antiparticles in the BZ *e*- and *h*-segments, $\pm\varepsilon_{e,h}^{(m)}$, and 4 impurity bands (*i*-bands), with energies near $\pm\varepsilon_{\text{loc}}$ and momenta in the same segments.

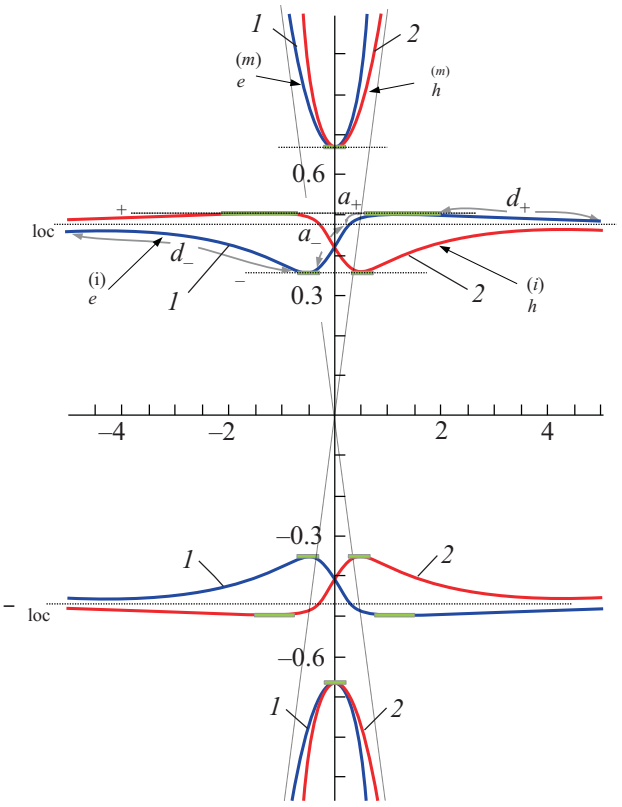

Fig. 34. (Color online) Dispersion laws for SC LaOFeAs system with non-magnetic impurities at the choice of impurity parameters $v = 1$ and $\bar{c} = 0.6$. For convenience, the energy bands, resulting from Eq. (72) in the electron (*1*) and hole (*2*) parts of Brillouin zone in function of respective quasimomentum variables $\xi_{e,h}$, are superposed as functions of the same variable ξ. The grey arrows indicate the ascending and descending ranges of the $\varepsilon_e^{(i)}$ band, the rectangles near the band edges indicate the ranges of localized states and related mobility edges.

The dispersion laws for the *m*-bands in function of the above introduced single variable ξ are approximated as

$$\varepsilon_{e,h}^{(m)}(\xi) \approx \sqrt{\xi^2+\Delta^2} \pm \frac{cV}{1+v^2}\frac{\xi^3}{\left(\xi^2+v^2\varepsilon_{\rm loc}^2\right)\sqrt{\xi^2+\Delta^2}}, \qquad (74)$$

and their difference from that for the pure SC, Eq. (67), is mainly in a slight $\xi \leftrightarrow -\xi$ asymmetry (due to renormalization of $\tilde{\xi}_{e,h}$) and in the *c*-dependence of the gap parameter Δ (analyzed below). Another difference is their finite inverse lifetime

$$1/\tau^{(m)} \approx \frac{cVv}{1+v^2}\left|\frac{\xi\sqrt{\xi^2+\Delta^2}}{\xi^2+\Delta^2-\varepsilon_{\rm loc}^2}\right|, \qquad (75)$$

that defines the validity range of Eq. (74) from the IRM criterion as $\xi \gtrsim c/(\pi\rho_N)$. The separation of corresponding mobility edges from the gap edges is estimated as

$$\varepsilon_{\rm mob} - \Delta \sim \frac{c^2}{c_0}\Delta, \qquad (76)$$

including

$$c_0 = \left(\frac{\pi\rho_N\varepsilon_{\rm loc}}{2k_Fa}\frac{v}{1+v^2}\right)^2, \qquad (77)$$

the characteristic impurity concentration for *i*-bands formation [87]. The latter presents an analogy to Eq. (50) for magnetic impurities in the common *s*-wave SC, but being even lower in the small parameter $\pi\rho_N\varepsilon_{\rm loc}$, due to the 2D dimensionality of the present system.

The dispersion laws for *i*-bands are more suitably obtained from Eqs. (72), (73) in the inverted form as

$$\xi = \xi_{\pm,\varepsilon} = \frac{cV\left(\Delta^2-\varepsilon^2\right)}{\left(1+v^2\right)\left(\varepsilon^2-\varepsilon_{\rm loc}^2\right)} \pm \sqrt{\tilde{\varepsilon}^2-\Delta^2}, \qquad (78)$$

defining a peculiar non-monotonous function $\varepsilon_e^{(i)}(\xi)$ (see Fig. 34) between its limits $\varepsilon_\pm$, the roots of the equation $\tilde{\varepsilon}^2 = \Delta^2$. The positive sign in Eq. (78) applies to the ascending part of this function within the $[\varepsilon_-, \varepsilon_{\rm loc}]$ range (or the a_- range) and to its descending part within the $[\varepsilon_{\rm loc}, \varepsilon_+]$ range (the d_+ range), while the negative sign does, respectively, to the d_- and a_+ ranges. In the same way, the $\varepsilon_h^{(i)}(\xi)$ law follows from the $\xi = -\xi_{\pm,\varepsilon}$ equation. The main qualitative difference of this structure from the single-band case by Sec. 3.2 consists in that the resulting impurity band $[\varepsilon_-, \varepsilon_+]$ embraces its generating impurity level $\varepsilon_{\rm loc}$ and thus realizes a "bilateral" dispersion type. In particular, this prevents the actual system from appearance of a dispersionless state, like the S_2 phase from Sec. 3.2, and of the related "rhinocero-horn" singularities in the order function $S(\Delta, T)$ (see Fig. 35 below). Nevertheless, the presence of in-gap impurity bands in the spectrum generates a non-monotonous behavior of this function, discussed in what follows.

At low enough impurity concentrations, $c << c_0^{1/2}$, approximate analytic expressions: $\varepsilon_\pm - \varepsilon_{\rm loc} \approx \approx \pm cVv^2/[2(1+v^2 \pm \sqrt{1+v^2})$, define linear in *c* growth of *i*-band width: $w_{\rm imp} = cV$. But it becomes slower at $c \sim c_0^{1/2}$ when this growth feels also an essential interference from the reduction of $\Delta(c)$. Its numerical treatment, like that for the systems considered in Secs. 3.2 and 5, is presented below.

Again, as in the above mentioned systems, the validity range for the formal dispersion laws, Eq. (78), is restricted by the IRM criterion, Eq. (33), where the relevant inverse lifetime for given ε:

$$1/\tau^{(i)} \sim \frac{c^2Vv}{\left(k_Fa\right)^3}\left[\frac{v^2\varepsilon_{\rm loc}^2}{\left(1+v^2\right)\left|\varepsilon^2-\varepsilon_{\rm loc}^2\right|}\right]^4 \qquad (79)$$

(note its difference from $1/\tau^{(m)}$, Eq. (75)) is defined by the higher GE terms beside the T-matrix, Eq. (71). Then the

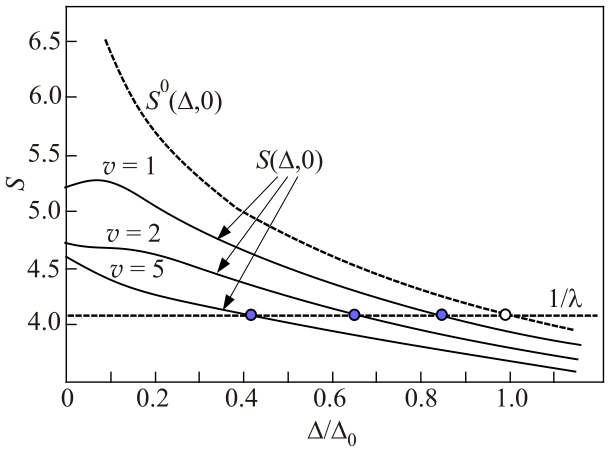

Fig. 35. Non-monotonous (and analytical) behavior of the SC order function $S(\Delta,0)$ for LaOFeAs with non-magnetic impurities at different choices of impurity perturbation parameter v and $\bar{c} = 0.3$ in comparison with the non-perturbed $S^0(\Delta,0)$. Note the absence of breaks, like those in Fig. 7 for the single-band system, and the change from negative to positive ending curvature for $S(\Delta \to 0,0)$ at stronger perturbations.

respective estimates for the mobility edges $\varepsilon_{\text{mob},\pm}$ near the i-band edges follow as

$$\varepsilon_+ - \varepsilon_{\text{mob},+} \sim \varepsilon_{\text{mob},-} - \varepsilon_+ \sim \left(\frac{c_0}{c}\right)^4 w_{\text{imp}} << w_{\text{imp}}. \qquad (80)$$

These limitations also restrict the admissible quasimomentum ξ values near the related extremal points, $\xi_\pm \approx$ $\approx (\varepsilon_{\text{loc}} \pm \Delta)\varepsilon_{\text{loc}}/\Delta$, to beyond their vicinities: $|\xi - \xi_\pm| \gtrsim$ $\gtrsim \xi_\pm (c_0/c)^2$ (narrow enough at $c >> c_0$).

Another peculiar feature of the present case is in absence of such restriction for the states near the very impurity levels $\pm\varepsilon_{\text{loc}}$, since their localization is "shortcutted" by the highly mobile quasiparticle states with permitted ξ values from the $[\xi_-, \xi_+]$ range (granting long enough IRM lifetime for all the states at the same energy).

At least, for $c < c_0$, all the in-gap states are localized and more adequately described by NRE for $\hat{G}_{\mathbf{k}}$ (this issue being left beyond the scope of the present study) while the main bands are still defined by Eqs. (73), (76).

Now, the analysis of the gap equation for this system can begin from the case of $T = 0$, with use of the actual GF forms by Eqs. (71)–(73) in the general Eq. (8), resulting in the specific forms for the order function $S(\Delta,0)$ as shown in Fig. 35. Their shape, in particular, the ending curvature sign, changes with varying the impurity parameters c and v, and this will be seen to also produce some specific SC phases in the present system, though different from those in Secs. 3.2 and 5.

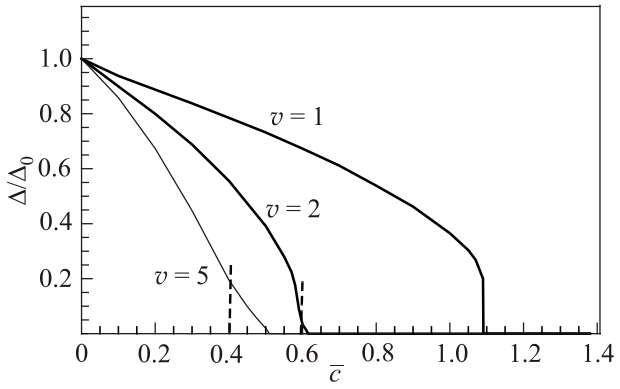

Fig. 36. Evolution of SC gap in LaOFeAs with non-magnetic impurities at $T = 0$ and different choices of impurity perturbation parameter v in function of reduced impurity concentration $\bar{c} = c/(\pi\rho_N\Delta_0)$. At stronger v values, deviations from the initial decay mode appear within the ending c ranges (delimited by the dashed lines).

Such phase separation can be concluded from the concentration dependencies for the $s_\pm$-wave order parameter, $\Delta = \Delta(c)$, at different values of the impurity perturbation parameter v, as shown in Fig. 36.

When comparing them with the single band case of Figs. 9–12, we notice appearance of another type of $\Delta(c)$ behavior near the final S/N transition. Here its monotonous decay ends with a 1st order discontinuous drop to zero only at lower v values, as for the $v = 1$ curve in Fig. 36 (at negative ending curvature of corresponding $S(\Delta,0)$ in Fig. 35). But at high enough v, a deviation from this decay mode appears near its end (at positive ending S-curvature), $\Delta(c)$ reaching zero with a finite slope, that resembles "semi-continuous" transitions from Sec. 3.2 (but those never being S/N transitions). Notably, this anomalous c range turns broader with growing v, as seen from comparison between the $v = 2$ and $v = 5$ curves in Fig. 36.

More information on these processes comes from the numerical treatment of related quasiparticle spectra, represented by their DOS and the diagrams analogous to the single-band Figs. 9–12. Thus, such a diagram for the $v = 1$ case is shown in Fig. 37 and demonstrates a similarity to the single-band Fig. 9, with only difference in more closeness of the "bilateral" i-band to the m-band gap edge at the S/N transition at the maximum value of impurity reduced concentration $\bar{c}_{\max} \approx 1.09$.

But the corresponding diagram at higher $v = 2.5$ in Fig. 38 reveals the mechanism for the ending anomaly in this case. Namely, it is seen that the bottom of "bilateral" i-band reaches zero (the center of m-band gap) at $\bar{c}_1 \approx 0.54$ and, unlike the case of S_1/S_4 transition in Fig. 12 from Sec. 3.2, stays fixed there at further growing c, indicating formation of a "gapless" SC state (with $\Delta(c)$ staying finite and very close to the i-band top). This phase (denoted S_{gl}) exists here within a relatively narrow concentration

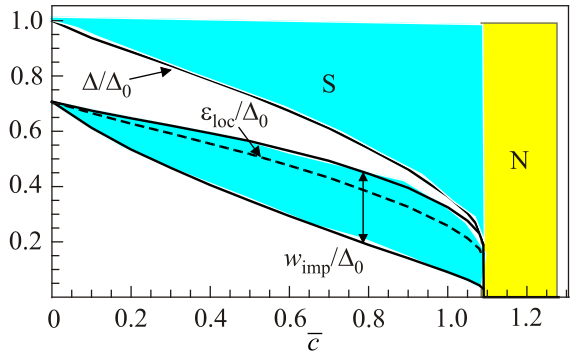

Fig. 37. (Color online) Evolution of the SC gap Δ, the in-gap impurity level ε_{loc}, and the impurity bandwidth w_{imp} at $T = 0$ and $v = 1$ in function of $\bar{c}$.

range from $\bar{c}_1$ to $\bar{c}_{max} \approx 0.57$, presenting almost linear decay of $\Delta(c)$ and of the related ε_{loc} to zero. As seen from Fig. 36, the S_{gl} range in c rapidly grows with growing v. Evidently, despite a certain formal similarity with the traditional AG concept of gapless phase, this spectrum structure is very different from that in its origin and its dynamics under external factors.

Next, in the same analogy with the single-band case, the analysis can be extended to finite temperatures and some of its results are briefly indicated in Fig. 39. Here, the comparison with the single-band case in Figs. 14, 15, and 17 confirms the above suggestion regarding the absence of dispersionless SC phases in the present system (by absence of temperature independent plateaus on the Δ vs T curves). Nevertheless, these curves also present a non-monotonous behavior, including even an anomalous growth of Δ with T, at higher v values and this can be related with the existence of the gapless, S_{gl}, phase there and with closeness of the system at $T = 0$ and chosen c to this phase (as seen in Fig. 39). Thus, a possibility for peculiar device applications can be sought in such systems, even with common non-magnetic impurities.

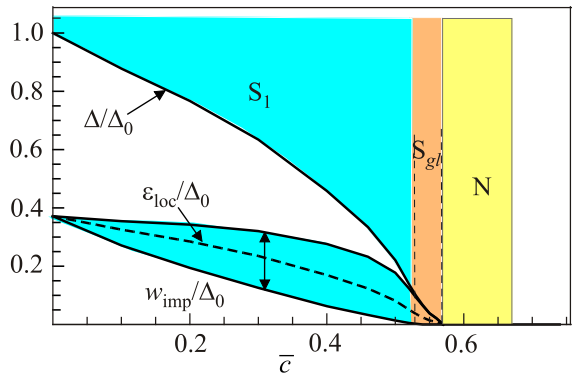

Fig. 38. (Color online) The processes analogous to those in Fig. 35, but at the choice of $v = 2.5$. Notice the onset of a narrow gapless phase in the range of $0.54 < \bar{c} < \bar{c}_{max} = 0.57$.

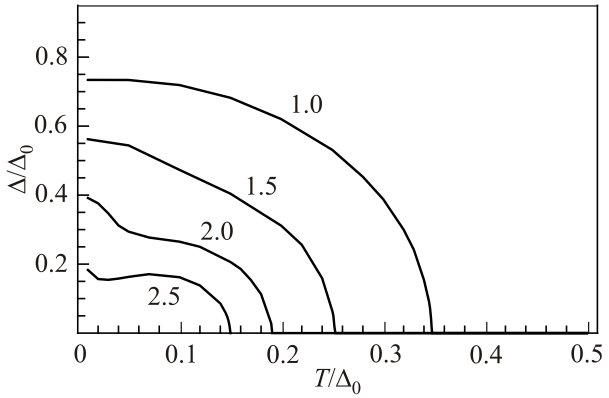

Fig. 39. Evolution of SC gap in LaOFeAs with non-magnetic impurities at different choices of impurity perturbation parameter v (shown as labels near each curve) and $\bar{c} = 0.5$ in function of temperature T. Note the emergence of anomalous non-monotonous behavior at stronger v values.

Finally, the critical SC transition temperature vs non-magnetic impurity concentration c is shown in Fig. 40 and its comparison with the corresponding Fig. 18 for the case of magnetic impurities in the single-band system reflects the difference between their modes of reaching zero at various choices of impurity perturbation parameters. They suggest that, for the present system, unlike the single-band one, such transition is mostly realized through the gapless phase, whose width depends on the chosen v value. Also, a difference between the modes in which Δ and T_c vanish with c (and, hence, the lack of common Δ/T_c universality) can be noticed when comparing Figs. 36 and 40.

From the available experimental data, a strong suppression of SC order in LaOFeAs with non-magnetic Zn substitutes for Fe was already detected [88–90] and attributed to their specific pair-breaking effect in presence of the $s_{\pm}$

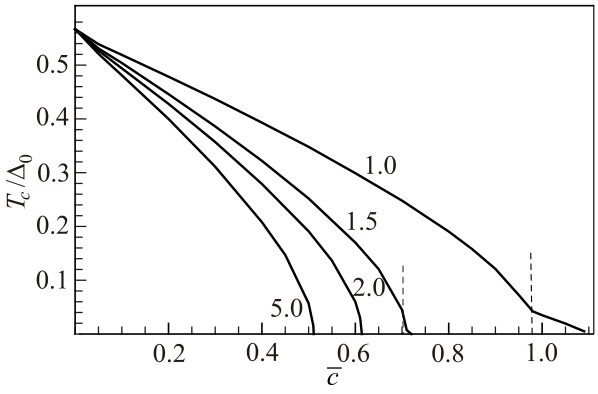

Fig. 40. SC critical temperature for LaOFeAs with non-magnetic impurities in function of reduced impurity concentration $\bar{c}$ (the curves labeled by the chosen v values). The corresponding S/N transitions at these curves are realized through the gapless phase except for their final sections at weaker v, indicated by the dashed lines.

symmetry of this order. Also, a similar effect was found to be produced by Co substitutes in the $BaFe_2As_2$ iron pnictide [91]. To confirm all other theoretical consequences of this effect, a more detailed further study is needed.

6.2. Observable effects by the in-gap impurity states

In-gap impurity states, either localized and band-like, can produce notable effects on various thermodynamical properties of disordered superconductors, as the SC order parameter and transition critical temperature (that were already discussed in the previous Sections), and also the London penetration depth λ_L, electronic specific heat $C_{\rm el}$, etc. [87]. Thus, the superfluid density n_s in the London formula, $\lambda_L = \sqrt{mc^2/(4\pi e^2 n_s)}$, can be expressed in the semi-classical approach [92] as

$$n_s = n - \int_0^\infty d\varepsilon \rho(\varepsilon) \operatorname{sech}^2 \frac{\varepsilon}{2T}. \tag{81}$$

Then, after inserting Eqs. (69) and (71)–(73) in the general Eq. (7) to obtain the DOS $\rho(\varepsilon)$, the numerical treatment of Eq. (81) leads to the temperature dependence of λ_L shown in Fig. 41, visibly slower than its known behavior in the pure SC system. Experimentally, a similar variation of the decay rate of $\lambda_L(T)$ in the $BaFe_2As_2$ iron pnictide with different impurity substitutes for Fe was reported in Ref. 93.

Next, the expression for the electronic specific heat:

$$C_{\rm el} = \frac{\partial}{\partial T} \int_0^\infty \varepsilon \rho(\varepsilon) \tanh \frac{\varepsilon}{2T} d\varepsilon, \tag{82}$$

after being numerically integrated and differentiated (with a notable contribution from $\partial\Delta(c,T)/\partial T$ taken into account), results in the behavior presented in the common logarithmic form in Fig. 42. Its most notable new feature, compared to the conventional almost linear dependence on inverse temperature for unperturbed system (dashed line), is a clear break of the characteristic exponent at a rather low temperature (here $T_b \sim \Delta_0/14$) that can be attributed to the effect by quasiparticles excited at the low lying bottom edge of the impurity band (see in Fig. 37). Also, this break differs from that found for the same system in the low concentration limit [55] with only a narrow $\Gamma_{\rm loc}$ range of localized states being present near the impurity level $\varepsilon_{\rm loc}$.

But besides those, other effects, specific for new quasiparticle bands only, can be expected on kinetic properties of the disordered material, while the localized impurity states should have practically no effect on them. Such phenomena can be naturally described in terms of the above indicated GF matrices as seen in what follows. Thus, the Kubo–Greenwood formalism [94,95] gives such expression for the (frequency and temperature dependent) electrical conductivity that describes optical absorption at given frequency ω:

$$\sigma(\omega,T) = \frac{e^2}{\pi} \int_{-\infty}^{\infty} d\varepsilon \, \frac{f_F(\varepsilon') - f_F(\varepsilon)}{\omega} \int d\mathbf{k} v_x(\mathbf{k},\varepsilon) v_x(\mathbf{k},\varepsilon') \times$$

$$\times \operatorname{Tr}\left[\operatorname{Im} \hat{G}_{\mathbf{k}}(\varepsilon) \operatorname{Im} \hat{G}_{\mathbf{k}}(\varepsilon') \right], \tag{83}$$

where $\varepsilon' = \varepsilon - \omega$, $f_F(\varepsilon) = (e^{\varepsilon/T} + 1)^{-1}$ is the Fermi occupation function, and the electric field is applied along the x-axis. When using the above derived GF's, Eq. (69), with the impurity renormalized variables, Eq. (73), in this formula, the generalized velocity functions are defined as $v(\mathbf{k},\varepsilon) = \nabla_{\mathbf{k}} \operatorname{Re} D_{\mathbf{k}}(\varepsilon) / [\partial \operatorname{Re} D_{\mathbf{k}}(\varepsilon)/\partial\varepsilon]$ [87], and they result in the physical quasiparticle velocities at $\varepsilon = \varepsilon^{(j)}(\xi)$, for

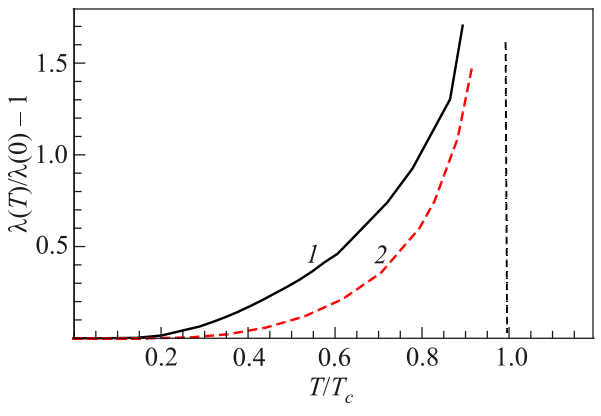

Fig. 41. Low temperature decay of the London penetration depth λ_L in LaOFeAs with impurities at $v = 1$ and $\bar{c} = 0.5$ (*1*) is slower than that in the unperturbed SC system at $\bar{c} = 0$ (*2*). For the sake of visibility, the two curves are plotted in the T/T_c scale, normalized to their respective T_c values from the $v = 1$ line in Fig. 40.

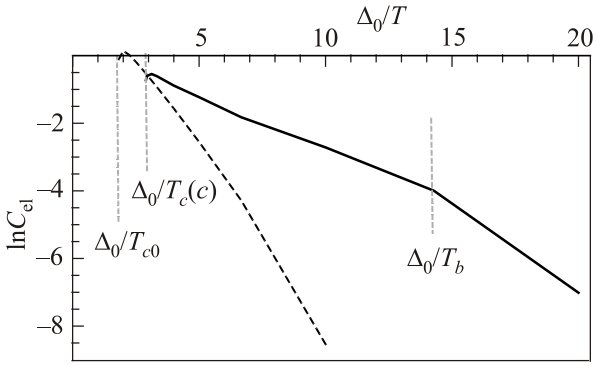

Fig. 42. Logarithmic plots for electronic specific heat vs inverse temperature in the same systems as presented in Fig. 41. Besides the evident lowering of $T_c(c)$ in accordance with Fig. 40, there appears an unconventional impurity effect in a break of the decay exponent at some low temperature T_b, due to the presence of the in-gap impurity band of width comparable to the main band gap (see in Fig. 37), while there is no such break for the unperturbed system (dashed line).

the particular spectrum subbands (the peaks of $\mathrm{Im}\,\hat{G}_{\mathbf{k}}(\varepsilon)$). Respectively, there arise three characteristic types of contributions to $\sigma(\omega,T)$, due to the transitions:

i) from the lower m-band ($\varepsilon' < -\Delta$) to the upper m-band ($\varepsilon > \Delta$), denoted $\sigma_{m\to m}$,

ii) from the lower m-band ($\varepsilon' < -\Delta$) to the upper i-band ($\varepsilon > \varepsilon_-$), denoted $\sigma_{m\to i}$ (or the equivalent $\sigma_{i\to m}$),

iii) from the lower i-band ($\varepsilon' < -\varepsilon_+$) to the upper i-band ($\varepsilon > \varepsilon_-$), denoted $\sigma_{i\to i}$, whose corresponding frequencies are shown schematically in Fig. 43. The calculation in Eq. (81) is simplified with use of the Lorentzian approximation for GF ξ-dependencies:

$$\mathrm{Im}\,\hat{G}_{\mathbf{k}}(\varepsilon) \approx \sum_{j=\pm} \hat{A}_{j,\varepsilon} L\left(\xi - \xi_{j,\varepsilon}, \gamma_{j,\varepsilon}\right), \qquad (84)$$

including the weight matrices:

$$\hat{A}_{\pm,\varepsilon} = \frac{\pi}{2}\left[\rho(\varepsilon)/\rho_N + s(\varepsilon,\Delta)\Delta\hat{\tau}_1 \pm \hat{\tau}_3\right],$$

with $s(\varepsilon,\Delta)$ from Eq. (37), the standard Lorentzian function of halfwidth γ: $L(x,\gamma) = \gamma/[\pi(x^2+\gamma^2)]$, and its peak points $\xi_{\pm,\varepsilon}$ given by Eq. (78). The related halfwidths of these peaks are $\gamma_{\pm,\varepsilon} = 1/\tau^{(l)}$ (with the properly chosen lifetimes from Eqs. (75), (79)) but, if the IRM criterion holds,

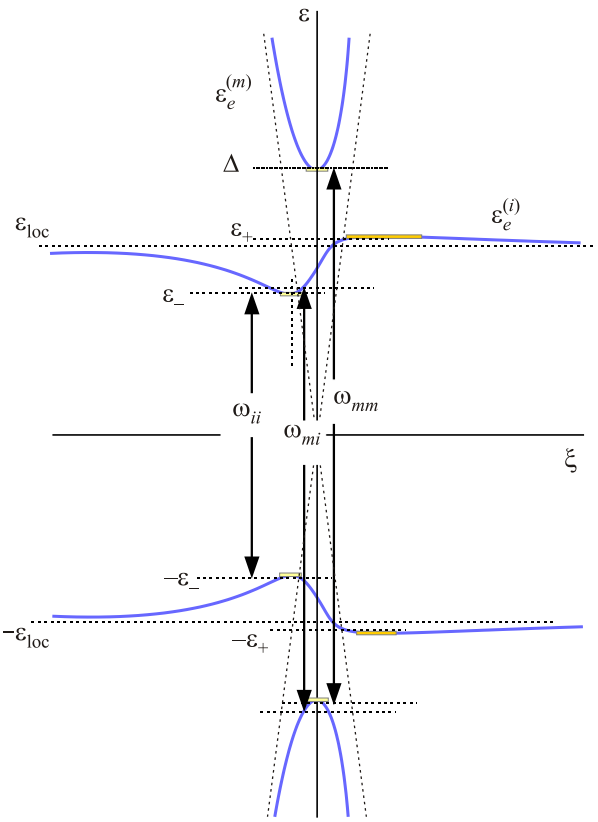

Fig. 43. (Color online) Schematic of optical transitions in the SC system with the quasiparticle spectrum as in Fig. 34 (presented only for its part on the electron pocket).

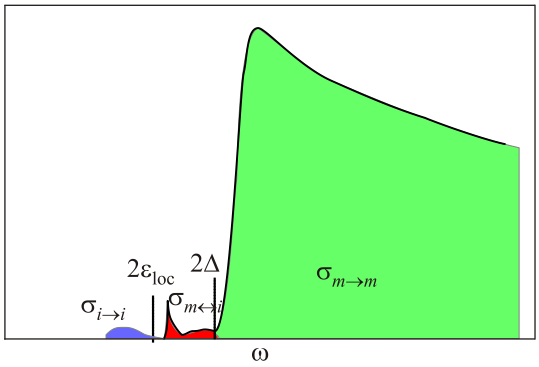

Fig. 44. (Color online) General picture of the optical conductivity showing three types of contributions by the transitions as in Fig. 43 for the choice of impurity parameters $v = 1$ and $\bar{c} = 0.5$.

they are small enough to not matter in the final result. In this approximation, the ξ-integral in Eq. (83) is done by the Lorentzian convolution rule:

$$\int_{-\infty}^{\infty} dx\, L(x,\gamma)L(x-y,\gamma') = L(y,\gamma+\gamma').$$

The next integration in ε of the resulting Lorentzians, when done for the $\sigma_{m\to m}$ and $\sigma_{i\to i}$ processes, involves only the diagonal in j arguments: $\xi_{j,\varepsilon} - \xi_{j,\omega-\varepsilon}$, with the respective $\mathrm{Tr}\,\hat{A}_{j,\varepsilon}\hat{A}_{j,\omega-\varepsilon}$ numerators. But, for the $\sigma_{m\to i}$ and $\sigma_{i\to m}$ processes, it also involves the non-diagonal combinations. Finally, this provides the particular contributions to $\sigma(\omega,T)$ as presented in Fig. 44 for the case of $T = 0$. A more detailed analysis shows that their amplitudes are mainly defined by the quasiparticle velocities for the transition initial and final states, so that the $\sigma_{i\to i}$ profile smoothly vanishes at its edges $2\varepsilon_{\pm}$ (where both velocities vanish, see Fig. 34) while the $\sigma_{m\to i}$ one has a pronounced peak at its lower edge (where both velocities stay finite). Also these amplitudes are notably enhanced compared to simply $a \sim c$ rate of the $\sigma_{m\to m}$ intensity, due to a resonance weight transfer from the main band states, in an analogy to well known effects of this nature in the optical spectra of normal systems with impurities [43,39,96].

This analysis can be evidently extended for such dynamical properties as heat conductivity (by the $\omega \to 0$ limit of an analogue to Eq. (83)) and the Peltier and Seebeck coefficients, but there the quasiparticle lifetimes $\tau^{(l)}$ given by Eqs. (75), (79) are already relevant, defining some analogues to the classical Drude formulas.

7. Concluding remarks

In conclusion, we presented a comprehensive review on various SC systems with impurities that produce different (magnetic and non-magnetic) perturbation types. This demonstrates the importance of detailed dynamical description of all the resulting quasiparticle states in them,

besides the general symmetry principles for impurity perturbations. In this course, a possibility for essential modification of initial quasiparticle spectra appears, consisting in formation of localized in-gap impurity states and their development into specific narrow bands of impurity quasiparticles, provided the impurity concentration is above a certain (quite low) critical value c_0. Consequently, this leads to a number of unusual effects in the system's observable properties.

First of all, this relates to the basic SC order parameter and the critical transition temperature. Besides their known decay, expected to appear at all impurity concentrations, either due to localized or band-like impurity states, a special interest is seen in studying the effects only specific to the impurity band-like states. Here the interplay between the impurity modifications of the SC condensate and of the excited quasiparticles spectrum can produce formation of new non-trivial SC phases and new types of transitions between them and from SC to normal metal state. In particular, depending on the relationship between the symmetries of the host SC order parameter Δ and of the impurity perturbation potential, such unusual phenomena as inversion of the usual Δ decay and vanishing dispersion of the impurity band can take place within some restricted intervals of impurity concentration and temperature. Also, formation of a specific gapless SC state, preceding the transition to the normal metal state, is found possible in certain SC systems with impurities, though it results here from very different dynamical mechanisms and has a different behavior under external factors, compared to the long ago proposed AG structure.

It was then shown that the indicated spectrum restructuring can produce quite pronounced observable effects, either in thermodynamical or kinetic properties of the respective systems, including both their static and high-frequency transport coefficients. In the latter case, the impurity effect is expected in narrow additional peaks of optical conductance near the edge of the main absorption band, resembling the known resonance enhancement of impurity absorption (or emission) processes near the edge of the main quasiparticle band in normal systems. Here it would be possible if the impurity perturbation is weak enough. The static transport coefficients, including the thermoelectric Peltier and Seebeck coefficients, are also expected to be strongly enhanced at overcritical ($c > c_0$) impurity concentrations, compared to those in a non-perturbed system.

Of course, in our theoretical approach to SC systems with impurities, some simplified models were used both for the host spectral structures and for impurity potentials, in order to get the final picture of excitation spectra with collective effects of interactions between impurities taken into account. Nevertheless, the main qualitative results of these considerations can be expected to stay true if more realistic developments be realized. Also, these results indicate an incompleteness of the previously known descriptions of such systems, limited to the simplest first Born approximation for quasiparticle scattering or employing an improper use of the self-consistent (coherent potential) approximation.

Experimental verifications of the predictions made would be of evident interest, since they can open perspectives for important practical applications, e.g., in narrow-band microwave devices or advanced low-temperature sensors, but this would impose rather hard requirements on the quality and composition of the necessary samples, which should be highly pure in addition to containing extremely low (by common standards) and well controlled measures of specially chosen and uniformly distributed impurity centers within the SC crystal lattice structure. These requirements can be compared to those imposed on doped semiconductor devices, these being met over a half century ago, and will hopefully not to present a real problem for modern lab technologies.

We acknowledge the kind assistance by K.Yu. Pogorelov in preparation of this manuscript. V.M.L. thanks the Physics and Astronomy Department of National Academy of Sciences of Ukraine for supporting these researches within the projects No. 0117U00236 and No. 0117U00240.

1. J. Bardeen, L.N. Cooper, and J.R. Schrieffer, *Phys. Rev.* **108**, 1175 (1957).
2. N.N. Bogoliubov, *Sov. Phys. JETP* **34**, 41 (1958).
3. W. Kohn, *Solid State Phys.* **5**, 257 (1957).
4. W. Shockley and J.L. Moll, *Phys. Rev.* **119**, 1480 (1960).
5. B.I. Shklovskii and A.L. Efros, *Electronic Properties of Doped Semiconductors*, Springer-Verlag, Berlin (1984).
6. P.W. Anderson, *J. Phys. Chem. Solids* **11**, 26 (1959).
7. A.A. Abrikosov and L.P. Gor'kov, *Sov. Phys. JETP* **12**, 1243 (1961).
8. M.A. Woolf and F. Reif, *Phys. Rev.* **137**, A557 (1965).
9. T. Sugawara, *Physica* **55**, 143 (1971).
10. Y.-J. Kim and A.W. Overhauser, *Phys. Rev. B* **47**, 8025 (1993).
11. L. Yu, *Acta Phys. Sin.* **21**, 75 (1965).
12. K. Maki, *Phys. Rev.* **153**, 428 (1967).
13. H. Shiba, *Prog. Theor. Phys.* **40**, 435 (1968).
14. A.I. Rusinov, *Sov. Phys. JETP* **29**, 1101 (1969).
15. S.-H. Ji, Z. Tong,Y.-S. Fu, C. Xi, X.-C. Ma, J. Li, W.-H. Duan, J.-F. Jia, and Q.-K. Xue, *Phys. Rev. Lett.* **100**, 226801 (2008).
16. V. Ambegaokar and A. Griffin, *Phys. Rev.* **137**, A1151 (1965).
17. E. Müller-Hartmann and J. Zittartz, *Solid State Commun.* **11**, 401 (1972).
18. J. Zittartz, A. Bringer, and E. Müller-Hartmann, *Solid State Commun.* **10**, 513 (1972).
19. V.M. Loktev and Yu.G. Pogorelov, *Fiz. Nizk. Temp.* **27**, 1039 (2001) [*Low Temp. Phys.* **27**, 767 (2001)].
20. N.F. Mott, *Adv. Phys.* **16**, 49 (1967).
21. M.A. Ivanov and Yu.G. Pogorelov, *JETP* **61**, 1033 (1985).

22. A.F. Ioffe and A.R. Regel, *Progr. Semicond.* **4**, 237 (1960).
23. F. Steglich, C.D. Bredl, W. Lieke, U. Rauchschwalbe, and G. Sparn, *Physica B+C* **126**, 82 (1984).
24. N.E. Alekseevskij and D.I. Khomskij, *Sov. Phys. Usp.* **28**, 1136 (1985).
25. A. Schilling, M. Cantoni, J.D. Guo, and H.R. Ott, *Nature* **363**, 56 (1993).
26. J.G. Bednorz and K.A. Müller, *Z. Physik B* **64**, 189 (1986).
27. *Novel Superconductivity*, S.A. Wolf and V.Z. Kresin (eds.), Springer, Berlin (1987).
28. *Physical Properties of High Temperature Superconductors I*, D.M. Ginsberg (ed.), World Scientific, (1989).
29. J.-P. Brison, L. Glemot, H. Suderow, A. Huxley, S. Kambe, and J. Flouquet, *Physica B* **280**, 165 (2000).
30. J. Nagamatsu, N. Nakagawa, T. Muranaka, Y. Zenitani, and J. Akimitsu, *Nature* **410**, 63 (2001).
31. S.L. Bud'ko, G. Lapertot, C. Petrovic, C.E. Cunningham, N. Anderson, and P.C. Canfield, *Phys. Rev. Lett*. **86**, 1877 (2001).
32. Y. Kamihara, H. Hiramatsu, M. Hirano, R. Kawamura, H. Yanagi, T. Kamiya, and H. Hosono, *J. Am. Chem. Soc.* **128**, 10012 (2006).
33. Y. Kamihara, T. Watanabe, M. Hirano, and H. Hosono, *J. Am. Chem. Soc*. **130**, 3296 (2008).
34. A.P. Drozdov, M.I. Eremets, I.A. Troyan, V. Ksenofontov, and S.I. Shylin, *Nature* **525**, 73 (2015).
35. A.V. Balatsky, M.I. Salkola, and A. Rosengren, *Phys. Rev. B* **51**, 15547 (1995).
36. Yu.G. Pogorelov, *Solid State Commun*. **95**, 245 (1995).
37. Yu.M. Kagan and Yu.A. Iosilevskii, *Sov. Phys. JETP* **15**, 182 (1962).
38. Yu.V. Skripnik and V.M. Loktev, *Phys. Rev. B* **73**, 241402 (2006).
39. M.A. Ivanov, V.M. Loktev, and Yu.G. Pogorelov, *Phys. Rep*. **153**, 209 (1987).
40. S.H. Pan, E.W. Hudson, K.M. Lang, H. Eisaki, S. Ushida and J.C. Davis, *Nature* **403**, 746 (2000).
41. A.V. Balatsky, I. Vekhter, and J.-X. Zhu, *Rev. Mod. Phys*. **78**, 373 (2006).
42. M.M. Korshunov, Yu.N. Togushova, and O.V. Dolgov, *Phys. Usp*. **59**, 12 (2016).
43. I.M. Lifshitz, S.A. Gredescul, and L.A. Pastur, *Introduction into the Theory of Disordered Systems*, Nauka, Moscow (1982).
44. V.L. Bonch-Bruevich and S.V. Tyablikov, *The Green Function Method in Statistical Mechanics*, North Holland, Amsterdam (1962).
45. D.I. Zubarev, *Sov. Phys. Usp*. **3**, 320 (1960).
46. T. Matsubara, *Prog. Theor. Phys*. **14**, 351 (1955).
47. E.Z. Kuchinskii, N.A. Kuleeva, and M.V. Sadovskii, *Fiz. Nizk. Temp*. **43**, 22 (2017) [*Low Temp. Phys*. **43**, 17 (2017)].
48. P.I. Arseev, *Phys. Usp*. **58**, 1159 (2015).
49. V.L. Bonch-Bruevich, *Sov. Phys. Dokl*. **4**, 172 (1959).
50. M. Abramowitz and I. Stegun, *Handbook of Mathematical Functions*, Natl. Bureau of Standards (1964).
51. Marius Grundmann, *The Physics of Semiconductors*, Springer: Berlin, Heidelberg, New York (2006).
52. G. James and M. Liebeck, *Representations and Characters of Groups*, Cambridge University Press, Cambridge (1993).
53. J. Kondo, *Prog. Theor. Phys*. **32**, 37 (1964).
54. V.M. Loktev and Yu.G. Pogorelov, *Dopants and Impurities in High-T_c Superconductors*, Naukova Dumka, Kyiv (2015).
55. Yu.G. Pogorelov, M.C. Santos, and V.M. Loktev, *Phys. Rev. B* **84**, 144510 (2011).
56. V.A. Moskalenko, *FMM* **8**, 503 (1959).
57. H. Suhl, B.T. Matthias, and L.R. Walker, *Phys. Rev. Lett*. **12**, 552 (1959).
58. V.A. Moskalenko and M.E. Palistrant, *Sov. Phys. JETP* **22**, 536 (1966).
59. A.A. Golubov and I.I. Mazin, *Phys. Rev*. **55**, 15146 (1997).
60. X.X. Xi, *Rep. Prog. Phys*. **71**, 116501 (2008).
61. J. Kortus, I.I. Mazin, K.D. Belashchenko, V.P. Antropov, and L.L. Boyer, *Phys. Rev. Lett*. **86**, 4656 (2001).
62. S.V. Okatov, A.L. Ivanovskii, Yu.E. Medvedeva, and N.I. Medvedeva, *Phys. Status Solidi B* **225**, R3 (2001).
63. D.A. Papaconstantopoulos and M.J. Mehl, *Phys. Rev*. **64**, 172510 (2001).
64. I.I. Mazin, O.K. Andersen, O. Jepsen, O.V. Dolgov, J. Kortus, A.A. Golubov, A.B. Kuz'menko, and D. van der Marel, *Phys. Rev. Lett.* **89**, 107002 (2002).
65. T. Dahm, S. Graser, C. Iniotakis, and N. Schopohl, *Phys. Rev. B* **66**, 144515 (2002).
66. K. Rogacki, B. Batlogg, J. Karpinski, N.D. Zhigadlo, G. Schuck, S.M. Kazakov, P. Wägli, R. Puźniak, A. Wiśniewski, F. Carbone, A. Brinkman, and D. van der Marel, *Phys. Rev. B* **73**, 174520 (2006).
67. R.S. Gonnelli, D. Daghero, G.A. Ummarino, A. Calzolari, M. Tortello, V.A. Stepanov, N.D. Zhigadlo, K. Rogacki, J. Karpinski, F. Bernardini, and S. Massidd, *Phys. Rev. Lett.* **97**, 037001 (2006).
68. S. Xu, Y. Moritomo, K. Kato, and A. Nakamura, *J. Phys. Soc. Jpn*. **70**, 1889 (2001).
69. N. Suemitsu, T. Masui, S. Lee, and S. Tajima, *Physica C* **445**–**448**, 39 (2006).
70. C.P. Moca, E. Demler, B. Jankó, and G. Zaránd, *Phys. Rev. B* **77**, 174516 (2008).
71. C.S. Lue, T.H. Su, B.X. Xie, S.K. Chen, J.L. MacManus-Driscoll, Y.K. Kuo, and H.D. Yang, *Phys. Rev. B* **73**, 214505 (2006).
72. X. Zhou, C. Ye, P. Cai, X. Wang, X. Chen, and Y. Wang, *Phys. Rev. Lett*. **106**, 087001 (2011).
73. H. Ding, P. Richard, K. Nakayama, K. Sugawara, T. Arakane, Y. Sekiba, A. Takayama, S. Souma, T. Sato, T. Takahashi, Z. Wang, X. Dai, Z. Fang, G. F. Chen, J.L. Luo, and N.L. Wang, *Europhys. Lett*. **83**, 47001 (2008).
74. T. Kondo, A.F. S.-Syro, O. Copie, C. Liu, M.E. Tillman, E.D. Mun, J. Schmalian, S.L. Bud'ko, M.A. Tanatar, P.C. Canfield, and A. Kaminski, *Phys. Rev. Lett*. **101**, 147003 (2008).
75. I.I. Mazin, D.J. Singh, M.D. Johannes, and M.H. Du, *Phys. Rev. Lett*. **101**, 057003 (2008).
76. D.J. Singh and M.-H. Du, *Phys. Rev. Lett.* **100**, 237003 (2008).
77. K. Haule, J.H. Shim, and G. Kotliar, *Phys. Rev. Lett*. **100**, 226402 (2008).

78. G. Xu, W. Ming, Y. Yao, X. Dai, S.-C. Zhang, and Z. Fang, *Europhys. Lett.* **82**, 67002 (2008).
79. C. Cao, P.J. Hirschfeld, and H.P. Cheng, *Phys. Rev. B* **77**, 220506 (2008).
80. S. Raghu, X.L. Qi, C.X. Liu, D.J. Scalapino, and S.C. Zhang, *Phys. Rev. B* **77**, 220503 (2008).
81. L. Boeri, O.V. Dolgov, and A.A. Golubov, *Phys. Rev. Lett*. **101**, 026403 (2008).
82. Q. Si and E. Abrahams, *Phys. Rev. Lett*. **101**, 076401 (2008).
83. M. Daghofer, A. Moreo, J.A. Riera, E. Arrigoni, D.J. Scalapino, and E. Dagotto, *Phys. Rev. Lett.* **101**, 237004 (2008).
84. W.F. Tsai, Y.Y. Zhang, C. Fang, and J. Hu, *Phys. Rev. B* **80**, 064513 (2009).
85. D. Zhang, *Phys. Rev. Lett*. **103**, 186402 (2009).
86. Y.-Y. Zhang, C. Fang, X. Zhou, K. Seo, W.-F. Tsai, B.A. Bernevig, and J. Hu, *Phys. Rev. B* **80**, 094528 (2009).
87. Yu.G. Pogorelov, M.C. Santos, and V.M. Loktev, *Phys. Rev. B* **88**, 224518 (2013).
88. Y.F. Guo, Y.G. Shi, S. Yu, A.A. Belik, Y. Matsushita, M. Tanaka, Y. Katsuya, K. Kobayashi, I. Nowik, I. Felner, V.P.S. Awana, K. Yamaura, and E. Takayama-Muromachi, *Phys. Rev. B* **82**, 054506 (2010).
89. Y. Li, J. Tong, Q. Tao, C. Feng, G. Cao, W. Chen, F.C. Zhang, and Z.A. Xu, *New J. Phys*. **12**, 083008 (2010).
90. S. Kitagawa, Y. Nakai, T. Iye, K. Ishida, Y.F. Guo, Y.G. Shi, K. Yamaura, and E. Takayama-Muromachi, *Phys. Rev. B* **83**, 180501(R) (2011).
91. F. Hardy, P. Burger, T. Wolf, R.A. Fisher, P. Schweiss, P. Adelmann, R. Heid, R. Fromknecht, R. Eder, D. Ernst, H. v. Loehneysen, and C. Meingast, *Europhys. Lett*. **91**, 47008 (2010).
92. B.S. Chandrasekhar and D. Einzel, *Ann. Physik* **2**, 535 (1993).
93. R.T. Gordon, H. Kim, M.A. Tanatar, R. Prozorov, and V.G. Kogan, *Phys. Rev. B* **81**, 180501 (2010).
94. R. Kubo, *J. Phys. Soc. Jpn*. **12**, 570 (1957).
95. D.A. Greenwood, *Proc. Phys. Soc*. **71**, 585 (1958).
96. V.L. Broude, A.F. Prikhot'ko, and E.I. Rashba, *Phys. Usp*. **2**, 38 (1959).